Application of Mean Field Theory to Nuclear Equation of State and Drip-line Nuclei

By

Shailesh Kumar Singh

Reg. No. PHYS07201004010

Institute of Physics,

Bhubaneswar,
India

A thesis submitted to the

Board of Studies in Physical Sciences

In partial fulfillment of requirements

For the Degree of

DOCTOR OF PHILOSOPHY

of

HOMI BHABHA NATIONAL INSTITUTE

February, 2016

STATEMENT BY AUTHOR

This dissertation has been submitted in partial fulfillment of requirements for an advanced degree at Homi Bhabha National Institute (HBNI) and is deposited in the Library to be made available to borrowers under rules of the HBNI.

Brief quotations from this dissertation are allowable without special permission, provided that accurate acknowledgement of source is made. Requests for permission for extended quotation from or reproduction of this manuscript in whole or in part may be granted by the Competent Authority of HBNI when in his or her judgment the proposed use of the material is in the interests of scholarship. In all other instances, however, permission must be obtained from the author.

Date: (Shailesh Kumar Singh)

CERTIFICATE

This is to certify that the thesis entitled **Application of Mean Field Theory to Nuclear Equation of State and Drip-line Nuclei** which is being submitted by **Shailesh Kumar Singh** in partial fulfilment of the degree of **Doctor of Philosophy in Physics** of **Homi Bhabha National Institute, Mumbai, India** is a record of his own research work carried out by him. He has carried out his investigations for the last five years on the subject matter of the thesis under my guidance at **Institute of Physics, Bhubaneswar, India**. To the best of my knowledge, the matter embodied in the thesis has not been submitted for the award of any other degree by him or by antbody else.

Signature of the Candidate
Shailesh Kumar Singh
Institute of Physics
Bhubaneswar

Signature of the Supervisor
Dr. S. K. Patra
Professor
Institute of Physics
Bhubaneswar

Date:

DECLARATION

I, Shailesh Kumar Singh, hereby declare that the investigations presented in the thesis has been carried out by me. The matter embodied in the thesis is original and has not been submitted earlier as a whole or in part for a degree/diploma at this or any other Institution/University.

Date: (Signature)

Shailesh Kumar Singh

To My Parents

Acknowledgements

I would like to express my special appreciation and thanks to my advisor Professor S. K. Patra, you have been a tremendous mentor for me. I would like to thank you for encouraging my research and for allowing me to grow as a research scholar. Your advice on both research as well as on my life career have been priceless. I would also like to thank my committee members, Prof. A. M. Srivastava, Prof. P. Agrawal and Prof. P. K. Sahu for serving as my committee members for letting my research work be an enjoyable during my years, and for your brilliant comments and suggestions. Furthermore I would like to thank Prof. L. Satpathy, Prof. C. R. Praharaj, Prof. B. K. Agrawal, Prof. P. K. Panda and Prof. R. N. Mishra for their valuable and priceless support and being always available for discussions.

I would like to thank my working group Dr. B. B. Sahu, Dr. M. Bhuyan, S. K. Biswal, B. Kumar, M. Ikram, S. Mahapatro for their patience and support.

I want to put deepest thanks to my classmates Anjan, Arnab, Himanshu, Mohit, Shalik, Sazim, Subhadeep, Mainak and Anwesha, who make my Pre-doc life very challenging and enjoyable. I am thankful to my seniors Dr. Jaya Maji, Dr. Rupali Kundu, Dr. Trilochan da, Dr. Saurabh da, Dr. Sankhu da, Dr. Sachin da, Tanmoy da, Pramita, Tanmoy Pal, Indrani, Subhasis those who always kind for me. I also like to thank my genius and talented juniors who always help me in any new area of problems. Also, I like to thank the institute staffs for supporting me during my journey of research and for making such a beautiful environment so that one can survive in the campus. I would also like to thank all of my friends who supported me in writing, and incented me to strive towards my goal. At the end I would like to express appreciation to my scholar room F-26 friends who spent a lot of time with me and was always supported me in the typical moments.

Date: **Shailesh Kumar Singh**

Contents

Synopsis

The nuclear physics started in 1911 with the discovery of nucleus by the famous gold-foil experiment by Rutherford and group. This experiment was a continuation series of experiments, which finally reached to the conclusion that whole mass of the atom is concentrated at the center called nucleus. After that many theoretical and experimental studies have been carried out to understand the behaviour of the nucleus. However, till now, we have not fully understood the mystery of the system. There is no exact theory which can explain the complete nature, both bulk and microscopic behaviour of the nucleus through out the periodic table. Thus, models are built up and approximation scheme are worked out to explain the properties of nuclei. Unlike the atom, there is not available a definite center for nucleus, so that it will control the movement of the nucleons inside it, which makes the system complicated and it is difficult to explain everything in a simplified model. A nucleus is made up of neutrons and protons (in collective form called as nucleons) which are moving inside the nucleus under the influence of the nuclear force. The nuclear force has a complex behavior, it is strong and short ranged in nature. At large distance, it is attractive with repulsive hard core at the shortest range (near the center). This is found from experimental measurements of phase shift. Attractive force correspond to the positive phase shift and repulsive force to negative phase shift.

In 1934-35, Yukawa had given the meson theory for the N-N interaction. According to this, nucleons are interacting to each other by exchanging the mesons. The repulsive and attractive nature are explain by the vector and scalar mesons which are short and long range interaction, respectively. The range (R) of the interacting mesons are decided by their masses (m) which have inversely proportional with the range of the interaction ($R \propto \frac{1}{m}$) i.e., a large mass mesons are effective at the central and lighter one at the surface regions of the system. In addition to this criteria, the coupling strength is also a deciding factor, i.e., for moderate or smaller coupling constant, lesser important of the meson participation in the force. In this way, one can select the possible kind of mesons to make an optimistic meson-nucleon model. The contribution of the meson within mass $1200 - 1300$ MeV or more has nominal influence on the interaction. Thus, it is a reasonable criteria for a cut for the mass of mesons at the nucleon mass (or slightly more) in the meson-nucleon many-body problems.

The possible mesons may be $\pi-$, $\sigma-$, $\omega-$, $\rho-$, $\delta-$ (and photons) while considering the nucleon-meson theory. The $\pi-$meson is isoscalar-pseudoscalar in nature and due to its smaller mass, it is effective at large distance in comparative to other mesons. But, within the mean field apporoximation, its contribution is negligible for the ground state properties of the nucleus. The other mesons like $\sigma-$, $\omega-$, and $\rho-$ are responsible for the nuclear force at various parts of the interaction range. These mesons are composites (resonance states) of $\pi-$mesons. For example, $\sigma-$meson is s-state resonance of $2\pi-$meson and $\omega-$meson is the p-state of three pions. The $\rho-$meson is p-state resonance of two $\pi-$mesons. There are other mesons also which are effective in the intermediate range according to their masses. One can construct the effective interaction mean field potential by taking these mesons into account.

There are basically two ways of constructing the NN interactions: one is from the origin of the interaction (one boson exchange potential) i.e. nuclear interaction through the exchange particles and another one is from the effective behavior of the interaction (non-relativistic Skyrme potentials) like central and non-central forces. The Nuclear Physics problems are many-body quantum system and dealing with these type of systems are comparatively difficult to handle in both analytically and computationally. Thus, the substitution of effective force is a pragmatic (and successful) apprach to deal these systems. In our analysis, we used the effective mean field theories to deal with the many-body system of nucleons.

We have studied the structural properties in finite nuclei having exotic nature, like bubble structure, "island of inversion" in various region of the mass table and parity doublets in low lying Ω states. The bulk properties, such as binding energy, quadrupole deformation parameter, nucleon density distribution and nuclear matter radii are calculated.

In the present thesis, we construct a simple form of nonlinear self-coupling of the scalar meson field and suggested a new nucleon-nucleon (NN) potential in relativistic mean field theory (RMFT). This potential named as NR3Y (Non-linear Relativistic 3 Yukawa) is analogous to the M3Y (Michigan 3 Yukawa) interaction. We investigate the ability of RMFT to reproduce nuclear ground state properties. The surface phenomena like proton radioactivity with NR3Y interaction potential is discussed in our study. The NR3Y potential could be the substitution of M3Y (Michigan 3 Yukawa) potential for analyzing the reaction rate of the nucleons.

We have extended our work to look for islands of stability, i.e. a set of isotopes which are more stable compare to nearby nuclei. In such cases, in the nuclear chart, some specific isotopes show extra stability than the neighbors, which is known as *"island of inversion"*. These nuclei show exotic behaviour compared to their neighboring nuclei. We study the extremely neutron-rich nuclei for Z = 17-23, 37-40 and 60-64 regions of the periodic table by using axially deformed relativistic mean field formalism. Based on the analysis of binding energy, two neutron separation energy, quadrupole deformation parameter and root mean square radii, we emphasized the speciality of these considered regions. In another work of my thesis, we analyzed the energy levels of nucleons in nucleus as a function of deformation parameter. We obtained results which show that low lying Ω opposite parity states ($\pm\frac{1}{2}$) come closer and formed parity doublet. For this, we have taken Ne, Na, Mg, Al, Si, P, S isotopes in our study and analyzed their radii, deformation parameter and shape coexistence (two shape eigen states of nearly same binding energy). It is very general phenomena near A=100 nuclei region. Based on our analysis, we predict the drip-line which are comparable with the existing experimental data. Our results show sudden fall in two neutron separation energy for some specific neutron number which may be a magic number (for a particular number of neutron or proton) in that region. For conforming these magic numbers, we need some more realistic calculations.

In the relativistic effective mean field theory, the Lagrangian has the meson fields needed for the nucleon force and their self and cross coupling terms are included in the Lagrangian upto optimal levels. In this respect, the G2 force parameter is almost a full set with most of the self and cross couplings and produces better results not only for the finite nuclei but also for the nuclear matter system. The effective mean field motivated relativistic mean field force (E-RMF) parameter follow the naturalness which is the basic requirement in the selection of any set of parameters. The parameter of E-RMF Lagrangian follow the naive dimensional analysis which is the analytical method to truncate the series of Lagrangian interaction terms. Because of the availability of the radioactive ion beam in various laboratories of the globe, advanced facilities like FAIR and PREX are getting attention for the probe further the nuclear drip-line. From these experimental facilities, one thing is clear that experimentalist now want to go more drip-line side and thinking for the more precise data and their relationship with the nuclear matter eqaution of state in extreme conditions which will help to study astrophysical objects, like neutron star etc.

It is possible that the existing theoretical models adequate for these new results or may need some modifications. The expected modification can be done by refitting the exiting parameters with newly obtained results or extend the interaction terms by adding some new couplings which are connected to the observables of the system. During these modifications, one should keep in mind, that the natureness of the older parameter should not be lost. In other way, we can make some new correlation between physical observables of finite and infinite systems. For more asymmetric (for example very neutron rich) nuclear systems, we need a full parameter set which can explain all the physics of the future experiments. Before going to build a new parameter set, we need to check the effectiveness of the extra interaction terms in comparison to the existing couplings. In this respect, we are extending the G2 force parameter by including cross coupling of isoscalar vector $\omega-$meson and isovector vector $\rho-$meson term in the Lagrangian, which is responsible for the neutron skin and softness of the symmetry energy.

Here, we study the effect of non-linear cross coupling on the energy density and pressure over a wide range of baryon densityies. The observables like symmetry energy E_{sym} and related coefficients like slope L_{sym} and curvature K_{sym} of the symmetry energy with respect to the baryon density are also evaluated systematically. The effects of the cross couplings on the symmetry energy of symmetric nuclear matter are studied. The work is further extended to $\beta-$equilibrium neutron matter to estimate the mass and radius of the neutron stars. We analyze the effect of the coupling of the Baryon octet on the nuclear equation of state.

We have also included the extra degree of freedom isovector scalar $\delta-$meson to take care of large asymmetry of the system. For our analysis, we use two types of methodology:

1. We included the $\delta-$meson on top of G2 Lagrangian and by changing the coupling strength of $\delta-$meson which is nothing but the coupling strength of the interaction between $\delta-$meson and nucleons. In our study, we have not included any other degree

of freedom in baryonic sector which will be consider in future work. The work mainly concentrate on this methodology and see the effect of $\delta-$meson coupling constant on finite and infinite nuclear systems. We also extend our calculations to analyse the behavior of coupling constant in mass radius trajectories of neutron star.

2. We split the isospin contribution of the system between $\rho-$ and $\delta-$mesons. Because the $\rho-$meson is responsible for the asymmetry of the nucleon density and mass asymmetry is taken by the $\delta-$meson. It is to be noted that in the symmetric system (number density of protons and neutrons are same) these two mesons have no contribution. In this case, the G2 force parameter changes and we tune the coupling constant to fix the binding energy same as earlier (same as G2 parameter) to see the effects on finite and infinite nuclear system followed by neutron star calculations.

Finally, in the extension of the Lagrangian, our aim is to make a full parameter set by including cross coupling and $\delta-$meson on top of the G2 set. Most of the work has been done and some more are in progress.

We have done works on Nuclear Astrophysics. We study the behaviour of static and rotating neutron star. We have used several relativistic and non-relativistic parameter sets and found the mass and radius of neutron star (NS). We have calculated properties of rotating neutron star like gravitational wave strain amplitude, gravitational wave frequency, Keplerian frequency, quadrupole moment and ellipticity. We get almost consistent results in all considered models which show the model independent predictions of the observables. We found that the gravitational wave strain amplitude is a function of breaking strain of neutron star crust and distance between the star and the earth. From our calculation, we approximate the range of the gravitational wave amplitude between 10^{-24} to 10^{-22}. The moment of inertia of the star comes around $\sim 10^{45}$ g cm^2 and the predicted range of the gravitational wave frequency is in between 400 to 1280 Hz. We have calculated the rotating frequency of star and concluded that, if we increase the rotating frequency then the increment in the mass is also changes subsequently. The ellipticity of the neutron star is consistent in all the considered parameter sets which will be helpful to constrain the value of quadrupole and moment of inertia of the neutron star and vice versa. Our results will be helpful to the new generation of gravitational wave detectors being planned.

List of Publications

1. *Effects of a delta meson in relativistic mean field theory,
   Shailesh K. Singh, S. K. Biswal, M. Bhuyan and S. K. Patra,
   Phys. Rev. C **89**, 044001 (2014).

2. *Effect of isospin asymmetry in nuclear system,
   Shailesh K. Singh, S. K. Biswal, M. Bhuyan and S. K. Patra,
   J. Phys. G: Nucl. Part. Phys. **41**, 055201 (2014).

3. *Importance of non-linearity in NN Potential,
   B. B. Sahu, **S. K. Singh**, M. Bhuyan, S. K. Biswal and S. K. Patra,
   Phys. Rev. C **89**, 034614 (2014).

4. Search of double shell closure in the superheavy nuclei using a simple effective interaction, S. K. Biswal, M. Bhuyan, **S. K. Singh** and S. K. Patra,
   Int. J. Mod. Phys. E **23**, 1450017 (2014).

5. *Superdeformed structures and low Ω parity doublet in Ne-S nuclei near neutron drip-line, **S. K. Singh**, C. R. Praharaj and S. K. Patra,
   Cent. Euro. J. Phys. **12**, 42 (2014).

6. *The effect of isoscalar-isovector coupling in infinite nuclear matter,
   S. K. Singh, M. Bhuyan, P. K. Panda and S. K. Patra,
   J. Phys. G: Nucl. Part. Phys. **40**, 085104 (2013).

7. *Relativistic mean field study of Island of Inversions in neutron-rich Z=17-23, 37-40 and 60-64 nuclei, **S. K. Singh**, S. Mahapatro and R. N. Mishra,
   Int. J. Mod. Phys. E **22**, 1350018 (2013).

8. Ground state properties and bubble structure of synthesized superheavy nuclei,
   S. K. Singh, M. Ikram and S. K. Patra,
   Int. J. Mod. Phys. E **22**, 1350001 (2013).

9. Spectroscopic study of $^{161;163}$Er in Deformed Hartree-Fock theory,
   B. B. Sahu, **S. K. Singh**, S. K. Patra and C. R. Praharaj,
   Acta Physica Polonica B **43**, 451 (2012).

b. Communicated:

1. The effect of self interacting isoscalar-vector meson on finite nuclei and infinite nuclear matter, S. K. Biswal, **S. K. Singh**, M. Bhuyan and S. K. Patra, communicated …

2. Exploration of nuclear matter and finite nuclei observables, S. K. Patra, S. K. Biswal, **S. K. Singh** and M. Bhuyan communicated …

3. Effects of isovector scalar δ-meson on hypernuclei, M. Ikram, S. K. Biswal, **S. K. Singh** and S. K. Patra, communicated …

4. $\Lambda-$interaction with nucleons M. Ikram, **S. K. Singh**, S. K. Biswal, M. Bhuyan and S. K. Patra, communicated …

5. *Gravitational wave from rotating neutron star, **Shailesh K. Singh**, S. K. Biswal, M. Bhuyan, T. K. Jha and S. K. Patra, *communicated* to journal, (1312.5840).

* **Papers included in the thesis**

c. Other Publications:

1. High Spin Spectroscopy of ^{168}Hf Nucleus, B. B. Sahu, **S. K. Singh**, Z. Naik, S. K. Patra and C. R. Praharaj, Proceedings of the DAE Symp. on Nucl. Phys **58**, 246 (2013).

2. The clustering in Magnesium isotopes, M. Bhuyan, **S. K. Singh**, S. K. Biswal and B. K. Sahu, Proceedings of the DAE Symp. on Nucl. Phys **58**, 114 (2013).

3. Yrast Spectra of ^{140}Ba in Deformed Hartree-Fock and J Projection Model,
S. K. Singh, B. B. Sahu, C. R. Praharaj, S. K. Patra, Z. Naik and R. K. Bhowmik,
Proceedings of the DAE Symp. on Nucl. Phys **58**, 248 (2013).

4. Structure and decay properties of Francium isotopes,
S. Mahapatro, M. Bhuyan, **S. K. Singh** and S. K. Patra,
Proceedings of the DAE Symp. on Nucl. Phys **58**, 290 (2013).

5. Comparative study of the effective force parameters NL3 and NL3,
S. K. Singh, M. Ikram, S. K. Biswal, M. Bhuyan and S. K. Patra,
Proceedings of the DAE Symp. on Nucl. Phys **58**, 116 (2013).

6. The effect of mass asymmetry in infinite nuclear matter,
S. K. Singh, S. K. Biswal, M. Bhuyan and S. K. Patra,
Proceedings of the DAE Symp. on Nucl. Phys **58**, 828 (2013).

7. The effect of isoscalar-isovector coupling in infinite nuclear matter,
S. K. Singh, M. Bhuyan, P. K. Panda and S. K. Patra,
AIP Conf. Proc. **1524**, 77 (2013).

8. The relativistic Lagrangian: Nucleon-nucleon potential,
B. B. Sahu, **S. K. Singh**, M. Bhuyan and S. K. Patra,
AIP Conf. Proc. **1524**, 3 (2013).

9. Relativistic mean field study of Island of Inversions in neutron rich Z=17-23 nuclei,
S. Mahapatro, **S. K. Singh**, R. N Mishra,
Proceeding of national Seminar on Recent Trends in LASER and Photonics (RTLP) and 30th Convention of Odisha Physical Society(OPS), p-74, 09-10th Feb, 2013.

10. The nucleon-nucleon potential from relativistic mean field theory,
B. B. Sahu, M. Bhuyan, **S. K. Singh** and S. K. Patra
Proceedings of the DAE Symp. on Nucl. Phys. **57**, 198 (2012).

11. Nuclear matter and finite nuclei properties using simple effective interaction,
M. Bhuyan, **S. K. Singh**, S. K. Tripathy, T. R. Routray, B. Behera, B. K. Sharma, X. Viñas and S. K. Patra,
Proceedings of the DAE Symp. on Nucl. Phys. **57**, 200 (2012).

List of Figures

List of Tables

Chapter 1

Introduction

The nucleus came into picture more than 100 year ago, due to Rutherford's well known experiment of $\alpha-$particle scattering. But its internal configuration came to be known after the discovery of neutron in 1932 by Sir James Chadwick [1]. These discoveries lead to the interesting problem of the stability of a nucleus because it is a composite system of positive and neutral particles. Thus the concept of nuclear force arose, which does not depend on the charge of the system. This continues to be one of the outstanding problems and our understanding of the nature of nuclear interaction at that time and even now has not been fully resolved. Hence, the major goal of nuclear physics (experimental/theoretical) is to develop a proper platform to understand the mystery behind the unpredictable behavior of the nucleus.

In simple terms, the atomic nucleus consists of protons and neutrons, which are commonly known as nucleons, because of their similarity, such as masses and statistics. For simplicity, we assume that nucleons have same mass and they differ only by the isospin quantum number associated with the neutron and proton.

1.1 Nuclei: near and away from the $\beta-$stability line

Naturally, about 300 nuclei are available on the earth's crust which are shown in figure 1.1 by black dots. Most of these naturally occurring nuclei exist on the $\beta-$ stability line and they have almost infinitely large life-time. On the other hand, the formation of the nuclei, which are away from the stability lines has become possible due to the availability of accelerators and stable as well as radio-active nuclear beams in various laboratories, such as HIRFL@CSR [2, 3], FAIR@GSI [4, 5], Spiral@GANIL [6], RIBF@RIEKEN [7] and FRIB@MSU [8], where one can synthesize a large number of isotopes both in the proton and neutron drip-line regions (see Figure 1.1). In India, very good stable beam facilities are in operation at IUAC (New Delhi), TIFR (Mumbai), BARC (Mumbai) and VECC (Kolkata). For lighter mass nuclei (Z=1-8), the drip-lines have already been reached. The drip-line nuclei are those extreme isospin systems, after which the existence of isotopes is not possible, i.e. proton/neutron drip line is reached, when separation energy of one proton/neutron ($S_{p/n}$) tends to zero. These exotic nuclei have very short life time and it is difficult to measure their properties. These drip-line nuclei (or exotic nuclei) have many strange features. In recent years, some interesting phenomena have been found like halo nuclei, variable neutron skin thickness, proton radioactivity and cluster structure in nucleon distribution inside the nucleus. Apart from these highly asymmetric nuclei which are away from the $\beta-$stability line, one more interesting region of the nuclear landscape is the superheavy valley. To our knowledge, till date 118 elements are known to us. Among, these 118 atomic nuclei, up to Z=92 are available in nature, while the rest starting from Z=93 to 118 are man-made superheavy nuclei synthesized in various laboratories [9–21].

1.2 Nuclear Forces and Interactions

In nature, there are four type of fundamental interactions. They are:

1. Gravitational Interaction
2. Electromagnetic Interaction
3. Strong Interaction
4. Weak Interaction

1.2.1 Gravitational Interaction

Gravitational interaction is the most common interaction, and is generated by the masses of the objects. The mediator of this interaction is "Graviton" which is yet to be detected. The

Figure 1.1: Typical landscape for the possible elements (stable, experimentally synthesized, and theoretically predicted) on the earth.

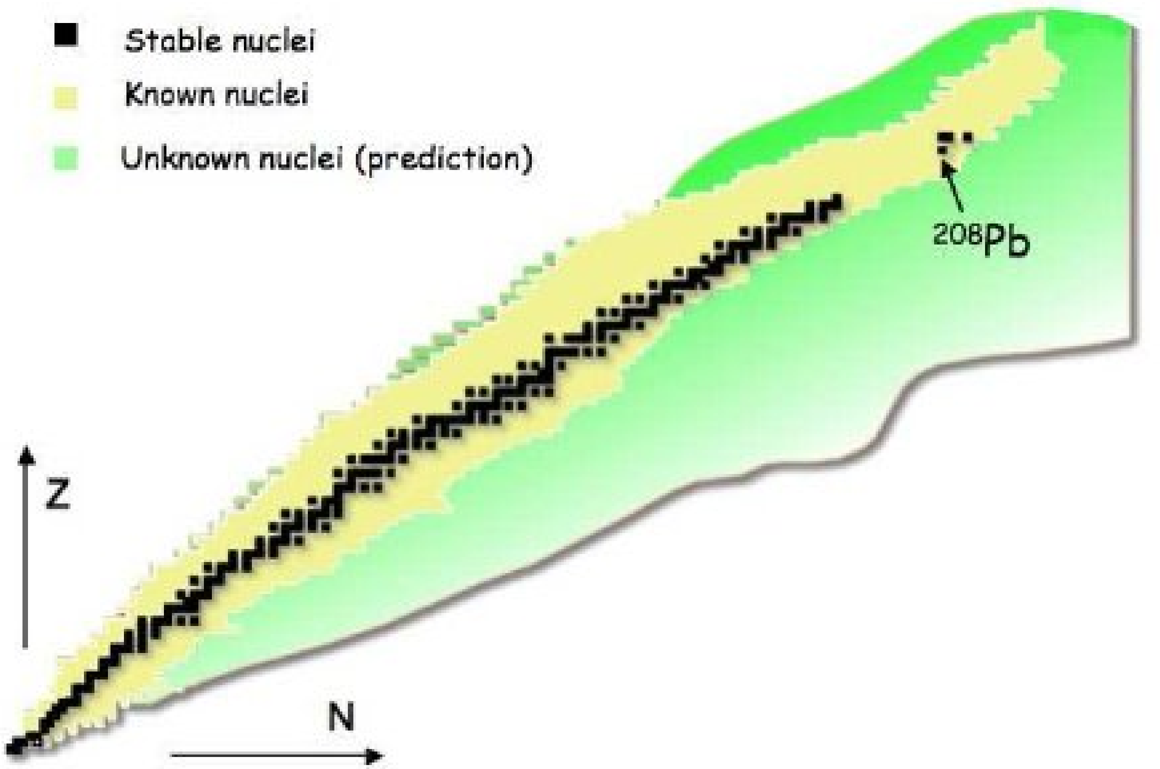

large objects like heavenly bodies such as planets, stars, etc. are maintaining their dynamic stability due to this interaction.

1.2.2 Electromagnetic Interaction

This is the second and most common interaction after the Gravitational force. It arises due to the electric charges and current and magnetic moments. The mediator of this force is the photon, which is a vector particle. Inside the nucleus, the protons are the positively charged particles and its effect can not be ignored for its stability. For example, after Z=8, one needs more number of neutrons for the stability of a nucleus to nullify the effect of Coulomb repulsion. Similarly, it prevents the formation of a superheavy nucleus with large number of proton numbers.

1.2.3 Weak Interaction

Weak interaction is the third type of force, where $W^{\pm}$, Z bosons are the mediator particles. In nuclear physics also, this interaction plays an important role in the decay processes, like $\beta-$decay.

1.2.4 Strong Interaction

The strong interaction is the strongest among all the four. The meson theory became a milestone in understanding the nuclear force, which was given by Hideki Yukawa in 1935 [22]. According to this, nucleons interact with each other through exchange particles and Yukawa predicted that these particles should have mass ($\sim$140 MeV), so called Yukawa particle or pion. This particle was discovered by Powell and collaborators in 1947 [23] which put the confirmatory signature on the Yukawa meson theory. In modern Nuclear Theory, these pions form various composite mesons, such as σ, ω, ρ, δ, Φ, η and many more, which are responsible for the mediation of the strong interaction inside a nucleus. The question arises for practical purpose, which are the mesons actually participating in nucleon-nucleon interactions? This will be discussed in the following subsection.

Table 1.1: Fundamental interactions in nature with their range and associated exchange particles

Interaction	Exchange Particle	Range (meters)
Gravitational	Graviton	∞
Electromagnetic	Photon	∞
Weak	$W^{\pm}$, Z^0	10^{-18}
Strong	Mesons	10^{-15}

1.3 Role of the various Mesons

Now, we discuss about the role of various mesons in the NN-interaction inside a nucleus. The properties of nucleon along with some mesons are listed in Table 1.2. The general form of NN-interaction is shown in Figure 1.2, where various mesons are associated with the long, intermediate and short range depending on their masses. From computational and analytical point of view, one has to choose the meson-nucleon interaction, which is relevant for the nuclear system. In this context, the range r_i and mass of the meson propagator P_i may be important criteria for the selection. The massive mesons are less important in the interaction as propagator being inversely proportional μ_i^2 implies range is inversely proportional to μ_i, with μ_i as the mass of the meson. In addition to this criteria, the coupling strength is also a deciding factor, i.e., for moderate or smaller coupling constant, the mesons become less important [24]. In this way, one can select the possible kinds of mesons to make an optimistic meson-nucleon model. Also, the strange mesons are suppressed by Zweig forbidden rule [25] in the NN-interaction. The contribution of the mesons within mass $1200 - 1300$ MeV or more has nominal influence in the interaction. Thus, it is a reasonable criteria to have a cut off for the selection of mesons at the mass of the nucleon or slightly more to include all type of effects in the meson-nucleon many-body problems. The possible mesons $\pi-$, $\sigma-$, $\omega-$, $\rho-$, $\delta-$ and photon fields are important while considering the nucleon-meson theory and all other mesons listed in the box at the bottom.

In relativistic mean field (RMF) approximation, the pseudo-scalar $\pi-$meson does not contribute to nuclear bulk properties, because of the definite spin and parity of the ground state nucleus [26–29]. The quark composition of this meson triplet is ($\pi^+ : u\bar{d}$), ($\pi^0 : \frac{u\bar{u}-d\bar{d}}{\sqrt{2}}$) and ($\pi^- : d\bar{u}$). The masses are 139.57 and 134.9766 MeV for $\pi^{\pm}$ and π^0, respectively

Table 1.2: The nucleons and mesons properties like mass (MeV), charge (e), spin (J), isospin (I) and third component of the isospin (I_3), parity (P) and $G-$parity (G) are given here.

Baryons Section					
Particle	mass (MeV)	q(e)	J	I	I_3
p (proton)	938.27	+1	$\frac{1}{2}$	$\frac{1}{2}$	+$\frac{1}{2}$
n (neutron)	939.57	0	$\frac{1}{2}$	$\frac{1}{2}$	-$\frac{1}{2}$

Mesons Section			
Type of meson	mass (MeV)	J^P	I^G
$\pi^{\pm}$	139.57	0^-	1^-
π^0	134.96	0^-	1^-
δ	983	0^+	1^-
σ	$\sim$500	0^0	0
ω	782.6	1^-	0^-
ρ	769	1^-	1^+
η	548.8	0^-	0^+
$\eta^{'}$	957.6	0^-	0^+
ϕ	1020	1^-	0^-
B	1234	1^+	1^+
f	1274	2^+	0^+
D	1283	1^+	0^+

Figure 1.2: General form of the NN-interaction with the role of various participating mesons.

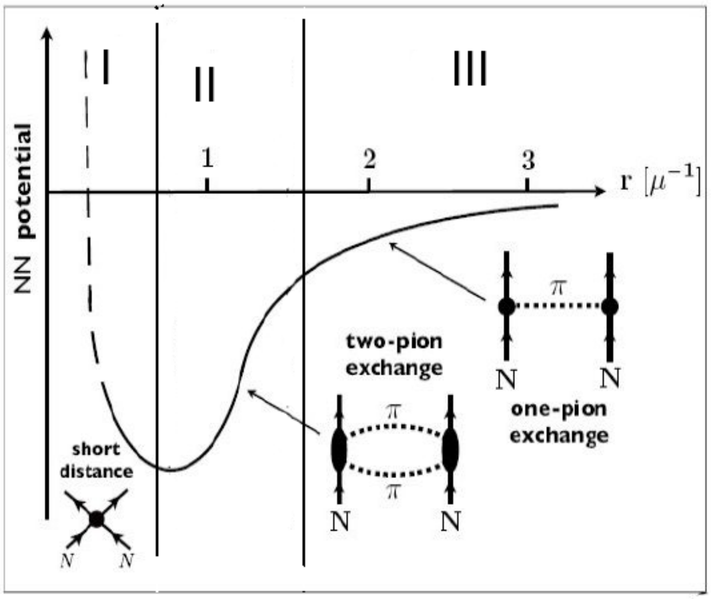

and spin-parity is 0^{-1}. The field corresponding to the iso-scalar scalar $\sigma-$meson, which is a broad two-pion resonance state (s wave) provides strong scalar attraction at intermediate distance (>0.4 fm) and has a mass of $400 \sim 550$ MeV [30, 31], which is the most dominating attractive part of the nuclear interaction. The quark structure of $\sigma-$meson is $\frac{u\bar{u}+d\bar{d}}{\sqrt{2}}$ and its spin parity (J^P) is 0^+. The non-linearity of the $\sigma-$meson coupling includes the 3-body interaction [32, 33], which is currently considered as an important ingredient for nuclear saturation.

The isoscalar-vector $\omega-$meson, which is a $3\pi-$ resonance state with a mass of 781.94 $\pm$ 0.12 MeV, gives the strong vector repulsion at short distance giving rise to the hard core repulsion of the nuclear force. The self-coupling of the $\omega-$meson is crucial to make the nuclear equation of state (EOS) softer [34–37], which has important consequence in determining the structure of neutron star. The quark structure of $\omega-$meson is $\frac{u\bar{u}+d\bar{d}}{\sqrt{2}}$ and J^P=1^-.

The isovector-vector $\rho-$meson is introduced to account for asymmetry of neutron-proton number densities. It is a resonance of $2\pi-$meson in p-state which contributes to the high repulsive core near the center and the attractive behavior near the intermediate range in the even-singlet central potential of NN-interaction [38, 39]. The $\rho-$meson has mass around 768.5 $\pm$ 0.6 MeV [31]. The quark structure of the neutral $\rho-$meson is $\frac{u\bar{u}-d\bar{d}}{\sqrt{2}}$ and J^P=1$^-$. The isovector-scalar $\delta-$meson is the resonance state of $\eta\pi$ (dominant channel) and $\overline{K}K$ (minor channel) [39,40], which has a mass of 980 $\pm$ 20 MeV [31]. Its quark structure is given as $\frac{u\bar{u}-d\bar{d}}{\sqrt{2}}$ and J^P=1$^-$. The neutron, propton mass difference can be explained by introducing the isovector scalar δ meson with nucleons. Thus, it has substantial effects in highly asymmetric systems like neutron star and heavy ion collision.

It is to be noted that the bulk properties like binding energy and charge radius do not isolate the contribution from the iso-scalar or iso-vector channels. It needs an overall fitting of the parameters. That is the reason, the modern Lagrangian ignores the contribution of $\delta-$ and $\rho-$mesons independently, i.e. once $\rho-$meson is included, it takes care of the properties of the nuclear system and does not need the $\delta-$meson [41–44]. However, the importance of the $\delta-$meson arises, when we study the properties of highly asymmetric systems such as drip-line nuclei and neutron star [45–57]. In particular, at high densities such as neutron star and heavy ion collisions, the proton fraction of $\beta-$stable matter can increase and the splitting of the effective mass can affect the transfer properties. Also, at high isospin asymmetry, because of the increase in proton fraction, influences the cooling of neutron star [58–60].

1.4 Infinite Nuclear System

A system which has a large number of particles ($A \rightarrow \infty$) and a large volume compared to the finite nuclei is known as infinite nuclear system. When both neutron and proton numbers are same ($\alpha = \frac{\rho_n-\rho_p}{\rho_n+\rho_p} = 0$) then it is pronounced as symmetric nuclear matter and in asymmetric matter case $\alpha \neq 0$. Just after the discovery of neutron, Weizsac̆ker gave the well known semi-empirical mass formula [61] in 1935. This was the first empirical mass formula which explained the average nuclear binding energy. Simply put this equation is given as:

$$B(N,Z) = a_v A - a_s A^{2/3} - a_c \frac{Z^2}{A^{1/3}} - a_a \frac{(N-Z)^2}{A}, \tag{1.1}$$

where A = N + Z is the total number of nucleons and a_i for *i* = *v, s, c* and *a* are the volume, surface, Coulomb and asymmetry co-efficients of the system, respectively. All the parameters are fitted to the experimental masses. If we put the infinite nuclear matter condition i.e. $A \rightarrow \infty$ in equation 1.1 for symmetric matter then only volume energy coefficient a_v survives. This is its empirical value and its dimension is energy. It is known as the binding energy per nucleon (BE/A$\sim$-16.0 MeV) and the corresponding density is known as the saturation density (ρ_0). The relation between energy density and pressure is known as the equation of state (EOS). The most important example of large density ($\rho \sim 5{-}7\rho$) systems is neutron star (NS), where protons and neutrons are being equilibrated by chemical equilibrium and charge neutrality conditions.

Now, we will discuss some nuclear matter properties which are constrained by physical observables. These quantities are incompressibility, effective mass, symmetry energy, saturation density. A brief description of these are given below:

1.4.1 Incompressibility

The incompressibility of a system is a dynamical quantity, which shows how much the system can be compressed at the saturation density ρ_0, without violating the Pauli exclusion principle. This plays an important role in the nuclear equation of state (EOS). For example, a stiffer EOS has higher incompressibility in comparison to the softer one. We have noticed in RMF theory that the incompressibility is a poorly determined quantity, because its range varies from 200 to 600 MeV depending on the force parameters. In the old linear parametrizations like L1, L2, and SH, the value of K_∞ is $\sim$550MeV; however for the newer parameter sets with non-linear terms, this value comes down in the range of $200 - 300$ MeV [62–65].

1.4.2 Effective Mass

The effective mass m^* of a nucleon plays a significant role in heavy ion collision (HIC), which leads to different paths for the neutron and proton. The main reason of this effect is the difference in effective masses of each proton and neutron. It is worth mentioning that many theoretical models are a bit unclear in the determination of the effective mass. Thus, the well established models like Landau-Fermi liquid theory, non-relativistic Bruckner-Hartree-Fock ($m_n^* > m_p^*$) [66, 67] and relativistic Dirac-Brueckner ($m_n^* < m_p^*$) [49, 50, 68] predict diverge behaviour of m^* which indicates the deficiency in understanding. The different effective mass of proton and neutron is due to the existence of isovector-scalar interaction in the nuclear potential [49, 69]. The constraint on m^* can be taken from the heavy ion collision data [70]. The asymmetry of the system due to nucleon density is taken care by the isovector-vector interaction. Earlier in RMF model effective mass of proton and neutron are taken as a single entity and adjusted by a single parameter. In **Chapter 7** of the present thesis, we have separately considered them on equal footing, which has significant consequences.

1.4.3 Symmetry Energy

A lot of works are going on to constrain the symmetry energy E_s by finite and infinite nuclear properties. The precise knowledge of the symmetry energy is the requirement of the present day nuclear physics/astrophysics. As we know, it has a correlation with the skin data ($R_n - R_p$) of finite nuclei and behaviour of equation of state for the nuclear matter system. Some experiments are very sensitive to the density variation of the symmetry energy i.e. behaviour of E_s at various range of the nuclear matter density. Some observables like π^-/π^+ [52,71–78], n/p [79–81], t/3He [82,83], the isospin fractionation [79,81,84,85] and the neutron-proton differential flow [50,86] are used to determine the symmetry energy of a nuclear system. For constraining this quantity by the neutron-proton differential transverse flow, we divide the whole symmetry energy behaviour with the density into two parts: one is stiff and second one is soft symmetry energy [87]. Another possibility of constraining the E_s at normal density is the skin data of ^{208}Pb nucleus, because skin thickness depends on symmetry pressure of the neutron rich matter [88]. The skin data is also strongly correlated with the slope of the symmetry energy at saturation density [89]. Recently, it has been reported that the skin of ^{208}Pb nucleus has a direct correlation with the radius of neutron star [90, 91]. Thus, it gives new hope that from the recent experimental observation of new X-ray pulsar, one can measure the neutron star radius quite precisely.

The behaviour of the symmetry energy above the saturation density is not well understood, i.e. it increases/decreases with baryon density [92]. Neutron stars (NS) are good example for the highly asymmetric and dense system. By measuring the properties of NS, like mass and corresponding radius, we can constraint the behaviour of symmetry energy and neutron skin data, because these two are correlated observables which connect the finite to infinite system [93]. Apart from these, the properties of rotating and axially deformed neutron star like gravitational wave strain amplitude (h_0), ellipticity and sensitivity of the r-mode instability window are studied by the behaviour of symmetry energy at high density (larger than saturation density ρ_0) [94].

1.5 Neutron Star

For general study, one can consider the neutron star to be static and spherical which may not be true in real case. It behaves like a liquid drop which is made of nucleons. The characteristic observables of the neutron star are mass (in units of solar mass) and physical radius R (km). which are constrained from experimental observations. The experimental limit on the maximum star mass is 2.01$\pm$0.04 $M_\odot$ from the pulsar PSR J0348+0432, using white dwarf spectroscopy [95]. This maximum mass is more than the earlier prediction of the measured mass of the millisecond pulsar PSR J16142230, which is 1.97$\pm$0.04 $M_\odot$, using Shapiro delay [96]. The Shapiro time delay effect, or gravitational time delay effect, is one of the four classic solar system tests of general relativity. Radar signals passing near a massive object take slightly longer to travel to a target and longer to return than they would if the mass of the object were not present. The time delay is caused by the slowing passage of light as it moves over a finite distance through a change in gravitational potential [97]. In these measurements, we obtain the upper limit of the maximum mass of neutron star which is more precise than the radius. Although, the radius of the neutron star is not precisely known, one can fix the limit on this way by analyzing the Quiescent low mass binaries [98]. The star mass and radius can be obtained by the Tolman-Oppenheimer-Volkoff (TOV) equation, where energy density and pressure are the inputs [99]. In reality, the neutron star is non-static and asymmetric, one can consider it as rotating with the angular momentum ω and having finite quadrupole deformation. The maximum possible angular velocity of the star is known as Kepler angular velocity ω_k. After this velocity, the system will not be stable or gravitational force is unable to bind the system. For solving the rotating neutron star equation of state, we use rotating equation of motions. The rotating objects radiate energy due to the asymmetry of the shape. This type of radiation is known as gravitaional waves [100] which are considered elaborately in **Chapter 8** of this thesis.

1.6 Nuclear Models

Unlike atomic case, there is no central force which controls the movement of nucleons inside the nucleus. All the nucleons have equivalent contribution to the nuclear potential. The properties of nucleus change significantly with the increase in nucleon number. Therefore, in Nuclear Physics, no unique theory exists to describe the nuclear phenomena. There are several models which describe the nuclear systems region by region. The models and their parameters are based on the well known experimental observables. The reliability of a model is tested by its ability to reproduce the experimental data. A good model should also have predictive power which will be helpful to show the path for future experiments. If one adds either a proton or a neutron to the nucleus, its behavior changes drastically than the parent system. As a result, each and every nucleus/isotope needs special attention both experimentally and theoretically. In various cases, it so happens that the well designed nuclear models fail to explain the properties of nucleus in extreme conditions. In this context there is a big debate about the nuclear system. "Is it a relativistic system or non-relativistic system", because both types of models explain nuclear properties quite satisfactorily. According to the non-relativistic phenomenon, the binding energy per nucleon is very small ($\sim 8MeV$) compared to its mass ($\sim$1 GeV), so it should behave like a non-relativistic system, while in the relativistic formalism, this small binding energy comes from the cancellation of two big contributions (a strong attractive and repulsive components). Hence, it should follow the relativistic dynamics. Although, the present thesis is meant for the study of finite and infinite nuclear systems within the frame work of Relativistic Mean Field formalism and non-relativistic Skyrme-Hartree-Fock approach, it is worthy to mention some well known models such as Infinite Nuclear Mass model, Finite Range Droplet model and liquid drop model whose results we use for comparison very often in different parts of the thesis.

1.7 Evolution of Models in Nuclear Structure Physics

Liquid Drop Model: The first and most successful model "Liquid Drop Model (LDM)" was given by George Gamow and further modifications were proposed by Niels Bohr and J. A. Wheeler. According to this model, nucleons are interacting with each other like a molecule in a drop of liquid. The density of the liquid is assumed to be homogeneous and constant for the entire volume and drop can not be compressed further i.e., volume is fixed. In this model, nucleons are moving in the interior of the system and collide with each other. The maximum distance travelled by nucleon before collision is its mean free path [101, 102] which is smaller than the diameter of the liquid drop. The LDM easily explains the nuclear binding energy, nuclear fission and reactions by assuming the shape of the nucleus spherical in ground state.

As time evolved, more nuclei were studied. The LDM was a crude approximation, as it was not able to explain all the properties of various nuclei. It was observed that a special combinations of the neutron (2, 8, 20, 28, 50, 82, 126) and proton (2, 8, 20, 28, 50, 82) numbers show extra stability and these combinations are called Magic Numbers. In this respect, the proton magic number beyond $Z = 82$ is still under debate. Some theoretical group predict that $Z = 120$ is the next proton magic number beyond ^{208}Pb [103–105]. In this respect, to reproduce the magic number, V. M. Strutinsky added the shell correction into the LDM and was successful in reproducing a 1-2 MeV difference in binding energy [106].

Finite Range Droplet Model: Another successful model is "Finite Range Droplet Model (FRDM)", which is used as a standard reference while developing new calculations [107]. In this model nucleus is taken as a drop of Fermi liquid. It describes the nuclear masses and deformations very well. The formalism combines the Droplet Model with the folding of model surface and Coulomb energy integrals [108].

Infinite Nuclear Mass Model: The Infinite Nuclear Matter (INN) model [109] is based on Hugenholtz-Van Hove theorem [110]. According to this model, the ground state energy of an asymmetric nucleus is considered as equivalent to the energy of a perfect sphere made up of the infinite nuclear matter of same asymmetry plus residual energy. The residual energy comes from the shell effect, deformation etc. The scope of this mass relation (INM) is limited in the sense that if two masses are known the third can be predicted within very small error but can not be extended to very unknown territory.

Shell Model: The shell model (SM) is a microscopic nuclear model which was able to explain the magic numbers. This model was given by two group M. G. Mayer and J. H. D. Jensen at the same time in 1949, independently. It is based on the assumption that a nucleon is moving freely in a potential well which is generated by other nucleons. It assumes a core at the center and other nucleons are moving under the influence of that core.

The modern shell model has no core and is now known as no-core shell model [111–113]. Here, all the nucleons are taken as independent from each other. This type of calculations need very good computational facilities, and are now possible due to the availability of high performance computing systems.

Effective mean field theory: The self-consistent mean field theories (SCMF) are recently used extensively in theoretical models to deal with the nuclear many-body system. These formalisms are surprisingly successful to deal with nuclei (on and away of the stability line) through out the periodic table from proton to neutron drip-line. There are almost two parallel models available in literature one is non-relativistic (Gogny, Skyrme) and other one is relativistic mean field (RMF) formalism. The energy functional of the Skyrme-Hartree-Fock (SHF) approach is the combination of all the possible interaction like the effective interaction between nucleons, the Coulomb energy, the pairing energy and corrections for spurious motion like center of mass. The SHF interaction is a zero range force while the RMF has a finite range interaction due to the exchange of mesons. Since, the Skyrme energy functional is local, it has several technical advantages like all exchange terms have the same structure as the direct terms, which reduces the number of integrations when solving the Skyrme Hartree-Fock equations. However, the Skyrme-Hartree-Fock (SHF) model has strictly point couplings. The gradient terms in the energy functional fulfill the finite range interaction. It merges the gradient term with the zero-range two-body force into a finite-range two-body coupling. Although, the depth of nuclear potential is near 100 MeV and much smaller than the nucleon rest mass ($\sim$1 GeV), this depth is a result of cancellation between much larger contributions. These are good reasons to consider relativistic dynamics for the nuclear system. The large nuclear spin-orbit force also comes out naturally from the interplay between two strong and counteracting fields: a long-range attractive scalar field and a short range repulsive vector field [39]. The typical order of the scalar potential is $\sim$ -400 MeV which is attractive and vector part is $\sim$ 300 MeV repulsive. So, net potential is attractive with combination of the scalar and vector part of the nuclear interactions. The saturation properties of the nuclear matter could not be explained by the conventional non-relativistic mean field models [114]. However, the simplest model of RMF formalism i.e. Walecka Lagrangian is able to produce the empirical data ($BE/A = -15.6$ MeV, $k_F = 1.36$ fm^{-1}) [115, 116]. A detailed discussion of the models (RMF, SHF) are presented in **Chapter 2**.

1.8 Plan of the Thesis

Taking into consideration the nuclear force and the contemporary problems in nuclear physics, we have used the SHF and RMF models throughout the mass table to study the properties of $\beta-$stable and unstable nuclei. We have given emphasis to the drip-line nuclei as well as the superheavy elements. Thus, we have analyzed the RMF model and studied the effects of its various terms. In general, the thesis is divided into two parts:

1) Application of the mean field models (RMF and SHF) to finite nuclei. Here, we calculate the bulk properties, like binding energy, charge radii, single particle energy and quadrupole deformation with the help of these observables and we discuss various physical consequences.

2) The second part of the thesis is devoted to the expansion of the Lagrangian and analyze the effects of extra degree of freedom. We study the influence of $\delta-$meson and cross coupling of $\omega-\rho$mesons on physical properties within the RMF formalism.

1.8.1 Properties of finite nuclei

The thesis proceeds through a brief introduction of nuclear experimental and theoretical status followed by evolution of the theoretical models. In this thesis, we have given a full flavor of relativistic and non-relativistic mean field formalisms for finite as well as infinite nuclear matter in **Chapter 2**. We have found an analytical expression for the NN-interaction, both from the linear and non-linear RMF models, denoted as R3Y and NR3Y interactions analogous to the well known M3Y and DDM3Y interactions. A simplified and approximate expression with its application to $\alpha-$particle decay is given in **Chapter 3**. We investigate the ability of RMF theory to reproduce the nuclear ground state properties and the surface phenomena like proton radioactivity simultaneously with the proposed NN-interaction. The obtained results are matched reasonably well with most widely used M3Y NN-interactions and the experimental data in this first application of nucleon-nucleon potential.

In **Chapter 4**, we have discussed the behavior of intrinsic single particle energy levels of nucleons with deformation. Other properties of finite nuclei like shape co-existence, deformation parameter etc. are also mentioned. We have analyzed the structure of Ne, Na, Mg, Al, Si, P and S near the neutron drip-line region in the frame-work of relativistic mean field theory (RMF) and non-relativistic Skyrme-Hartree-Fock (SHF) formalisms. The recently discovered nuclei ^{40}Mg and ^{42}Al, which are beyond the drip-line predicted by various mass formulae are located within the drip-line under these models. For some isotopes, we have found many largely deformed neutron-rich nuclei, whose structures are analyzed. From structure point of view, we find that at large deformation, low Ω orbits of opposite parities (e.g. $\frac{1}{2}^+$ and $\frac{1}{2}^-$) occur close to each other in energy, which some times may lead to the case of octupole deformation.

In some regions of the mass tables, few isotopes show extra stability in comparison to the neighbour which is called "Island of Inversion". Normally, the stability of nuclear isotopic series decreases with increase in the neutron number when moving towards the neutron drip-line. But this trend breaks due to some specific combination of proton and neutron number, a phenomena similar to the magic numbers. We study the extremely neutron-rich nuclei with $Z = 17-23$, $37-40$ and $60-64$ regions of the periodic table in **Chapter 5**. Based on the analysis of binding energy, two neutron separation energy, quadrupole deformation and root mean square radii, we emphasize the specialty of these considered regions which were recently predicted as *"islands of inversion"*.

1.8.2 Extension of RMF model

In **Chapter 6**, our aim is to expand the Lagrangian by adding the $\omega-\rho$cross term which was not included earlier. It is found to be useful in softening the symmetry energy. The neutron skin thickness and symmetry energy are correlated, but due to unavailability of the precise measurement of skin data, this correlation is also debatable. In the framework of relativistic mean field theory, we study the effect of non-linear cross coupling between the isoscalar-vector and isovector-vector mesons ($\omega-\rho$) on top of G2 parametrization. The energy density and pressure are calculated over a wide range of baryon density. The physical observables like symmetry energy and related coefficients are also evaluated systematically. The effect of cross coupling on the symmetry energy of symmetric nuclear matter are studied. The work is further extended to $\beta-$equilibrium matter to estimate the mass and radius of neutron star and also to baryon octet to see the effect of the cross coupling over the equation of state.

In **Chapter 7**, we have added one more term ($\delta-$meson coupling) to the Lagrangian and further extend our calculations. The effect of $\delta-$ and $\omega-\rho-$meson cross couplings on asymmetric nuclear systems are analyzed in the frame-work of an effective Field theory motivated relativistic mean field (ERMF) formalism. The calculations are done on top of the G2 parameter set. We calculate the root mean square radius, binding energy, single particle energy (for 1^{st} and last occupied orbits), density and spin-orbit interaction potential for some selected nuclei and evaluate the $L_{sym}-$ and $E_{sym}-$ coefficients for nuclear matter as function of coupling strengths. The number and mass isospin which are taken care by $\rho-$ and $\delta-$ meson respectively are connected to each other. So, it is very obvious to take the coupling of these two mesons with nucleons together and see the combined effect on the nuclear system. To show the effect of $\delta-$meson on the nuclear system, we split the isospin coupling into two parts: (i) g_ρ due to $\rho-$meson and (ii) g_δ for $\delta-$meson. Thus, our investigation is based on varying the coupling strengths of the $\delta-$ and $\rho-$mesons to reproduce the binding energies of the nuclei: ^{48}Ca and ^{208}Pb.

In **Chapter 8**, we present the applications of nuclear equation of states in cosmology. The calculations are carried out to obtain the masses and radii of static and rotating neutron stars by taking a large variety of relativistic and non-relativistic force parameters. These calculations may be quite useful for future experiments.

Finally, we have concluded the work in **Chapter 9**.

Chapter 2

Formalism

As it is discussed in **Chapter 1**, the nucleus is a complex many body system. To explain the properties of such a system, a large number of theoretical models have been constructed, which are available in literature. Among them the non-relativistic Skyrme-Hartree-Fock (SHF) and relativistic mean field (RMF) theories are quite successful. In these models, the many body system is converted to one body problem and few corrections like center-of-mass motion and pairing correction are introduced to reach an the acceptable level of accuracy. This technique has been widely used for the last 4 decades to study the ground state properties of finite nuclei. The two models SHF and RMF are considered to be at par, as both of them give almost comparable results and predictions. In the present thesis, these two models have been taken as the main theoretical tools and we have used them to analyze the nuclear systems in various conditions. In this chapter, a detailed discussion has been presented to understand these two theoretical formalisms.

2.1 Skyrme-Hartree-Fock (SHF) method

The Skyrme-Hartree-Fock theory is well documented and can be found in Refs. [117–120]. For completion, we outline some of the basic features in this chapter. The SHF approach converts the nucleon-nucleon two-body potential to an average field [121]. While constructing the potential, it is to be noted that one should take into account all the features of nuclear force (as discussed in **Chapter 1**). Thus it is essential to know the properties of nuclear interaction in detail. Some of them are:

- The nuclear force is short ranged, i.e. the influence of the interaction of a pair of nucleons does not affect other nucleons, which are far away from it.
- There is definite evidence of the presence of spin-orbit interaction, tensor force and pairing correlation in a nuclear potential.
- The average binding energy per particle of a finite nucleus is about 8 MeV, which is very small compare to the mass of a nucleon i.e. $\sim$938 MeV. This plays an important role in the success of non-relativistic approach.
- The average nuclear potential is $\sim$ 70 MeV deep, which is much smaller compared to the nucleon mass.

The nucleons are Fermions, so they follow the Fermi-Dirac statistics. As we have discussed, the many-body system can be converted to a one body problem using the Hartree-Fock approximation for the ground-state trial wave-function of a nucleus. The A particles wave function can be written as a Slater determinant or an antisymmetric product of occupied states. The Slater determinant is built from a complete orthonormal set of single-particle wave-functions $\phi_i(r_j)$ (the Hartree-Fock basis), here r_j stands for all the coordinates ($spatial$, $spin$ and $isospin$) of the j^{th} nucleon

$$\Phi(r_1, ..., r_A) \longrightarrow \Phi_{HF}(r_1, ..., r_A) = \frac{1}{\sqrt{A!}} \begin{bmatrix} \phi_1(r_1) & \phi_2(r_1) & \cdots & \phi_A(r_1) \\ \phi_1(r_2) & \phi_2(r_2) & \cdots & \phi_A(r_2) \\ \vdots & \vdots & \cdots & \vdots \\ \vdots & \vdots & \ddots & \vdots \\ \phi_1(r_A) & \phi_2(r_A) & \cdots & \phi_A(r_A) \end{bmatrix}. \quad (2.1)$$

The full Hamiltonian of the many body system after applying the Hartree Fock approximation can be written as a sum of one-body kinetic energy term and a two-body force for a system of A particles as [117]:

$$H = \sum_{i}^{A} \frac{\mathbf{p}_i^2}{2m_i} + \frac{1}{2} \sum_{i,j}^{A} V(\mathbf{r_i}, \mathbf{r_j}), \quad (2.2)$$

where $V(\mathbf{r_i}, \mathbf{r_j})$ contains all parts of the nucleon-nucleon force, including the Coulomb interaction and a half factor to avoid the double counting of the interactions. The main aim of **Mean Field Model** is to simplify the two-body $V(\mathbf{r_i}, \mathbf{r_j})$ potential in terms of a one-body mean-field which incorporates maximum physics of the original one. In the Hartree-Fock approach the expectation value of the total Hamiltonian with respect to the Hartree-Fock wave-function gives the approximate ground-state energy, which can be written as:

$$\begin{aligned} E^0_{HF} &= \langle \Phi_{HF}|H|\Phi_{HF}\rangle \\ &= -\frac{\hbar^2}{2m}\sum_i^A \int \phi_i^*(\mathbf{r})\nabla^2\phi_i(\mathbf{r})d\mathbf{r} \\ &\quad +\frac{1}{2}\sum_{i,j}^A \int\int \phi_i^*(\mathbf{r})\phi_j^*(\mathbf{r}')V(\mathbf{r},\mathbf{r}')\phi_i(\mathbf{r})\phi_j(\mathbf{r}')d\mathbf{r}d\mathbf{r}' \\ &\quad -\frac{1}{2}\sum_{i,j}^A \int\int \phi_i^*(\mathbf{r})\phi_j^*(\mathbf{r}')V(\mathbf{r},\mathbf{r}')\phi_i(\mathbf{r}')\phi_j(\mathbf{r})d\mathbf{r}d\mathbf{r}', \end{aligned} \tag{2.3}$$

here, $\int d\mathbf{r} = \sum_{i,j}^A d^3r$. The next aim is to find out the ground state energy of the system by the variational method. With a proper guess of the Hartree-Fock wave function, the final self-consistent solution will give the correct ground state energy. The wave function should be normalized so that:

$$\frac{1}{A}\sum_{i=1}^A \int |\phi_i(\mathbf{r})|^2 d\mathbf{r} = 1. \tag{2.4}$$

Now, the Schrödinger equation for the single-particle Hamiltonian can be given by:

$$h|\phi_i(\mathbf{r})\rangle = \epsilon_i|\phi_i(\mathbf{r})\rangle. \tag{2.5}$$

This leads to a simplified form for the Hartree-Fock equation and is given as:

$$\epsilon_i = -\frac{\hbar^2}{2m} + U_H^{(i)}(\mathbf{r})\phi_i(\mathbf{r}) - \int U_F^{(i)}(\mathbf{r},\mathbf{r}')\phi_i(\mathbf{r}')d\mathbf{r}', \tag{2.6}$$

where, $U_H^{(i)}$ and $U_F^{(i)}$ are known as the direct or Hartree and exchange or Fock potential term, respectively. This equation looks like a regular one-body Schrödinger equation with extra non-local term. Finally, we need to solve these equations in a self-consistent way iteratively and get the ground state energy for the system [118, 119].

2.1.1 The Skyrme effective interaction

The most general form of the Skyrme effective potential is written as:

$$
\begin{aligned}
V(\mathbf{r_1}, \mathbf{r_2}) &= t_0(1 + x_0\mathbf{P}_\sigma)\delta(\mathbf{r}) \\
&+\frac{1}{2}t_1(1 + x_1\mathbf{P}_\sigma)\left[\mathbf{P}^{'\mathbf{2}}\delta(\mathbf{r}) + \delta(\mathbf{r})\mathbf{P}^2\right] \\
&+t_2(1 + x_2\mathbf{P}_\sigma)\mathbf{P}^{'} \cdot \delta(\mathbf{r})\mathbf{P} \\
&+\frac{1}{6}t_3(1 + x_3P_\sigma)\left[\rho(\mathbf{R})\right]^\sigma \delta(\mathbf{r}) \\
&+iW_0\sigma \cdot \left[\mathbf{P}^{'} \times \delta(\mathbf{r})\mathbf{P}\right]. \qquad (2.7)
\end{aligned}
$$

The 1^{st} term corresponds to the central part, 2^{nd} & 3^{rd} term are the non-local terms, 4^{th} for density-dependent and $last$ one for the spin-orbit interaction. The center of mass coordinate $\mathbf{R} = \frac{1}{2}(\mathbf{r_1} + \mathbf{r_2})$ and relative coordinates $\mathbf{r} = \frac{1}{2}(\mathbf{r_1} - \mathbf{r_2})$ have their own meanings. The operators $\mathbf{P}$ and $\mathbf{P}^{'}$ are acting on left which is given as: $\mathbf{P} = \frac{1}{2i}(\nabla_1 - \nabla_2)$. The *spin* operator $\sigma = \sigma_\mathbf{1} + \sigma_\mathbf{2}$ and the spin-exchange operator is $P_\sigma = \frac{(1+\sigma_\mathbf{1}\cdot\sigma_\mathbf{2})}{2}$. From the general Skyrme effective interaction (2.7), the total binding energy of a nucleus can be expressed as [118]:

$$\langle\Phi_{HF}|H|\Phi_{HF}\rangle = \int \mathcal{H}(\mathbf{r})dr, \qquad (2.8)$$

here, $|\Phi_{HF}\rangle$ is the ground state Hartree Fock wave function, $\mathcal{H}$ is the total Hamiltonian density functional, which is given as:

$$\mathcal{H} = \mathcal{K} + \mathcal{H}_0 + \mathcal{H}_3 + \mathcal{H}_{eff} + \mathcal{H}_{fin} + \mathcal{H}_{so} + \mathcal{H}_{sg} + \mathcal{H}_{Coul}, \qquad (2.9)$$

where, $\mathcal{K}$ is the kinetic term and is expressed as:

$$\mathcal{K} = \frac{\hbar^2}{2m}\tau = \frac{\hbar^2}{2m}(\tau_n + \tau_p), \qquad (2.10)$$

with $\tau = \tau_n + \tau_p$, called the total (sum of proton and neutron) kinetic energy density. The terms, $\mathcal{H}_0$, $\mathcal{H}_3$, $\mathcal{H}_{eff}$, $\mathcal{H}_{fin}$, $\mathcal{H}_{so}$, $\mathcal{H}_{sg}$ and $\mathcal{H}_{Coul}$ are the density functional for zero-range, density-dependent, effective-mass, finite-range, spin-orbit, tensor-coupling and Coulomb correction, respectively. The corresponding expression for these terms are as follow:

$$
\begin{aligned}
\mathcal{H}_0 &= \frac{1}{4}t_0\left[(2+x_0)\rho^2-(2x_0+1)(\rho_p^2+\rho_n^2)\right],\\
\mathcal{H}_3 &= \frac{1}{24}t_3\rho^\eta\left[(2+x_3)\rho^2-(2x_3+1)(\rho_p^2+\rho_n^2)\right],\\
\mathcal{H}_{eff} &= \frac{1}{8}\left[t_1(2+x_1)+t_2(2+x_2)\right]\tau\rho\\
&+\frac{1}{8}\left[t_2(2x_2+1)-t_1(2x_1+1)\right](\tau_p\rho_p+\tau_n\rho_n),\\
\mathcal{H}_{fin} &= \frac{1}{32}\left[3t_1(2+x_1)-t_2(2+x_2)\right](\nabla\rho)^2\\
&-\frac{1}{32}\left[3t_1(2x_1+1)+t_2(2x_2+1)\right]\times\left[(\nabla\rho_{\mathbf{n}})^2+(\nabla\rho_{\mathbf{p}})^2\right],\\
\mathcal{H}_{so} &= \frac{1}{2}W_0\left[\mathbf{J}\cdot\nabla\rho+\mathbf{J_p}\cdot\nabla\rho_{\mathbf{p}}+\mathbf{J_n}\cdot\nabla\rho_{\mathbf{n}}\right],\\
\mathcal{H}_{sg} &= -\frac{1}{16}\left[(t_1x_1+t_2x_2)\,\mathbf{J}^2-(t_1-t_2)\,(\mathbf{J_p^2}+\mathbf{J_n^2})\right],
\end{aligned}
$$

and

$$
\mathcal{H}_{Coul} = =\frac{1}{2}\int\frac{\rho_p(\mathbf{r_2})}{|\mathbf{r_1}-\mathbf{r_2}|}d^3r_2-\frac{3}{4}\left(\frac{3}{\pi}\right)^{1/3}\rho_p^{4/3}(\mathbf{r_1}). \tag{2.11}
$$

The term $\mathcal{H}_{Coul}$ has two parts corresponding to direct and exchange interaction at Slater level [118]. The total density $\rho=\rho_p+\rho_n$, kinetic density $\tau=\tau_n+\tau_p$ and the spin density $\mathbf{J}=\mathbf{J_n}+\mathbf{J_p}$. The corresponding expressions for these densities are:

$$
\rho_q(\mathbf{r})=\sum_{i=1}^{A_q}\sum_{\sigma}|\phi_i(\mathbf{r},\sigma,q)|^2, \tag{2.12}
$$

$$
\tau_q(\mathbf{r})=\sum_{i=1}^{A_q}\sum_{\sigma}|\nabla\phi_i(\mathbf{r},\sigma,q)|^2, \tag{2.13}
$$

and

$$
J_q(\mathbf{r})=i\sum_{i=1}^{A_q}\sum_{\sigma,\sigma'}\phi_i^*(\mathbf{r},\sigma,q)\left[(\sigma)_{\sigma,\sigma'}\times\nabla\right]\phi_i(\mathbf{r},\sigma,q), \tag{2.14}
$$

where, ϕ_i is the single-particle wave function with *orbital*, *spin* and *isospin* quantum numbers. Now these equations are solved self-consistently by using the Skyrme parameter sets [117]. These parameter sets are designed on the basis of various experimental data of finite nuclei and properties of infinite nuclear matter [118–120, 122, 123]. Some of them reproduce both the ground state properties of finite nuclei [124, 125] and properties of infinite nuclear matter upto high density [117]. In our calculations, we have used different Skyrme parameter sets. In recent years, several new sets of Skyrme parameters such as SLy1-10, SkX, SkI5 and SkI6 are obtained by fitting the Hartree-Fock (HF) results with experimental data for nuclei starting from the valley of stability to neutron and proton driplines [118–120, 122].

2.2 Relativistic Mean Field Formalism

From the last few decades, the relativistic mean field (RMF) theory has been applied successfully to study the structural properties of nuclei throughout the periodic table [26, 126–129]. At high density, the mesons which are the medium for NN-interaction, can be taken as mean field. At this point, meson field operators, can be replaced by their expectation values (classical fields) which is known as the mean field approximation [26]. The relativistic field theory of the nuclear system was first developed by Schiff in 1951 [33]. In this investigation, he had taken linear and non-linear self-interaction in classical neutral scalar meson field. This non-linear term may be helpful to achieve saturation in the nuclear system.

In 1955, Johnson and Teller modified the Schiff ideas up to a significant level and used only linear interaction of scalar field to explain the many empirical features of nuclear structure [130]. The first time they put their attention towards the scalar sigma meson degree of freedom in the NN-interaction, although its decay width $\sigma \rightarrow 2\pi$ is very large. Dürr took the Johnson and Teller concept and proposed the theory of vector and scalar meson fields. This model was able to explain the many nuclear properties and other like spin-orbit interaction, and energy dependence of the real part of the nuclear optical potential [131]. Dürr observed that nuclear saturation can be obtained naturally by including the non-linear coupling of scalar meson interaction.

In 1961, Rozsnayi performed the relativistic Hartree calculations of finite nuclear structure. The problem of stationary baryon interacting with a classical vector meson field was studied by Zel'dovich in 1962 [132]. The complete form of the RMF model came in 1974 by Walecka [26] which incorporated sigma (σ), omega (ω) and rho (ρ) mesons to describe the finite and infinite systems. This model provides considerably large value of bulk modulus K (~ 560) than the acceptable empirical value (230±30) [133]. Boguta and Bodmer resolved this problem by including the non-linear interaction in sigma meson (scalar). This extended Lagrangian is known as non-linear Walecka model which is the most acceptable interaction Lagrangian till date.

The relativistic treatment of the quantum hadrodynamic (QHD) models automatically takes care of spin-orbit force (interaction), the finite range and the density dependence of the nuclear interaction. The relativistic mean field (RMF) or the effective field theory motivated relativistic mean field (E-RMF) model has the advantage that, with proper relativistic kinematics and meson properties, already known or fixed from the properties of a small number of finite nuclei, gives excellent results for binding energies, root-mean-square (rms) radii, quadrupole and hexadecapole deformations and other properties of spherical and deformed nuclei [38, 127, 134–136]. The quality of the result is comparable to that of non-relativistic nuclear structure calculations with effective Skyrme [137] or Gogny [138] forces.

The theory and equations for finite nuclei and nuclear matter can be found in Refs. [139–143] and we shall give only the outline of the formalism. We start from Ref. [142] where the field equations are derived from an energy density functional containing Dirac baryons and classical scalar and vector mesons. The field equations for mesons and nucleons are solved by the self-consistent way, which is a successful technique in effective field theory. It gives excellent results for finite and infinite nuclear systems [37, 129, 139, 144–146]. The energy density functional for finite nuclei can be written as:

$$\begin{aligned}
\mathcal{E}(r) \;=\; & \sum_{\alpha}\psi_{\alpha}^{\dagger}(r)\Bigg\{-i\boldsymbol{\alpha}\cdot\boldsymbol{\nabla}+\beta\left[M-\Phi(r)-\tau_3 D(r)\right]+W(r)+\frac{1}{2}\tau_3 R(r)+\frac{1+\tau_3}{2}A(r) \\
& -\frac{i\beta\boldsymbol{\alpha}}{2M}\cdot\left(f_v\boldsymbol{\nabla}W(r)+\frac{1}{2}f_\rho\tau_3\boldsymbol{\nabla}R(r)\right)\Bigg\}\psi_\alpha(r)+\left(\frac{1}{2}+\frac{\kappa_3}{3!}\frac{\Phi(r)}{M}+\frac{\kappa_4}{4!}\frac{\Phi^2(r)}{M^2}\right)\frac{m_s^2}{g_s^2}\Phi^2(r) \\
& -\frac{\zeta_0}{4!}\frac{1}{g_v^2}W^4(r)+\frac{1}{2g_s^2}\left(1+\alpha_1\frac{\Phi(r)}{M}\right)\left(\boldsymbol{\nabla}\Phi(r)\right)^2-\frac{1}{2g_v^2}\left(1+\alpha_2\frac{\Phi(r)}{M}\right) \\
& \left(\boldsymbol{\nabla}W(r)\right)^2-\frac{1}{2}\left(1+\eta_1\frac{\Phi(r)}{M}+\frac{\eta_2}{2}\frac{\Phi^2(r)}{M^2}\right)\frac{m_v^2}{g_v^2}W^2(r)-\frac{1}{2e^2}\left(\boldsymbol{\nabla}A(r)\right)^2 \\
& -\frac{1}{2g_\rho^2}\left(\boldsymbol{\nabla}R(r)\right)^2-\frac{1}{2}\left(1+\eta_\rho\frac{\Phi(r)}{M}\right)\frac{m_\rho^2}{g_\rho^2}R^2(r)-\Lambda_v\left(R^2(r)\times W^2(r)\right) \\
& +\frac{1}{2g_\delta^2}\left(\boldsymbol{\nabla}D(r)\right)^2-\frac{1}{2}\frac{{m_\delta}^2}{g_\delta^2}\left(D^2(r)\right)\;, \qquad (2.15)
\end{aligned}$$

where $\Phi(r) = g_s\phi_0(r)$, $W(r) = g_v V_0(r)$, $R(r) = g_\rho b_0$, $D(r) = g_\delta\delta_0(r)$ and $A(r) = eA_0(r)$ are the fields for $\sigma, \omega, \rho, \delta$ and photon and g_s, g_v, g_ρ, g_δ and $\frac{e^2}{4\pi}$ are their coupling constants, and masses are m_s, m_v, m_ρ and m_δ, respectively. ψ is field for nucleons. In the energy functional, the non-linearity as well as the cross-coupling upto a maximum of 4^{th} order is taken into account. This is restricted due to the condition $1 \geq \frac{field}{M}$ (M = nucleon mass) and non-significant contribution of the higher order [141]. The higher order non-linear couplings for $\rho-$ and $\delta-$meson fields are not taken into the energy functional, because the expectation values of the $\rho-$ and $\delta-$ fields are orders of magnitude less than that of $\omega-$field and they have only marginal contribution to finite nuclei. For example, in calculations of the high-density equation of state, Müller and Serot [140] find the effects of a quartic ρ meson coupling (R^4) to be appreciable only in stars made of pure neutron matter. A surface contribution $-\alpha_3 \Phi\,(\boldsymbol{\nabla} R)^2/(2g_\rho^2 M)$ is tested in Ref. [147] and it is found to have absolutely negligible effects. We should note, nevertheless, that very recently it has been shown that couplings of the type $\Phi^2 R^2$ and $W^2 R^2$ are useful to modify the neutron radius in heavy nuclei while making very small changes to the proton radius and the binding energy [91].

The Dirac equation corresponding to the energy density eqn. (2.15) becomes

$$\Big\{ - i\boldsymbol{\alpha}\cdot\boldsymbol{\nabla} \;\; + \;\; \beta[M - \Phi(r) - \tau_3 D(r)] + W(r) + \frac{1}{2}\tau_3 R(r) + \frac{1+\tau_3}{2} A(r) - \frac{i\beta\boldsymbol{\alpha}}{2M}\cdot\left[f_v \boldsymbol{\nabla} W(r) + \frac{1}{2} f_\rho \tau_3 \boldsymbol{\nabla} R(r) \right] \Big\}\, \psi_\alpha(r) = \varepsilon_\alpha\, \psi_\alpha(r)\,. \quad (2.16)$$

The mean field equations for Φ, W, R, D and A are given by

$$\begin{aligned}
-\Delta\Phi(r) + m_s^2\Phi(r) &= g_s^2\rho_s(r) - \frac{m_s^2}{M}\Phi^2(r)\left(\frac{\kappa_3}{2} + \frac{\kappa_4}{3!}\frac{\Phi(r)}{M}\right) \\
&\quad + \frac{g_s^2}{2M}\left(\eta_1 + \eta_2\frac{\Phi(r)}{M}\right)\frac{m_v^2}{g_v^2}W^2(r) + \frac{\eta_\rho}{2M}\frac{g_s^2}{{g_\rho}^2}m_\rho^2 R^2(r) \\
&\quad + \frac{\alpha_1}{2M}[(\boldsymbol{\nabla}\Phi(r))^2 + 2\Phi(r)\Delta\Phi(r)] \\
&\quad + \frac{\alpha_2}{2M}\frac{g_s^2}{g_v^2}(\boldsymbol{\nabla}W(r))^2\,, \qquad (2.17)
\end{aligned}$$

$$\begin{aligned}
-\Delta W(r) + m_v^2 W(r) &= g_v^2\left(\rho(r) + \frac{f_v}{2}\rho_{\mathrm{T}}(r)\right) - \left(\eta_1 + \frac{\eta_2}{2}\frac{\Phi(r)}{M}\right)\frac{\Phi(r)}{M}m_v^2 W(r) \\
&\quad - \frac{1}{3!}\zeta_0 W^3(r) + \frac{\alpha_2}{M}[\boldsymbol{\nabla}\Phi(r)\cdot\boldsymbol{\nabla}W(r) + \Phi(r)\Delta W(r)] \\
&\quad -2\;\Lambda_v {g_v}^2 R^2(r) W(r)\,, \qquad (2.18)
\end{aligned}$$

$$\begin{aligned}
-\Delta R(r) + m_\rho^2 R(r) &= \frac{1}{2}g_\rho^2\left(\rho_3(r) + \frac{1}{2}f_\rho\rho_{\mathrm{T},3}(r)\right) - \eta_\rho\frac{\Phi(r)}{M}m_\rho^2 R(r) \\
&\quad -2\;\Lambda_v {g_\rho}^2 R(r) W^2(r)\,, \qquad (2.19)
\end{aligned}$$

$$-\Delta A(r) = e^2\rho_{\mathrm{p}}(r)\,, \qquad (2.20)$$

$$-\Delta D(r) + {m_\delta}^2 D(r) = g_\delta^2\rho_{s3}\,, \qquad (2.21)$$

where the baryon, scalar, isovector, proton and tensor densities are

$$\rho(r) = \sum_\alpha \psi_\alpha^\dagger(r)\psi_\alpha(r)\,, \tag{2.22}$$

$$\rho_s(r) = \sum_\alpha \psi_\alpha^\dagger(r)\beta\psi_\alpha(r)\,, \tag{2.23}$$

$$\rho_3(r) = \sum_\alpha \psi_\alpha^\dagger(r)\tau_3\psi_\alpha(r)\,, \tag{2.24}$$

$$\rho_{\mathrm{p}}(r) = \sum_\alpha \psi_\alpha^\dagger(r)\left(\frac{1+\tau_3}{2}\right)\psi_\alpha(r)\,, \tag{2.25}$$

$$\rho_{\mathrm{T}}(r) = \sum_\alpha \frac{i}{M}\boldsymbol{\nabla}\cdot\left[\psi_\alpha^\dagger(r)\beta\boldsymbol{\alpha}\psi_\alpha(r)\right]\,, \tag{2.26}$$

$$\rho_{\mathrm{T},3}(r) = \sum_\alpha \frac{i}{M}\boldsymbol{\nabla}\cdot\left[\psi_\alpha^\dagger(r)\beta\boldsymbol{\alpha}\tau_3\psi_\alpha(r)\right]\,, \tag{2.27}$$

$$\rho_{s3}(r) = \sum_\alpha \psi_\alpha^\dagger(r)\tau_3\beta\psi_\alpha(r), \tag{2.28}$$

with ρ_{s3}=$\rho_{sp} - \rho_{sn}$, ρ_{sp} and ρ_{sn} as scalar densities for proton and neutron, respectively. The scalar density ρ_s is expressed as the sum of proton (p) and neutron (n) scalar densities ρ_s=$\langle\bar{\psi}\psi\rangle$=$\rho_{sp}$+$\rho_{sn}$, which are given by

$$\rho_{si} = \frac{2}{(2\pi)^3}\int_0^{k_{Fi}} d^3k \frac{M_i^*}{(k^2+M_i^{*2})^{\frac{1}{2}}}, \qquad i = p, n \tag{2.29}$$

k_i is the nucleon's Fermi momentum and M_p^*, M_n^* are the proton and neutron effective masses, respectively and can be written as

$$M_p^* = M - \Phi(r) - D(r), \qquad M_n^* = M - \Phi(r) + D(r), \tag{2.30}$$

Thus, the δ field splits the nucleon effective masses. The baryon density is given by

$$\rho = \langle\bar{\psi}\gamma^0\psi\rangle = \gamma\int_0^{k_F} \frac{d^3k}{(2\pi)^3}, \tag{2.31}$$

where γ is spin or isospin multiplicity ($\gamma = 4$ for symmetric nuclear matter and $\gamma = 2$ for pure neutron matter). The proton and neutron Fermi momentum will also split, while they have to fulfill the following condition:

$$\rho = \rho_p + \rho_n = \frac{2}{(2\pi)^3}\int_0^{k_{Fp}} d^3k + \frac{2}{(2\pi)^3}\int_0^{k_{Fn}} d^3k. \tag{2.32}$$

The total vector potential V(r) is given by the summation of potential generated by the ω, ρ and Coulomb fields V_0, R_0 and A_0, respectively.

$$V(r) = g_v V_0(r) + \frac{1}{2} g_\rho \tau_3 b_0(r) + e\frac{(1-\tau_3)}{2} A_0(r). \tag{2.33}$$

The total attractive scalar potential $V_s(r)$ is described as:

$$V_s(r) = g_s \phi_0(r) + g_\delta \tau_3 \delta_0(r), \tag{2.34}$$

where, $\phi_0(r)$, $\delta_0(r)$ are scaler fields by σ and δ mesons, respectively. A static solution is obtained from the equations of motion to describe the ground state properties of nuclei. The set of nonlinear coupled equations are solved self-consistently in an axially deformed harmonic oscillator basis with the maximum oscillator shells for Fermions (N_F) and Bosons (N_B). The oscillator frequency $\hbar\omega_0 = 41A^{-1/3}$ is used in the calculations. The quadrupole deformation parameter β_2 is extracted from the calculated quadrupole moments of neutrons and protons through the following relation:

$$Q = Q_n + Q_p = \sqrt{\frac{16\pi}{5}} \left(\frac{3}{4\pi} A R^2 \beta_2 \right), \tag{2.35}$$

where R = $1.2A^{1/3}$.

The root mean square charge radius(r_{ch}), proton radius (r_p), neutron radius (r_n) and matter radius (r_m) are given as [38]:

$$< r_p^2 > = \frac{1}{Z} \int \rho_p(r) r_p^2 d\tau_p, \tag{2.36}$$

$$< r_n^2 > = \frac{1}{N} \int \rho_n(r) r_n^2 d\tau_n, \tag{2.37}$$

$$r_{ch} = \sqrt{r_p^2 + 0.64}, \tag{2.38}$$

$$< r_m^2 > = \frac{1}{A} \int \rho(r) r^2 d\tau, \tag{2.39}$$

here, all terms have their own usual meaning. The total energy of the system is given by

$$E_{total} = E_{part} + E_\sigma + E_\omega + E_\rho + E_\delta + E_c + E_{pair} + E_{c.m.}, \tag{2.40}$$

where E_{part} is the sum of the single particle energies of the nucleons and E_σ, E_ω, E_ρ, E_δ, E_c, E_{pair}, E_{cm} are the contributions of the meson fields, the Coulomb field, pairing energy and the center-of-mass energy, respectively. The total binding energy and other observables are also obtained by using the standard relations, given in [38, 127]. The center-of-mass motion correction in light mass nuclei is very important; we have taken care within the harmonic oscillator approximation. Its final expression is $E_{cm} = \frac{3}{4}.41A^{-1/3}$ MeV [34, 148, 149]. The BCS pairing approach is used to take care of the nucleon pairing correlation near the Fermi surface.

2.2.1 Pairing Correlation (E_{pair})

For open shell nuclei, pairing correlation plays an important role. This interaction contains terms like $\psi^\dagger\psi^\dagger$, $\psi\psi$, $\psi^\dagger\psi^\dagger\psi^\dagger\psi^\dagger$, $\psi\psi\psi\psi$ etc. which do not appear in the relativistic Lagrangian. To take care of the pairing effect in the calculation, we use the Bardeen-Cooper-Schrieffer (BCS) pairing prescription, while determining the bulk properties like binding energy (BE), quadrupole deformation parameter and nuclear radii of finite nuclei. The pairing energy can be given as:

$$E_{pair} = -G\left[\sum_{\alpha>0} u_\alpha v_\alpha\right]^2, \tag{2.41}$$

where G is the pairing force constant and v_α^2, and $u_\alpha^2 = 1 - v_\alpha^2$ are occupation and unoccupation probabilities, respectively [127, 150, 151]. The simple form of BCS equation can be derived from the variational method with respect to the occupation number v_α^2:

$$2\epsilon_\alpha u_\alpha v_\alpha - \triangle(u_\alpha^2 - v_\alpha^2) = 0, \tag{2.42}$$

using $\triangle = G\sum_{\alpha>0} u_\alpha v_\alpha$. The above equation (2.42) is known as BCS equation for pairing energy.

The occupation number is defined as:

$$n_\alpha = v_\alpha^2 = \frac{1}{2}\left[1 - \frac{\epsilon_\alpha - \lambda}{\sqrt{(\epsilon_\alpha - \lambda)^2 + \triangle^2}}\right]. \tag{2.43}$$

In our calculations, we are dealing with the nuclei, many of them are far from the beta stability line. The pairing gap $\triangle$, used in the calculation is determined from the odd-even experimental binding energies. The chemical potential λ is determined by the particle numbers for nucleons. However, these values are not always available for the drip-line region. To estimate these constant gaps, we used the empirical expressions of Madland and Nix [152, 153] which are:

$$\triangle_p = RB_s e^{sI-tI^2}/Z^{1/3} \tag{2.44}$$

and

$$\triangle_n = RB_s e^{-sI-tI^2}/A^{1/3}, \tag{2.45}$$

with R=5.72, s=0.118, t= 8.12, B_s=1, and $I = (N-Z)/(N+Z)$.

In this thesis work, we have taken the **constant pairing gap** for all states $|\ \alpha >=|\ nljm >$ near the Fermi surface for the sake of simplicity. As we know, if we go near the neutron drip line, then coupling to the continuum becomes important [154, 155]. In this case, we should use the Relativistic Hartree-Bogoliubov (RHB) approach which is more accurate for this region. However, it has been shown that with the use of BCS pairing correlation with sufficient model space, the results of RMF-BCS approach is almost similar with the RHB formalism [141, 156–159], as a result one can use the RMF-BCS approximation to get a reasonable description of the nuclei.

2.2.2 Center of Mass Correction ($E_{c.m.}$)

Certainly for light mass nuclei, the correction of center of mass motion can not be ignored and it should be done self-consistently. That means, in the evaluation of center-of-mass energy, one should evaluate $E_{CM} = \frac{<F|P^2|F>}{2M}$ using $|F>=|F>_{RMF}$ wave function. In this case, one has to calculate the matrix elements directly. However, this procedure is more involved and in the present calculations we have subtracted the spurious center-of-mass motion using the Elliott-Skyrme approximation and the approximate analytical expression is written as $E_{CM} = \frac{3}{4}.41A^{-1/3}$ MeV (harmonic oscillator approximation), where A is mass number [34, 148, 149] and expect that the two results should not differ drastically.

2.2.3 Choosing the Basis

For axially deformed system, we expand the wave function in a deformed harmonic oscillator basis. We took the maximum oscillator shells N_F and N_B for Fermionic and Bosonic fields, respectively. The optimal number of oscillator shell depends on the size of the nucleus. Due to the computational time limitation, we use optimal model space. We try to fix these basis space in such that system should converge properly. For this, we calculate the physical observables like binding energy (BE), charge radius (r_{ch}), and deformation parameter (β_2) as functions of basis space. After certain values, the physical observables become insensitive to N_F and N_B, these basis quanta are called optimized basis quanta and rest of the calculations have been performed on these bases.

2.2.4 Blocking Approximation

For even-even nucleus $\pm m$ orbits are pairwise occupied and the mean field has time reversal symmetry. But in the case of odd nucleon, the time reversal symmetry is broken. To take care of the odd nucleon, we employ the blocking method [141]. We put the last nucleon in one of the conjugate states ±m and keeping other state empty. In this way we follow the time reversal symmetry for odd-even and odd-odd nuclei. We repeat this calculation by putting the odd nucleon in all nearby states of the conjugate level to determine the maximum binding energy of the ground state [38, 141].

Chapter 3

Importance of non-linearity in NN Potential

From the relativistic self-coupling scalar meson (non-linear) Lagrangian a new nucleon-nucleon (NN) potential is derived, and is found to be analogous to the widely used M3Y interaction. We investigate the predictive power of RMF theory to reproduce the nuclear ground state properties and surface phenomena like proton radioactivity and cluster-decay problem. The results are found to be reasonable agreement with the M3Y interaction as well as the experimental data.

3.1 Introduction

In the nucleonic regime, nuclei behave as sets of interacting nucleons. In order to go beyond some basic nuclear models which provide a global description of the system, one has to include the elementary interaction between nucleons in the picture. One can then explore how the average potential well, in which nucleons evolve, can be built up from this elementary interaction and thus gain a more microscopic picture of nuclei.Early field theoretical approaches [160] in the 1950's were generally unsuccessful. These eventually gave way to more phenomenological treatments [161] which provided a pragmatic way to describe the abundant NN scattering and bound state (deuteron) data. In the beginning of 1970's many theoretical models emerged which were more successful than the earlier attempts, and were based on one-pion exchange (OPE), heavy meson exchange, and multi-meson exchange [162–165]. A key idea on which more theoretical machinery is founded, is the concept of nuclear mean field, which basically relies on the fact that nucleons move quasi-independently from one another inside a nucleus. Although the mean field underlies many of our discussions, one should not forget the elementary nucleon-nucleon interaction from which it is built. But it is not our aim to discuss here all the works which have been devoted to the NN-interaction. We thus only recall the shape of the interaction with a few gross properties. We content ourselves with noting that the dominant part of the interaction is strongly repulsive at short range ($\leq 0.4 fm$, hard core) and attractive at intermediate range ($\sim 1.0 - 1.2 fm$). This dominant repulsive and attractive interaction is the typical widely used well known M3Y NN-interaction [166]. The NN-interaction can not yet be derived from first principle (QCD). So the existing potentials are thus, at least partly, phenomenological and contain a large number of parameters, which are fitted to deuteron properties and available phase shifts. This fitting procedure does not necessarily ensure a proper reproduction of many-body properties. So for the first time, we try to obtain a NN-interaction (NR3Y) analogous to M3Y derived from the relativistic-mean-field (RMF) theory, which leads to an overall agreement with the ground state bulk properties, compressibility and some radioactive properties of proton drip-line nuclei and super heavy region.

3.1.1 Importance of non-linearity:

It is to be noted that in our recently published work [167], an attempt has been made to simulate the M3Y NN-interaction from a simple Lagrangian [27,28]. However, the value of compressibility obtained is quite large, about 550 MeV (Though it is difficult to determine empirically, it is most probably about 210±30 MeV [133]). Later on its application to finite nuclei [168] shows that the results also deviate far from the experiment. To overcome the above mentioned difficulties, we take the Lagrangian of Boguta and Bodmer [128] who has for the first time included the cubic and quartic terms in the scalar field. Actually, they studied the empirical properties of nuclear matter and finite nuclei without abnormal solution involving the non-linear terms in the original linear $\sigma - \omega$ model of Miller and Green [27]. The binding energy (B.E.), charge radius and deformation parameter (β_2) of finite nuclei from ^{20}Ne to ^{238}U were studied thoroughly and some of them are presented in Fig. 3.1.

Figure 3.1: Relative difference of the ground state B.E., charge radius, and quadrupole deformation parameter of nuclei are compared with experimental data.

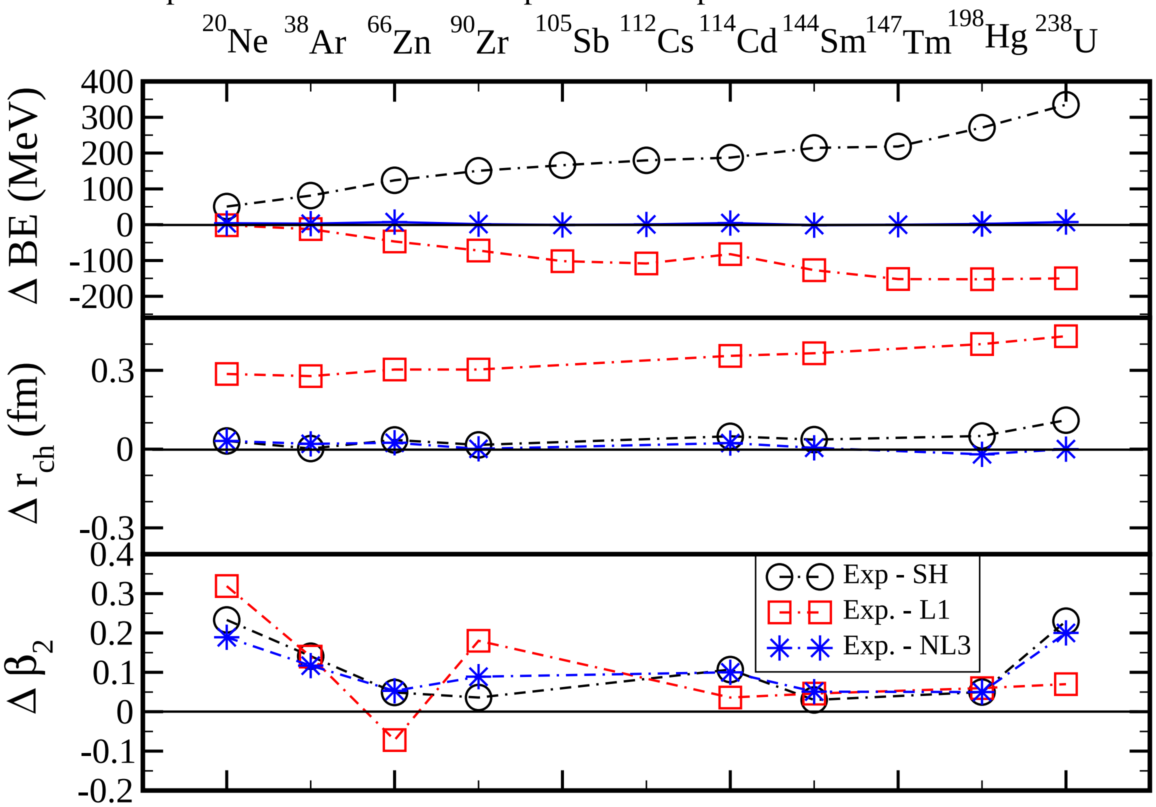

Table 3.1: The binding energy (B.E.), rms charge radius (r_{ch}), nuclear matter Compressibility (K), asymmetry parameter (a_s), ratio of the effective mass and bare nucleon mass ($\frac{m^*}{m}$), and the equation of state (EOS) of infinite nuclear matter are compared in linear and non-linear model.

Observable	Linear σ	Non-linear σ
B.E. and r_{ch} for finite nuclei	can not be reproduced satisfactorily [170]	Excellent agreement [170]
K	~550MeV	210-300 MeV
a_s	22.1 MeV 33.2 MeV (Empirical) [26]	37 MeV [62]
$\frac{m^*}{m}$	0.56 0.6 (Empirical) [26]	0.6 [62]
EOS	Too stiff	Comparatively softer and consistent with empirical result

It is clearly seen from the figure that the linear model (L1), where non-linear self-couplings of the mesons are switched off, gives a modest fit. The experimental data can be reproduced with an average error of above 20% for the energies, 0.7% for the radii, and of above 50% for β_2 parameter. The full parametrization, including the non-linearity (NL3) allows an excellent fit. It reproduces the experimental data within an average error of below 0.3% for energies, of 0.3% for the radii and relatively less error in β_2 parameter. This proves that a relativistic treatment of the nucleus with explicit non-linear mesonic degree-of-freedom is fully capable of reproducing the bulk properties of finite nuclei and its simultaneous explanation of surface phenomena like proton radioactivity is quite impressive over linear (L1) one as will be discussed later. Also the properties of infinite nuclear matter such as radius and mass of the neutron star can not be produced within the experimental range with the linear Walecka model. Again this non-linearity generates analogous effect of the three body interaction due to its off-shell meson couplings which is essential for the saturation properties [32, 169] and we present here a comparative study of involved non-linear terms to the σ-meson with the linear one for clear understanding in Table 3.1.

Therefore, the two non-linear terms are not only mere addition to the Lagrangian, rather they are essential in the Lagrangian to get a proper description of nuclear system. Also the necessity of non-linear σ self-coupling terms have been well addressed by Boguta and Bodmer [128] and of relativistic Brueckner-Hartree-Fock theory of nuclear matter [171]. After adding the non-linear terms in the Lagrangian, the equation for σ-meson turns to a non-linear equation which is not solvable analytically [172]. So, to get a feasible potential, we followed the same procedure of Ref. [33].

It is to be noted that, this can be done numerically using the self-consistent iterative method [38, 172, 173, 173]. Also using these non-linear coupling terms, Bhuyan et al. [104] successfully searched for the proton magic number in the superheavy valley beyond Z = 82 and the corresponding neutron magic number after N = 126 and found justified structural properties. Here, along with the ground state and saturation properties of nuclei, we have tried to explain the surface phenomena with the same NN-interaction. Further, rigorous study of half-lives of proton radioactivity using large number of Skyrme parameter sets by Routray et al. [174] concludes that greater the value of the compressibility, larger the value of half-lives. So, to have reasonable compressibility and effective mass as shown in Table 3.1 the inclusion of cubic and quartic terms in the scalar field is necessary. In fact the linear model (containing only of ω and σ-terms) with L1 parameter set [175] gives undesired depth of the attractive part of the potential as shown in the Fig. 3.2. Although, the HS parameter set gives comparable results of half-lives, it deviates significantly in ground state properties and compressibility as shown in Fig. 3.1 and Table 3.1. However, the nonlinear self-couplings of the scalar field are essential to reach a quantitative description of nuclear properties.

Later on this Lagrangian becomes extremely successful both for finite as well as infinite nuclear matter [170, 176]. Therefore it is interesting to find a NN-interaction from this Lagrangian which can simulate the form of M3Y or R3Y (which was attempted in our earlier work [167]). Further, we employ it for the study of proton radioactivity and compare our results with those based on the phenomenological M3Y effective NN-interaction.

3.2 Theoretical Framework

3.2.1 The relativistic mean field (RMF) theory and the microscopic NN-interaction

In this thesis, rather than using a simple phenomenological prescription [166], we derive the microscopic NN-interaction from the RMF Lagrangian. The attractive long range part of the NN-interaction has long been known to correspond to pion exchange, whereas the ρ and ω correspond to the shorter range part etc. But the complex, multi-meson contributions are furthermore simulated by effective mesons, such as σ meson along with non-linear terms which leads to an overall simple form for the interaction analogous to the widely used M3Y form. Nevertheless, the short range effects (hard core) are yet to be better understood and properly linked to quark degrees of freedom. It is relevant to mention here that the simplified spin and isospin-independent (S=T=0) M3Y effective NN-interaction has been successfully used in a wide number of applications [177–179]. The effective NN-interaction is S(and T) dependent [180, 181] and generally carries three components as:

$$v_{eff} = V^C(r) + V^{LS}(r)\vec{L}.\vec{S} + V^T(r)\hat{S}_{12}, \tag{3.1}$$

where r is the relative distance and $\vec{L}.\vec{S}$ and $\hat{S}_{12}$ are the usual spin-orbit and tensor operators, respectively. The central component [180] is

$$\begin{aligned} V^C(r) &= V_0(r) + V_\sigma(r)\sigma_1.\sigma_2 + V_\tau(r)\tau_1.\tau_2 \\ &\quad + V_{\sigma\tau}(r)(\sigma_1.\sigma_2)(\tau_1.\tau_2), \end{aligned} \tag{3.2}$$

with radial, spin-, isospin-, and spin-isospin-dependent parts, respectively.

The non-linear, relativistic mean field Lagrangian density for a nucleon-meson many-body system [34, 35, 37, 128] is

$$\begin{aligned} L &= \overline{\psi_i}\{i\gamma^\mu\partial_\mu - M\}\psi_i + \frac{1}{2}\partial^\mu\sigma\partial_\mu\sigma - \frac{1}{2}m_\sigma^2\sigma^2 - \frac{1}{3}g_2\sigma^3 - \frac{1}{4}g_3\sigma^4 - g_\sigma\overline{\psi_i}\psi_i\sigma \\ &\quad -\frac{1}{4}\Omega^{\mu\nu}\Omega_{\mu\nu} + \frac{1}{2}m_w^2V^\mu V_\mu - g_w\overline{\psi}_i\gamma^\mu\psi_iV_\mu - \frac{1}{4}\vec{B}^{\mu\nu}.\vec{B}_{\mu\nu} + \frac{1}{2}m_\rho^2\vec{R}^\mu.\vec{R}_\mu \\ &\quad -g_\rho\overline{\psi}_i\gamma^\mu\vec{\tau}\psi_i.\vec{R}^\mu, \end{aligned} \tag{3.3}$$

where, the field for σ meson is denoted by σ, for ω meson by V_μ, and that for the iso-vector ρ by $\vec{R}_\mu$, respectively. The ψ_i are the Dirac spinors for the nucleons and an isospin is denoted by τ. Here, g_σ, g_ω, g_ρ, and g_δ are the coupling constants for σ, ω, and ρ mesons, respectively. M, m_σ, m_ω and m_ρ are the masses of the nucleons, σ, ω, and ρ mesons respectively. $\Omega^{\mu\nu}$ and $\vec{B}_{\mu\nu}$ are the field tensors for the V^μ and $\vec{R}_\mu$, respectively. In this Lagrangian, the contribution of π meson has not been taken into account as, at the mean-field level, its contribution is zero due to its pseudoscalar nature [26,182]. It is essential for quantitative discussions to introduce the self-coupling terms with the coupling constants g_2 and g_3 for the σ meson. The coupling strengths, g's, and the meson masses, m's are the parameters of this theory.

We solve the nuclear system under the mean-field approximation using the above Lagrangian and obtain the field equations for the nucleons and mesons as:

$$\Big(-i\alpha.\bigtriangledown+\beta(M+g_\sigma\sigma)+g_\omega\omega+g_\rho\tau_3\rho_3\Big)\psi_i=\epsilon_i\psi_i, \tag{3.4}$$

$$(-\bigtriangledown^2+m_\sigma^2)\sigma(r)=-g_\sigma\rho_s(r)-g_2\sigma^2-g_3\sigma^3, \tag{3.5}$$

$$(-\bigtriangledown^2+m_\omega^2)V(r)=g_\omega\rho(r), \tag{3.6}$$

$$(-\bigtriangledown^2+m_\rho^2)\rho(r)=g_\rho\rho_3(r), \tag{3.7}$$

respectively, for Dirac nucleons, σ, ω, and ρ mesons.

The interaction between a pair of nucleons, when they are embedded in a heavy nucleus, is less than when they are in empty space. This suppression of the two-body interactions within a nucleus in favor of the interaction of each nucleon with the average nucleon density, means that the non-linearity acts as a smoothing mechanism and hence leads in the direction of the one-body potential and shell structure [183]. Here, we deal with the non-linearity in the meson field, where this is chosen in such a way that the meson field amplitude increases less rapidly than the linear one and the change in meson amplitude produced by the addition or emission of a nucleon is less (may be $1/e$). This sort of effect is needed to account for saturation. Again, the Lagrangian density contains the non-linear coupling function and the non-linear field function where the interaction between two π

meson is less, so that for weak fields the non-linear theory becomes the usual one. Considering for high nucleon density, when nucleon density and σ are large, the non-linear field function is proportional to σ^n where $n \geq 2$. Then the energy per nucleon becomes negative. Since this energy is the average potential energy of a nucleon and its kinetic energy increases with nucleon density, the heavy nuclear system fails to collapse in this approximation. Again, this non-linearity can take any form as it is derived from scalar meson theory in which the non-linearity corresponds to a point-contact repulsion between mesons [33]. So, we take opposite sign to the source term for σ^3 and σ^4 terms, first by using only classical field theory, and second by choosing the mesons to be of the neutral scalar type. This seems a simple and natural form to use, but it brings a serious problem into analysis and the interpretation of the formalism. As far meson production in heavy nuclei is concerned, the outgoing meson wave is much more strongly coupled with the surface than to the interior of the nucleus. So, the expressions for second and third term of Eq. (3.5) should be interpreted in such a way that the nuclear matter acts as a strongly repulsive potential for small-amplitude meson waves and this equivalent repulsion should be conveniently specified in terms of the distance in which the amplitude of an incident meson wave of unit energy is decreased by a factor e. So the solution for second and third term of Eq. (3.5) is taken as [33]:

$$V_\sigma(r) = +\frac{g_2^2}{4\pi} r e^{-2m_\sigma r} \qquad \text{and} \qquad V_\sigma(r) = +\frac{g_3^2}{4\pi}\frac{e^{-3m_\sigma r}}{r} \tag{3.8}$$

to get a new NN-interaction analogous to M3Y form in-order to improve the compressibility and the finite nuclei results which was the deficiency in our earlier work [167]. In addition to this, the self coupling of the σ-meson (non-linear terms) helps to generate the repulsive part of the NN potential at long distance to satisfy the saturation properties and binding energy of nuclear matter at the same time (Coester-band problem) [115, 171]. Again the scalar potential overestimates the Dirac-Brueckner-Hartree-Fock (DBHF) [116, 184–188] results at high density in order to compensate for the strong repulsion in the vector channel. This leads to multi-valued solution and to a very limited physical branch [189]. Adding a quartic vector self interaction remarkably improves the behavior of the vector and scalar potentials, and softens the equation of state [34,35,37], and also produces a NN-interaction analogous with M3Y one. Here, we take into account the non-linear terms in σ field and are able to obtain a similar type of potential with M3Y form. The resultant effective nucleon-nucleon interaction, obtained from the summation of the scalar and vector parts of the single meson fields, is then defined as [27, 29, 182]

$$
\begin{aligned}
v_{eff}(r) &= V_\omega + V_\rho + V_\sigma \\
&= \frac{g_\omega^2}{4\pi}\frac{e^{-m_\omega r}}{r} + \frac{g_\rho^2}{4\pi}\frac{e^{-m_\rho r}}{r} - \frac{g_\sigma^2}{4\pi}\frac{e^{-m_\sigma r}}{r} + \frac{g_2^2}{4\pi} r e^{-2m_\sigma r} + \frac{g_3^2}{4\pi}\frac{e^{-3m_\sigma r}}{r}
\end{aligned}
\tag{3.9}
$$

Table 3.2: The values of m_σ, m_ω, m_ρ, symmetry energy coefficient E_{sym}, nuclear matter compressibility at saturation K_0 (in MeV), nuclear matter saturation density ρ_0 (fm^{-3}) and g_σ, g_ω, g_ρ, effective mass M^*/M for different relativistic mean field (RMF) forces [145]. The dimension of g_2 is fm^{-1} and all other coupling constants are dimensionless. The mass of mesons and symmetry energy are in MeV.

Set	m_σ	m_ω	m_ρ	g_σ	g_ω	g_ρ	g_2 (fm^{-1})	g_3	ρ_0	BE/A	E_{sym}	K_0	M^*/M
HS	520	783	770	10.47	13.80	08.08	–	–	0.147	−15.73	34.9	544.4	0.54
Z	551.31	780	763	11.19	13.83	10.89	–	–	0.151	−17.07	48.8	548.5	0.53
W	550	783	–	09.57	11.67	–	–	–	0.194	−15.75	22.1	544.6	0.56
L1	550	783	–	10.30	12.60	–	–	–	0.152	−18.59	21.7	626.3	0.53
NL3	508.194	782.5	763.0	08.31	13.18	6.37	2.0553	-2.6508	0.148	−16.24	37.0	271.5	0.59

Table 3.3: The energy (in MeV) contribution from different fields of RMF Hamiltonian density with NL3 force [62] for ^{16}O, ^{208}Pb and ^{270}Ds nuclei. The experimental data are given for comparison.

Nucleus	Nucleon Field		Meson Field				Other Field			Total Energy	
	Proton	Neutron	Linear σ	Linear ω	Linear ρ	Non-linear σ	E_{Coul}	E_{pair}	$E_{c.m.}$	E_{total}	$BE_{expt.}$
^{16}O	168.8	200.2	-1860.7	1553.9	0.0	37.4	16.9	0.0	12.2	128.8	127.6
^{208}Pb	1822.4	3045.6	-29513.5	24724.3	104.4	624.4	827.5	0.0	5.2	1640.5	1636.4
^{270}Ds	1900.7	4055.2	-38479.1	32180.2	110.4	845.3	1335.6	14.3	4.8	1967.3	1958.3

The parameters used in Eq. 3.9 are listed in Table 3.2, which are adjusted to reproduce the nuclear matter and finite nuclei properties quite well. That means, using the parameters g_σ, g_ω, g_ρ, g_2, g_3 and m_σ in the equation of motions and equation of state, obtained from the relativistic Lagrangians, one reproduce the experimental data for both finite and infinite nuclear matter systems [36, 38, 170, 176]. It is worthy to mention that, these parameters are used as free parameters in the Lagrangian to reproduce the experimental data and once the parameters are defined, these are fixed for the entire nuclear chart including the nuclear matter domain. This fitting of the parameter sets is nearly similar to the scheme adopted in Ref. [33]. According to Schiff, if the parameters reproduce the nuclear data satisfactorily, then the solution of the non-linear equation can be expressed by the exponential form which we have done in this work, and the final form of the solutions of the coupled linear and non-linear equations is expressed as in Eq. 3.9. Apart from the, the binding energy, i.e. the wave functions for nuclear systems using these parameters, may be another support to the Schiff's prescription [33]. Thus, the B.E. obtained from various contributions of the Hamiltonian for some of the selected nuclei (^{16}O, ^{208}Pb and ^{270}Ds) with SH and NL3 representative forces are listed in Table 3.3. The total binding energy of a nucleus comes out to be a small quantity, which is the summation of energy computed from various terms. From the table, it is clear that the contribution, specially from the linear scalar and vector terms are of the order of several thousands. Hence, a slight error in the coupling constants will create a large instability in the computation of the nuclear observables. Thus, we expect that the parameter sets designed for relativistic mean field formalism are very accurate, which are good enough to use in Eq. 3.9 for any type of applications.

Hence, Eq. 3.9 with the single-nucleon exchange effects [166], becomes:

$$\begin{aligned} v_{eff}(r) &= \frac{g_\omega^2}{4\pi}\frac{e^{-m_\omega r}}{r} + \frac{g_\rho^2}{4\pi}\frac{e^{-m_\rho r}}{r} - \frac{g_\sigma^2}{4\pi}\frac{e^{-m_\sigma r}}{r} \\ &+ \frac{g_2^2}{4\pi} r e^{-2m_\sigma r} + \frac{g_3^2}{4\pi}\frac{e^{-3m_\sigma r}}{r} + J_{00}(E)\delta(s), \end{aligned} \tag{3.10}$$

where $J_{00}(E)\delta(s)$ is the zero range pseudo potential representing EX [166, 190] and is given by:

$$J_{00} = -276(1 - 0.005E/A_{c(\alpha)})MeV fm^3. \tag{3.11}$$

Here, $A_{c(\alpha)}$ is the cluster (or α-particle) mass, and E, the energy measured in the center of mass of the cluster- or α-daughter nucleus system, is equal to the released Q-value.

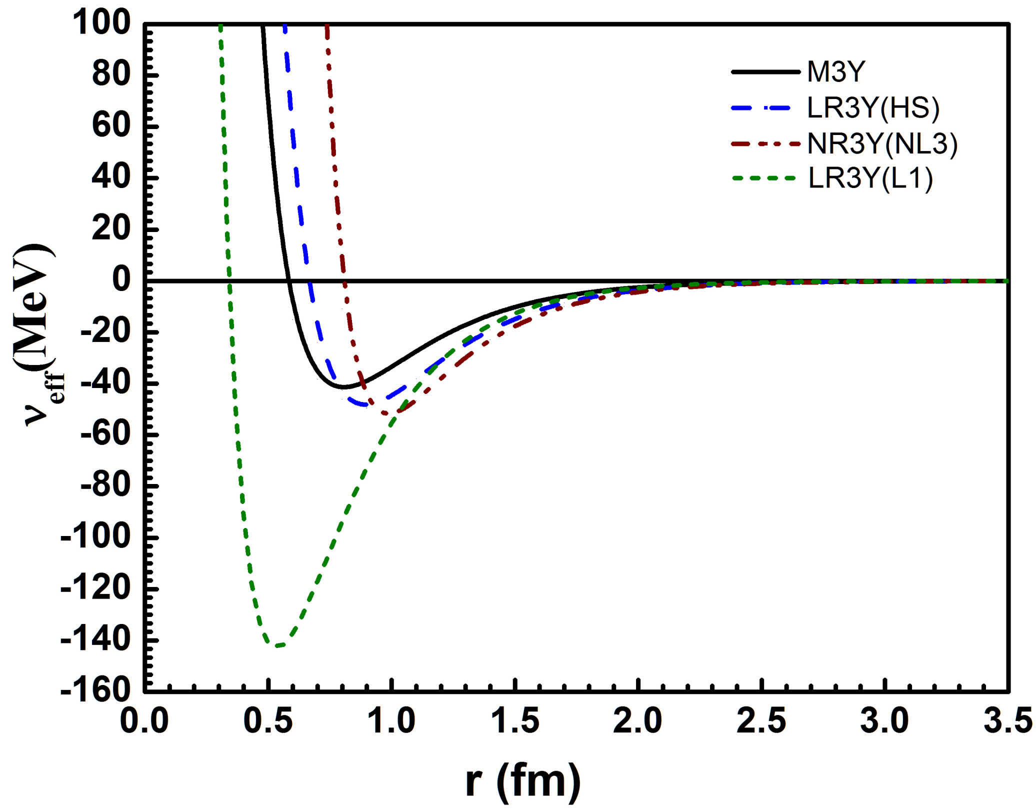

Figure 3.2: The NR3Y and the M3Y effective NN-interaction potentials as a function of r.

As illustrative cases, using in Eq. 3.10 the HS parameters [168], we get:

$$\begin{aligned} v_{eff}(r) &= 11957\frac{e^{-3.97r}}{4r} + 4099\frac{e^{-3.90r}}{4r} \\ &\quad -6883\frac{e^{-2.64r}}{4r} + J_{00}(E)\delta(s), \end{aligned} \tag{3.12}$$

and for NL3 parameters [62], Eq. 3.10 becomes

$$\begin{aligned} v_{eff}(r) &= 10395\frac{e^{-3.97r}}{4r} + 1257\frac{e^{-3.87r}}{4r} - 6554\frac{e^{-2.58r}}{4r} \\ &\quad +6830r\frac{e^{-5.15r}}{4} + 52384\frac{e^{-7.73r}}{4r} + J_{00}(E)\delta(s), \end{aligned} \tag{3.13}$$

and for L1 parameters [175] containing only ω and σ terms, Eq. 3.9 becomes

$$v_{eff}(r) = 9968\frac{e^{-3.97r}}{4r} - 6661\frac{e^{-2.79r}}{4r}, \tag{3.14}$$

with the corresponding effective NN-interaction potentials, denoted LR3Y(HS), NR3Y(NL3) and LR3Y(L1), etc., as shown in Fig. 3.2, together with other effective NN-interaction potentials, like M3Y without the one-pion exchange potential (OPEP) term, is given by:

$$v_{eff}(r) = 7999\frac{e^{-4r}}{4r} - 2134\frac{e^{-2.5r}}{2.5r}, \tag{3.15}$$

where ranges are in fm and the strength in MeV.

However, to take care OPEP we have added J_{00} term as it is done in Eq. 3.10 while calculating the nuclear potential. This M3Y effective interaction, obtained from a fit of the G-matrix elements based on Reid-Elliott soft-core NN-interaction [166], in an oscillator basis, is the sum of three Yukawa's with ranges 0.25 fm for a medium-range attractive part, 0.4 fm for a short-range repulsive part and 1.414 fm to ensure a long-range tail of the OPEP. It should be noted that Eq. 3.13 represents the spin- and isospin-independent parts of the central component of the effective NN-interaction [Eqs. 3.1 and 3.2], and that the OPEP contribution is absent here. Comparing Eqs. 3.12 and 3.13 with 3.15, we find very similar behavior of the NN-interactions derived from RMF theory in Fig. 3.2, which supports the belief that Eq. 3.10 can be used to obtain the nucleus-nucleus optical potential.

We know that in the mean field the expectation value of the pion potential is zero because of the definite parity of the ground state nucleus (The OPEP is purely S = T = 1.) (psuedoscalar nature of pion) [26]. Of course this contribution of pion should be taken care if one will go beyond mean field to account for the long range nuclear forces. In Fig. 3.2, we have shown the effective NN-interactions given by Eqs. 3.12-3.15 without the exchange term J_{00}. While we have considered $J_{00} \approx -276 MeV fm^3$ representing EX [166] in calculating the half-lives because the second bracketed term $(0.005E/A_{c(\alpha)})$ in equation 3.11 has negligible value. If we take pure linear term even without ρ-meson coupling (Eq. 3.14, (for example L1 parameter set) we will get the depth of NN potential around ~142 MeV as shown in Fig. 3.2 which is an extremely high value. However, we have corrected it by inserting ρ-meson coupling terms in HS-parameter set. Using the optical potentials so obtained, we demonstrated in the next sub-section, the applications of Eqs. (3.10, 3.12, 3.13) and (3.15) to various nuclear systems for evaluating some of the physical observables in the phenomenon of exotic proton and cluster radioactivity (CR).

3.2.2 Optical potential and the half-lives study using the preformed cluster model (PCM)

The nuclear interaction potential $V_n(R)$ between the cluster (c) and daughter (d) nuclei, using the well known double folding procedure [166] and by single folding, with the respective RMF calculated nuclear matter densities ρ_c and ρ_d for M3Y forces is given as:

$$V_n(\vec{R}) = \int \rho_c(\vec{r}_c)\rho_d(\vec{r}_d)v_{eff}(|\vec{r}_c - \vec{r}_d + \vec{R}|{\equiv}r)d^3r_c d^3r_d, \tag{3.16}$$

and

$$V_n(\vec{R}) = \int \rho_d(\vec{r})v(|\vec{r} - \vec{R}|)d^3r. \tag{3.17}$$

Adding Coulomb potential $V_C(R)$ (=$Z_d Z_c e^2/R$) and centrifugal potential wherever necessary the scattering potential is obtained as

$$V(R) = V_N(R) + V_C(R) + \frac{\hbar^2 L(L+1)}{2\mu R^2}, \tag{3.18}$$

where R is the separation between the mass center of the residual daughter nucleus and the emitted proton/cluster, L is the angular momentum of emitted proton in the case of proton radioactivity. The density distribution function ρ has been calculated using RMFT formalism [26, 38, 145, 168], in which an effective Lagrangian is taken to describe the nucleons interaction through the effective meson and electromagnetic (e.m.) fields. The decay constant λ or half-life time $T_{1/2}$ in the preformed cluster model (PCM) of Gupta and collaborators [191, 192] is defined as:

$$\lambda_{PCM} = \frac{\ln 2}{T_{1/2}} = \nu_0 P_0 P, \tag{3.19}$$

with the "assault frequency" ν_0, i.e., the frequency with which the cluster hits the barrier, given by:

$$\nu_0 = \frac{velocity}{R_0} = \frac{(2E_c/\mu)^{1/2}}{R_0}. \tag{3.20}$$

Here, R_0 is the radius of parent nucleus and E_c is the kinetic energy of the emitted cluster. P_0 is the preformation probability and has been taken as unity in our calculations. P is the WKB penetration probability of the cluster tunneling through the interaction potential $V(R)$ and is given by the WKB integral:

$$P = exp[-\frac{2}{\hbar}\int_{R_a}^{R_b} \{2\mu[V(R) - Q]\}^{1/2} dR], \tag{3.21}$$

with R_a and R_b as the first and second turning points, satisfying $V(R_a) = V(R_b) = Q$, $\mu = A_d A_c/(A_d + A_c)$, the reduced mass, and $Q = BE_p - (BE_d + BE_c)$, where BE_p, BE_c and BE_d are the experimental ground-state (gs) binding energies of the parent, cluster and daughter nuclei, taken from Audi and Wapstra [193].

We have also successfully demonstrated its application (with HS parameter set) to study the half-life of proton decay [194] and a recent study of the half-life of α-decay [195] with the fusion cross section of heavy-ion systems using the region wise absorption method [196]. It is clearly seen from Fig. 4 of Ref. [195] that the barrier (for l=0) position and height play significant roles, not only in the study of fusion cross sections of heavy nucleus but also in half-life study of proton decay [194] and $\alpha-$decay [195]. So, to check the applicability of the present formalism, we study the proton and cluster decay of heavy nuclei in the next section.

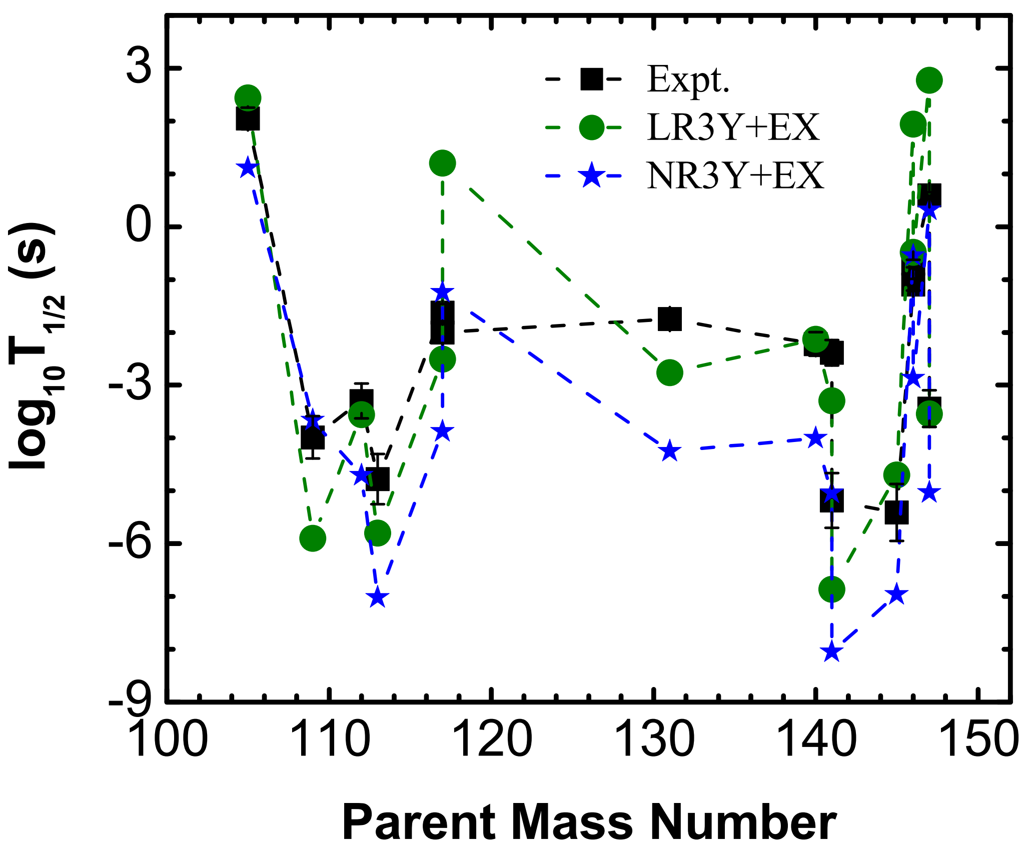

Figure 3.3: Half-lives for proton radioactivity of proton rich parent nuclei.

Table 3.4: The calculated half-lives of proton emitters are presented using M3Y+EX and NR3Y+EX NN-interactions. The results of the calculations have been compared with the experimental values and with the results of [197, 198]. The experimental Q values, half-lives, and l values are taken from [197]. The asterisk symbol $(\star)$ denotes the isomeric state.

Parent	Q	Ang. momentum	$Expt.$	$(M3Y+EX)$ HS	$(LR3Y+EX)$ HS	$(M3Y+EX)$ $NL3$	$(NR3Y+EX)$ $NL3$	[197]	[198]
nuclei	(MeV)	L	$log_{10}T(s)$	$log_{10}T(s)$	$log_{10}T(s)$	$log_{10}T(s)$	$log_{10}T(s)$		
^{105}Sb	0.491	2	2.049	3.070	2.436	3.100	1.113	2.085	1.970
^{109}I	0.819	0	-3.987	-5.627	-5.897	-5.593	-6.941	–	–
		2				-5.522	-3.666	–	–
^{112}Cs	0.814	2	-3.301	-2.857	-3.555	-2.835	-4.705	–	–
^{113}Cs	0.973	2	-4.777	-5.236	-5.803	-5.204	-7.017	–	–
^{117}La	0.803	2	-1.628	-1.943	-2.504	-1.922	-3.878	–	–
^{117}La*	0.954	5	-2.000	2.794	1.203	–	-1.241	–	–
		4				-0.226	-3.266	–	–
^{131}Eu	0.940	2	-1.749	-2.097	-2.764	-2.085	-4.256	–	–
^{140}Ho	1.094	3	-2.221	-1.374	-2.132	-1.376	-4.007	–	–
^{141}Ho	1.177	3	-2.387	-2.487	-3.298	-2.468	-5.038	–	–
^{141}Ho*	1.256	0	-5.180	-6.374	-6.846	-6.366	-8.047	–	–
^{145}Tm	1.753	5	-5.409	-3.415	-4.698	-3.278	-6.962	-5.170	-5.140
^{146}Tm	1.127	5	-1.096	3.384	1.945	3.51	-0.547	–	–
^{146}Tm*	1.307	5	-0.698	0.919	-0.484	1.043	-2.870	–	–
^{147}Tm	1.071	5	0.591	4.191	2.775	4.369	0.315	1.095	0.980
^{147}Tm*	1.139	2	-3.444	-2.916	-3.546	-2.963	-5.036	-3.199	-3.390

3.3 Results and Discussions

The new formalism has been applied to some highly unstable proton rich trans-tin nuclei with the above mentioned PCM of Gupta et al. [191, 192]. Though the study of proton radioactivity provides nuclear structure information on nuclides lying beyond the proton drip-line, it also yields the information on the angular momentum carried off by the proton [199]. Further, the conservation of angular momentum only allows decay to the ground state, with no possibility of calculating decay to excited states of the daughter [200]. So to relate the calculated and experimental decay rates, an adjustment of spectroscopic factor is needed [201]. This may be (i) due to deformed nucleus, where the decaying Nilsson level is close to the Fermi surface and (ii) the probability of that particular level is unoccupied in the daughter nucleus. This indicates that the interaction between the last proton and the core nucleus should include particle-vibration coupling [201] for better agreement between calculated and experimental results. Nevertheless, without this particle-vibration couplings our present formalism simply with the inclusion of non-linear terms in σ meson, shows reasonable agreement with the experimental data as well as our earlier work with RMFT-HS densities given in Table 3.4 simultaneously with the finite nuclear properties shown in Figs. 3.1 and 3.3. It is observed that, in few of the cases the LR3Y+EX gives superior or comparable results. This implies the charge particle or cluster decay property is less sensitive to the compressibility. Also, perhaps this value is indifferent to the detail nuclear structure inherited by the density while calculating the proton and cluster decay property (mostly a surface phenomena).

However, if one applies these folding potential to some other nuclear phenomena where structural property of the nuclei given in Table 3.1 and in Fig. 3.1 are important, the NR3Y+EX may work better. This is because of better predictive power of NL3 [62] over HS [168] throughout the periodic table. In addition to the shifting of barrier position and height, the effect of various model parameters can not be neglected as one can observe from the fifth and seventh column of Table 3.2 and from Fig. 3.1. We also study the sensitivity of half-lives to the orbital angular momentum L as we have clearly shown in Fig. 3 of Ref. [194]. Here for the case ^{109}I and ^{117}La* we study the half-lives for different L and it is seen that NR3Y+EX NN-interaction gives remarkably good result with the experiment, in fact the Q value is very compatible with the half-life.

Further, the self mesonic field of a nucleon within a nucleus is much smaller in spatial extent than it is in empty space. This may also account for the observed deviations in surface phenomena like proton radioactivity as we know the outgoing meson wave is much more strongly coupled to the surface than to the interior of the nucleus.

3.4 Summary and Conclusions

In conclusion, the reported NN-potential denoted here as NR3Y is presented eloquently in terms of the well known inbuilt RMF parameters. Furthermore, in terms of the nucleus-nucleus folding optical potential, we have generated a bridge between the NR3Y and M3Y which can be considered as an unification of the RMF model to predict the nuclear cluster decay properties. Here, we explain the proton decay properties of nuclei by using the RMF-derived NR3Y potential instead of the phenomenological M3Y interaction and found comparable results with the experimental data.

Although, the decay property which we have shown are mostly the surface phenomena, we get similar results with and without non-linear couplings. It is worthy to mention here that from Fig. 3.2, it is clearly seen that after $2.0 fm$, all the potentials follow same trends and merge almost at the same point, where the proton radioactivity takes place. So, a good set of parameters describing the density at the tail region may produce the half-lives close to the experimental data. However, these non-linear coupling have important role for many observables and some of them are listed in Table 3.1 and also shown in Fig. 3.1. Particularly, to obtain the phenomenological compressibility value of 210$\pm$30 MeV along with the other basic structure phenomena, we simply take into account the non-linear terms in σ-meson coupling which gives a new form of NN-interaction alternate to the popular M3Y potential. In future, the situation will become more clear with the availability of more precise experimental data on energies and half-lives, as well as additional examples of charge particle and also cluster emitters.

Chapter 4

Superdeformed structures and low Ω parity doublet in Ne$-$S nuclei near neutron drip-line

4.1 Introduction

The structure of light nuclei near the neutron drip-line is one of the interesting topics for a good number of exotic phenomena. Nuclei in this region are quite different in collectivity and clustering features than the stable counterpart in the nuclear chart. For example, the neutron magic property is lost for N = 8 in ^{12}Be [202] and N = 20 in ^{32}Mg [203]. The unexpectedly large reaction cross-section for ^{22}C gives the indication of neutron halo structure [204]. The discovery of large collectivity of ^{34}Mg by Iwasaki et al. [205] is another example of such exotic properties. The deformed structures, core excitation and the location of drip-line for Mg and neighboring nuclei are interesting properties of investigation. In this context, the discovery of ^{40}Mg and ^{42}Al, which predicted to be nuclei beyond the drip-line by various mass formulae [206,207], show the need to modify the of mass models.

On the other hand, the appearance of N = 16 as a magic number in ^{24}O and the existence of neutron halo in ^{11}Li are established observations [208]. However, the proposed proton [209] (^{8}B) and neutron [210,211] halo (^{14}Be, ^{17}B, ^{31}Ne) in the exotic nuclei are currently under investigations. In addition to these, the cluster structure of the entire light mass nuclei and the skin formation in neutron-drip isotopes motivate us for the study of light mass drip-line nuclei. In this chapter, our aim is to study the neutron drip-line for Ne$-$S isotopic chain in the frame-work of a relativistic mean field (RMF) and non-relativistic Skyrme-Hartree-Fock (SHF) formalisms. We use NL3 parameter [62] for RMF and SkI4 parameters [120] for SHF formalism for the calculations.

4.1.1 Pairing correlation

We find that, for this lighter mass region of the periodic chart, pairing is less important for majority of the cases. With pairing, the deformation becomes negligible for ^{20}Ne and we do not get the experimental deformation parameter in RMF calculations. With no pairing, we reproduce substantially the deformation parameter in RMF because the *density of states* near Fermi surface for such light nuclei are small and not conducive to pairing [212]. To understand the influence of pairing on the open shell nuclei, we have taken into account the experimental data, wherever available. The SHF(SkI4) results are used as guideline in the absence of these data. We found, after comparing the calculated β_2 of RMF and SHF with experimental data, that the quadrupole deformation of SHF is closer to experiment without taking pairing correlation into account. For example, when we use the $\triangle_n$ and $\triangle_p$ from the experimental binding energy of odd-even values or from the empirical formula of Refs. [152, 213] to calculate β_2 for ^{20,22,24,26,28}Ne in RMF(NL3), we find $\beta_2 \sim 0.18, 0.35, 0.19, 0.0, 0.0$, respectively. The results for these isotopes agree with prediction of Lalazissis et al. [214]. These β_2 strongly disagree with the measured values ($\beta_2(expt.) = 0.723, 0.562, 0.45, 0.498, 0.50$) [215]. Similar effects are also seen in other considered isotopes. On the other hand, if we ignore pairing, then the calculated results are often better and these β_2 are quite close to the experimental data. The influence of pairing is also visible in the total binding energy. In some of the cases, even a couple of MeV difference in total binding energy is found with and without taking pairing correlation into account in RMF formalism.

4.1.2 Pauli Blocking and Harmonic oscillator basis

In our calculations, the nuclei are treated as axial-symmetrically deformed, with z-axis as the symmetric axis. Spherical symmetry is no longer present in general and therefore j is not a good quantum number any more. Because of axial symmetry, each orbit is denoted by the quantum number m of J_z and is a superposition of $|jm>$ states with various j values. The densities are invariant with respect to a rotation around the symmetry axis. For numerical calculations, the wave functions are expanded in a deformed harmonic oscillator potential basis and solved self-consistently in an iteration method. The major oscillator quanta for Fermions N_F and Bosons N_B are taken as N_{max}=12.

4.2 Results and Discussions

The binding energy BE, rms charge radius r_{ch} and quadrupole deformation parameter β_2 of the isotopes of Ne, Na, Mg, Al, Si, P and S are calculated near the drip-line region. For this, both the relativistic and non-relativistic models are used.

4.2.1 Binding energy and neutron drip-line

The ground state binding energy (BE) for Ne, Na, Mg, Al, Si, P and S isotopes are selected by comparing the binding energy obtained from the prolate, oblate and spherical solutions for a particular nucleus. For a given nucleus, the maximum binding energy corresponds to the ground state and other solutions are obtained as various excited intrinsic states. In Table 4.1, the ground state binding energy for the heaviest known isotopes for the discussed nuclei are compared with the experimental data [216]. The binding energy for ^{31}Ne is 216.0 MeV with RMF (NL3) and these are 213.2 and 211.4 MeV in SHF(SkI4) and experiment, respectively. Similarly, these results for ^{45}S respectively are 353.4, 350.4 and 354.7 MeV in RMF, SHF and experiment. Analyzing the data of Table 4.1, generally one finds that BE of RMF is slightly over estimated and SHF is underestimated than the experimental values. However, the overall agreement of the calculated energies are within an acceptable range with the experimental data.

We have listed the neutron drip-lines in Table 4.2, which are obtained from the ground state binding energy for neutron rich Ne, Na, Mg, Al, Si, P and S nuclei. The drip-line is determined by setting the condition that the minimum value of two neutron separation energy $S_{2n} = BE(N,Z) - BE(N-2,Z) \geq 0$. The nuclei with the largest neutron numbers so far experimentally detected in an isotopic chain along with the extrapolated data are also displayed in the last column of Table 4.2. The numbers given in the parenthesis

Table 4.1: The calculated ground state binding energy obtained from SHF and RMF theory are compared with the experimentally known heaviest isotope for Ne, Na, Mg, Al, Si, P and S [216]. All the values are in MeV.

Nucleus	RMF	SHF	Expt.	Nucleus	RMF	SHF	Expt.
^{31}Ne	216.0	213.2	211.4±1.6	^{32}Na	234.5	233.4	230.9±0.1
^{36}Mg	263.9	260.2	260.8±0.5	^{38}Al	283.5	281.4	280.3±0.3
^{41}Si	310.1	307.2	307.9±0.4	^{43}P	331.7	329.0	330.7±0.4
^{45}S	353.4	350.4	354.7±0.7				

Table 4.2: The predicted mass number of neutron drip-line for Ne, Na, Mg, Al, Si, P and S nucleus in RMF (NL3) and SHF (SKI4) parameter sets are compared with infinite nuclear matter (INM) mass model [217], finite range droplet model (FRDM) [107] and the nuclei with the largest neutron numbers so far experimentally detected [216] along with the number shown in parenthesis are the experimentally extrapolated values.

Nucleus	RMF	SHF	INM	FRDM	Expt.
Ne	34	34	34	33	31 (34)
Na	40	37	37	36	32 (37)
Mg	40	40	39	40	36 (40)
Al	48	48	42	42	38 (43)
Si	54	48	45	43	41 (45)
P	54	55	49	48	43 (47)
S	55	55	51	51	45 (49)

are the experimentally extrapolated values [216]. To get a qualitative understanding of the prediction of neutron drip-line, we have compared our results with the infinite nuclear matter (INM) [217] model and finite range droplet model (FRDM) [107] mass estimation. The RMF and SHF drip-lines coincide with each other for Ne, Mg, Al and S. In case of Na and Si the RMF drip nuclei are found to be 3 and 6 unit heavier than the SHF prediction. The INM predictions of drip-line nuclei always on the higher side than FRDM. From Table 4.2, we find that the experimental effort has almost reached to the INM and FRDM prediction of drip nuclei for lighter mass region.

The theoretical predictions of drip nuclei are very important after the discovery of ^{40}Mg

Table 4.3: The calculated value of charge radius (r_{ch}) in fm, quadrupole moment deformation parameter β_2 and binding energy (BE) in MeV for Ne, Na and Mg nuclei in RMF (NL3) and SHF (SkI4) formalisms. We compare our results with experimental β_2 [215], ground state binding energy BE [216] and the charge radius r_{ch} [219].

Nucleus	RMF (NL3)			SHF (SkI4)			Exp.		
	r_{ch}	β_2	BE	r_{ch}	β_2	BE	r_{ch}	β_2	BE
^{20}Ne	2.970	0.535	156.7	3.030	0.550	156.8	3.006	0.727	160.6
^{21}Ne	2.953	0.516	165.9	3.012	0.529	166.8	2.970		167.4
^{22}Ne	2.940	0.502	175.7	3.010	0.520	175.8	2.953	0.562	177.8
^{23}Ne	2.913	0.386	181.8	2.975	0.382	182.2	2.910		183.0
^{24}Ne	2.881	-0.259	189.1	2.950	-0.250	188.5	2.901	0.45	191.8
^{25}Ne	2.907	0.272	194.2	2.948	0.170	194.2	2.932		196.0
^{26}Ne	2.926	0.277	199.9	2.950	0.120	199.4	2.925	0.498	201.6
^{27}Ne	2.945	0.247	203.9	2.987	0.159	203.2			203.1
^{28}Ne	2.965	0.225	208.2	3.010	0.160	206.5	2.964	0.50	206.9
^{29}Ne	2.981	0.161	211.2	3.027	0.010	210.1			207.8
^{30}Ne	2.998	0.100	215.0	3.050	0.000	213.7			211.3
^{31}Ne	3.031	0.244	216.0	3.057	0.225	213.2			211.4
^{32}Ne	3.071	0.373	218.6	3.100	0.380	213.1			
^{33}Ne	3.095	0.424	219.5	3.148	0.429	213.5			
^{34}Ne	3.119	0.473	220.9	3.180	0.490	213.5			
^{24}Na	2.964	0.379	192.3	3.042	0.411	194.0	2.974		193.5
^{25}Na	2.937	0.273	200.6	3.024	0.314	201.4	2.977		202.5
^{26}Na	2.965	0.295	207.1	3.027	0.274	208.4	2.993		208.1
^{27}Na	2.993	0.323	214.2	3.043	0.282	214.9	3.014		214.8
^{28}Na	2.993	0.272	219.0	3.058	0.234	219.7	3.040		218.4
^{29}Na	3.004	0.232	224.3	3.072	0.194	224.3	3.092		222.8
^{30}Na	3.031	0.169	228.1	3.079	0.030	228.6	3.118		225.1
^{31}Na	3.047	0.108	232.7	3.103	0.000	233.5	3.170		229.3
^{32}Na	3.077	0.237	234.5	3.121	0.187	233.4			230.9
^{33}Na	3.113	0.356	237.9	3.172	0.352	234.9			
^{34}Na	3.137	0.404	239.8	3.198	0.407	236.2			
^{35}Na	3.161	0.450	242.3	3.224	0.457	237.4			
^{36}Na	3.175	0.481	242.5	3.235	0.501	237.5			
^{37}Na	3.190	0.512	243.1	3.251	0.541	237.6			
^{38}Na	3.199	0.491	243.4						
^{39}Na	3.209	0.472	244.1						
^{40}Na	3.228	0.477	243.4						
^{24}Mg	3.043	0.487	194.3	3.130	0.520	195.2	3.057	0.605	198.3
^{25}Mg	3.009	0.376	202.9	3.103	0.432	204.3	3.028		205.6
^{26}Mg	2.978	0.273	212.5	3.080	-0.300	213.2	3.034	0.482	216.7
^{27}Mg	3.015	0.310	220.2	3.096	0.339	221.5			223.1
^{28}Mg	3.048	0.345	228.7	3.110	0.340	229.0		0.491	231.6
^{29}Mg	3.055	0.289	234.3	3.118	0.283	235.0			235.3
^{30}Mg	3.062	0.241	240.5	3.120	-0.180	240.5		0.431	241.6
^{31}Mg	3.075	0.179	245.1	3.123	0.030	246.1			243.9
^{32}Mg	3.090	0.119	250.5	3.150	0.000	252.0		0.473	249.7
^{33}Mg	3.117	0.233	253.1	3.165	0.155	253.0			252.0
^{34}Mg	3.150	0.343	257.3	3.210	0.330	255.1			256.7
^{35}Mg	3.173	0.388	260.5	3.239	0.393	257.8			257.5
^{36}Mg	3.198	0.432	263.9	3.265	0.440	260.2			260.8
^{37}Mg	3.212	0.462	264.9	3.279	0.469	261.0			
^{38}Mg	3.227	0.492	266.3	3.295	0.490	261.6			
^{39}Mg	3.237	0.473	267.8	3.307	0.485	262.4			
^{40}Mg	3.247	0.456	269.7	3.320	0.470	262.8			

Table 4.4: Same as Table 4.3, for Al and Si isotopes.

Nucleus	RMF			SHF			Exp.		
	r_{ch}	β_2	BE	r_{ch}	β_2	BE	r_{ch}	β_2	BE
^{24}Al	3.097	0.388	182.3	3.174	0.413	185.0			183.6
^{25}Al	3.072	0.381	197.7	3.164	0.430	199.5			200.5
^{26}Al	3.052	-0.275	207.8	3.122	0.315	211.4			211.9
^{27}Al	3.053	-0.292	221.9	3.092	0.204	222.7	3.061		225.0
^{28}Al	3.037	-0.208	238.6	3.105	0.202	232.5			232.7
^{29}Al	3.033	-0.141	245.6	3.126	0.241	241.5			242.1
^{30}Al	3.070	-0.184	253.8	3.139	0.194	248.7			247.8
^{31}Al	3.101	-0.205	259.8	3.161	-0.192	256.0			255.0
^{32}Al	3.103	-0.111	261.2	3.162	0.020	262.6			259.2
^{33}Al	3.165	-0.333	269.4	3.183	0.000	269.8			264.7
^{34}Al	3.134	-0.108	275.1	3.198	0.090	271.7			267.3
^{35}Al	3.167	0.268	274.1	3.229	0.250	274.4			272.5
^{36}Al	3.173	-0.189	277.7	3.254	0.320	277.4			274.4
^{37}Al	3.208	0.355	281.5	3.278	0.371	280.1			278.6
^{38}Al	3.214	-0.254	283.5	3.288	0.378	281.4			280.3
^{39}Al	3.236	-0.299	286.7	3.383	-0.121	287.1			
^{40}Al	3.257	-0.336	290.4	3.316	0.403	284.2			
^{41}Al	3.278	-0.370	290.6	3.338	-0.367	285.9			
^{42}Al	3.281	-0.355	291.2	3.341	-0.339	286.2			
^{43}Al	3.282	-0.338	292.2	3.341	-0.312	286.6			
^{44}Al	3.274	-0.288	293.6	3.340	-0.282	287.0			
^{45}Al	3.271	-0.263	293.5	3.338	-0.250	287.6			
^{46}Al	3.359	0.341	294.5	3.326	-0.129	287.7			
^{47}Al	3.246	0.090	294.8	3.318	-0.004	288.7			
^{48}Al	3.319	-0.252	294.0	3.347	-0.060	287.6			
^{28}Si	3.122	-0.331	232.1	3.190	-0.350	233.6	3.122	0.407	236.5
^{29}Si	3.035	0.001	240.7	3.176	-0.272	243.1	3.118		245.0
^{30}Si	3.070	0.148	250.6	3.170	-0.210	252.6	3.134	0.315	255.6
^{31}Si	3.108	-0.180	259.1	3.182	-0.199	261.7			262.2
^{32}Si	3.137	-0.201	268.5	3.200	-0.200	270.5		0.217	271.4
^{33}Si	3.131	-0.084	275.6	3.196	0.010	278.1			275.9
^{34}Si	3.148	0.000	284.4	3.220	0.000	286.3		0.179	283.4
^{35}Si	3.161	-0.083	287.4	3.226	0.010	289.5			285.9
^{36}Si	3.186	-0.162	291.5	3.150	0.150	292.4		0.259	292.0
^{37}Si	3.200	0.238	295.4	3.269	0.247	295.9			294.3
^{38}Si	3.218	0.281	299.8	3.290	0.310	298.2		0.249	299.9
^{39}Si	3.224	0.263	302.4	3.298	0.292	301.4			301.5
^{40}Si	3.272	-0.301	306.0	3.310	-0.280	304.0			306.5
^{41}Si	3.295	-0.336	310.1	3.349	-0.329	307.2			307.9
^{42}Si	3.318	-0.369	314.6	3.330	-0.350	310.0			
^{43}Si	3.320	-0.356	315.2	3.377	-0.339	311.1			
^{44}Si	3.322	-0.342	316.2	3.380	-0.300	311.6			
^{45}Si	3.316	-0.308	317.5	3.374	-0.282	312.9			
^{46}Si	3.303	-0.262	319.3	3.370	-0.240	313.5			
^{47}Si	3.345	-0.298	319.8	3.340	0.030	314.3			
^{48}Si	3.263	0.001	321.8	3.350	0.000	315.4			
^{49}Si	3.290	0.045	321.1						
^{50}Si	3.341	-0.159	321.5						
^{51}Si	3.358	-0.135	321.2						
^{52}Si	3.371	0.082	321.4						
^{53}Si	3.391	0.042	321.6						
^{54}Si	3.415	0.000	322.3						

Table 4.5: Same as Table 4.3, for P and S isotopes.

Nucleus	RMF			SHF			Exp.		
	r_{ch}	β_2	BE	r_{ch}	β_2	BE	r_{ch}	β_2	BE
^{30}P	3.138	0.130	246.3	3.189	0.026	249.9			250.6
^{31}P	3.158	0.205	258.3	3.201	0.105	261.1	3.189		262.9
^{32}P	3.174	-0.143	267.1	3.216	0.069	270.9			270.9
^{33}P	3.201	-0.183	277.5	3.246	-0.167	280.5			281.0
^{34}P	3.201	-0.082	285.8	3.248	0.001	289.9			287.2
^{35}P	3.216	-0.001	295.4	3.265	0.000	299.2			295.6
^{36}P	3.227	0.120	299.5	3.272	0.007	303.3			299.1
^{37}P	3.246	0.209	305.0	3.290	0.148	307.4			305.9
^{38}P	3.260	0.250	310.4	3.313	0.240	311.7			309.6
^{39}P	3.275	0.288	316.1	3.334	0.301	316.1			315.9
^{40}P	3.281	0.274	320.1	3.343	0.290	319.6			319.2
^{41}P	3.288	0.261	324.4	3.355	0.295	322.7			324.2
^{42}P	3.306	0.301	327.3	3.371	0.320	325.6			326.3
^{43}P	3.346	-0.323	331.7	3.398	-0.320	329.0			330.7
^{44}P	3.346	-0.302	333.3	3.398	-0.293	330.6			
^{45}P	3.315	0.222	335.4	3.397	-0.264	332.4			
^{46}P	3.342	-0.251	337.5	3.397	-0.237	334.2			
^{47}P	3.341	-0.232	340.0	3.399	-0.218	336.0			
^{48}P	3.381	-0.271	341.2	3.379	0.034	337.4			
^{49}P	3.328	0.088	343.2	3.387	0.012	339.3			
^{50}P	3.353	0.101	343.7	3.414	-0.061	339.2			
^{51}P	3.397	-0.166	344.7	3.437	0.068	339.4			
^{52}P	3.403	0.109	345.2	3.462	0.079	339.7			
^{53}P	3.428	0.109	346.3	3.487	0.089	340.1			
^{54}P	3.447	0.074	346.6	3.502	0.016	340.5			
^{55}P	3.468	0.037	347.4	3.525	0.001	341.2			
^{33}S	3.241	0.197	275.5	3.276	0.119	278.9			280.4
^{34}S	3.257	-0.168	286.5	3.300	-0.160	289.3	3.285	0.252	291.8
^{35}S	3.260	-0.078	295.7	3.300	-0.006	299.6			298.8
^{36}S	3.273	0.002	306.2	3.310	0.000	309.6	3.299	0.168	308.7
^{37}S	3.285	0.152	311.6	3.319	-0.008	315.1			313.0
^{38}S	3.300	0.228	318.6	3.340	0.210	320.2		0.246	321.1
^{39}S	3.312	0.264	325.3	3.354	0.248	326.5			325.4
^{40}S	3.325	0.299	332.4	3.370	0.300	332.1		0.284	333.2
^{41}S	3.331	0.287	337.7	3.381	0.294	336.9			337.4
^{42}S	3.338	0.277	343.2	3.390	0.290	341.0		0.300	344.1
^{43}S	3.359	0.318	347.2	3.413	0.326	344.7			346.7
^{44}S	3.381	0.367	351.0	3.440	0.370	348.3		0.254	351.8
^{45}S	3.375	0.312	353.4	3.430	0.311	350.4			354.7
^{46}S	3.371	0.258	356.6	3.420	0.250	352.5			
^{47}S	3.385	0.257	358.5	3.428	-0.214	354.8			
^{48}S	3.400	0.259	360.8	3.430	-0.200	356.6			
^{49}S	3.403	0.227	362.9	3.430	0.127	358.8			
^{50}S	3.403	0.189	365.5	3.440	0.120	360.8			
^{51}S	3.427	0.188	366.4	3.459	-0.090	361.8			
^{52}S	3.451	0.183	367.6	3.490	-0.140	362.5			
^{53}S	3.463	0.158	369.1	3.508	-0.113	363.6			
^{54}S	3.477	0.139	371.0	3.530	0.000	364.7			
^{55}S	3.494	0.105	371.4	3.541	0.030	365.4			

and ^{42}Al [206]. These two nuclei are considered to be beyond the drip-line (neutron-unbound) in some of the mass calculations [207, 218]. The discovery of these two isotopes, suggests the existence of drip-line somewhere in the higher side. Thus, the study of these isotopes is beyond the scope of the existing mass models [207, 218]. In the present RMF/SHF calculations, the newly discovered ^{40}Mg and ^{42}Al are well within the drip-line. Also, a point of caution, it may be possible that if we allow triaxial deformation in the calculation, then we may get one minimum as a saddle point and another one as triaxial minimum. But this calculation is out of scope of our work, as we are dealing with axial deformed calculation only by using NL3 and SkI4 parameter sets, where, mostly we find similar results in both the formalisms. These type of prescriptions are used in many of the earlier publications [220].

4.2.2 Neutron configuration

Analyzing the neutron configuration for these exotic nuclei, we notice that, for lighter isotopes of Ne, Na, Mg, Al, Si, P and S the oscillator shell $N_{osc} = 3$ is empty in the $[N_{osc}, n_3, \Lambda]\Omega^\pi$. However, the $N_{osc} = 3$ shell gets occupied gradually with increase of neutron number. In case of Na, $N_{osc} = 3$ starts filling up at ^{33}Na with quadrupole moment deformation parameter $\beta_2 = 0.356$ and -0.179 with occupied orbits $[330]\frac{1}{2}^-$ and $[303]\frac{7}{2}^-$, respectively. The filling of $N_{osc} = 3$ goes on increasing for Na with neutron number and it is $[330]\frac{1}{2}^-$, $[310]\frac{1}{2}^-$, $[321]\frac{3}{2}^-$ and $[312]\frac{5}{2}^-$ at $\beta_2 = 0.472$ for ^{39}Na. Again for the oblate solution the occupation is $[301]\frac{1}{2}^-$, $[301]\frac{3}{2}^-$, $[303]\frac{5}{2}^-$ and $[303]\frac{7}{2}^-$ for $\beta_2 = -0.375$ for ^{39}Na. In case of Mg isotopes, even for ^{30,32}Mg, the $N_{osc} = 3$ shell has some occupation for the low-lying excited states near the Fermi surface. For ^{30}Mg (at β_2 = 0.599 with BE = 237.7 MeV) the N_{osc} = 3 orbit is $[330]\frac{7}{2}^-$ and for ^{32}Mg is $[330]\frac{1}{2}^-$ (BE = 248.8 MeV at $\beta_2 = 0.471$). With the increase of neutron number in Mg and Si isotopic chains, the oscillator shell with $N_{osc} = 3$ gets occupied more and more.

In Tables (4.3-4.5) the results for the ground state solutions are displayed. Thus, the prolate solutions have more binding than the oblate one for Ne, Na, Mg and S isotopes. In some cases, like $^{24-30}$Ne the prolate and oblate solutions are in degenerate states. For example, ^{24}Ne has BE = 188.9 and 189.1 MeV at $\beta_2 = 0.278$ and -0.259 respectively. Contrary to this, the ground state solutions for Al and Si are mostly oblate. For example,

^{34}Al has BE = 269.9 and 275.1 MeV at $\beta_2 = 0.159$ and -0.108 respectively. In such cases, the prolate solutions are in low-lying excited intrinsic state. Note that in many cases, there exist low lying superdeformed states.

It is important to list some of the limitations of the results due to the input parameters, mostly from E_{pair} and E_{cm} energies. As one can see from Tables (4.3-4.5), in many cases there are solutions of different shapes lying only a few MeV higher, sometimes even degenerate with the ground states. Such a few MeV difference is within the uncertainty of the predicted binding energies. A slight change in the pairing parameter, among others, may alter the prediction for the ground state shape. With few MeV uncertainty in ground state binding energies, by reassigning the ground state configurations, the deformation may change completely, and make the predictions close to each other and agree with the FRDM predictions as well.

4.2.3 Quadrupole deformation

The ground and low-lying excited state deformation systematics for some of the representative nuclei for Ne, Na, Mg, Al, Si, P and S are analyzed. In Fig. 4.1, the ground state quadrupole deformation parameter β_2 is shown as a function of mass number for Ne, Na, Mg, Al, Si, P and S. The β_2 value goes on increasing with mass number for Ne, Na and Mg isotopes near the drip-line. The calculated quadrupole deformation parameter β_2 for ^{34}Mg is 0.59 which compares well with the recent experimental measurement of Iwasaki *et al.* [205] ($\beta_2 = 0.58 \pm 0.06$). It found that this superdeformed state is 3.2 MeV above than the ground band. Again, the magnitude of β_2 for the drip nuclei reduces with neutron number N and again increases. A region of maximum deformation is found for almost all the nuclei as shown in the figure. It so happens in cases like, Ne, Na, Mg and Al that the isotopes are maximum deformed which may be comparable to superdeformed near the drip-line. For Al and Si isotopes, in general, we find oblate solutions in the ground configurations (see Table 4.4). In many of the cases, the low-lying superdeformed configuration are clearly visible and some of them can be seen in Fig. 4.1.

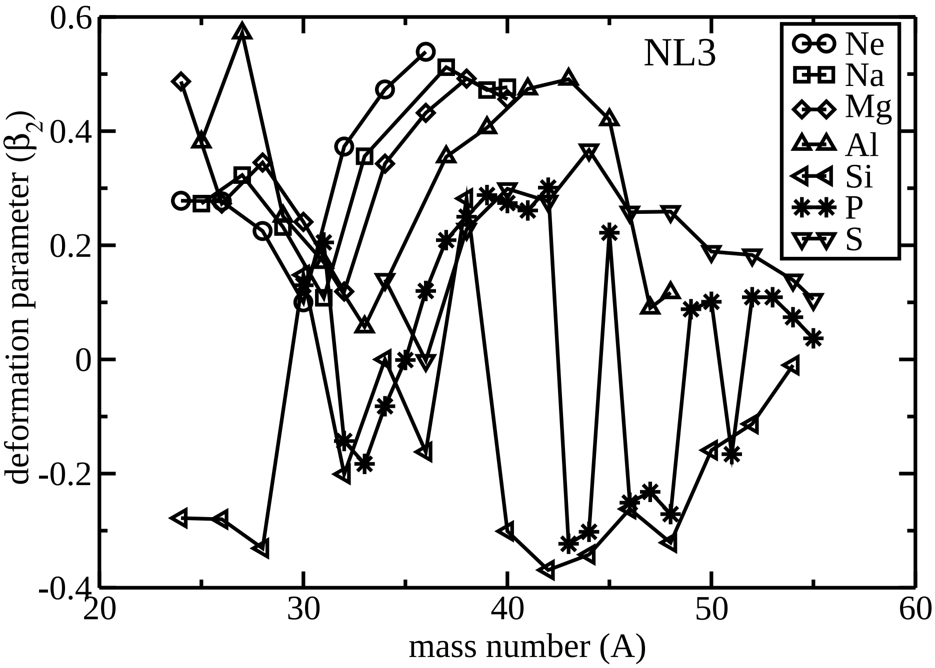

Figure 4.1: The ground state quadrupole deformation parameter β_2 versus mass number A.

4.2.4 Shape coexistence

One of the most interesting phenomena in nuclear structure physics is the shape coexistence [220–223]. In some cases of the nuclei, considered near the drip-line, the ground state configuration accompanies a low-lying excited state. In a few cases, it so happens that these two solutions are almost degenerate in energy. For example, in the RMF calculation, the ground state binding energy of ^{24}Ne is 189.1 MeV with $\beta_2 = -0.259$ and the binding energy of the excited low-lying configuration at $\beta_2 = 0.278$ is 188.9 MeV. The difference in BE of these two solutions is only 0.179 MeV. Similarly the solution of prolate-oblate binding energy difference in SkI4 is 0.186 MeV for ^{30}Mg with $\beta_2 = -0.183$ and 0.202. This type of degenerate solutions are observed in most of the isotopes near the drip-line. It is worthy to mention that in the truncation of the basis space, an uncertainty of ≤ 1 MeV in total binding energy may occur. However, this uncertainty in convergence does not affect the shape co-existence, because both the solutions are obtained by using the same model space of $N_F = N_B = 12$.

4.2.5 Two neutron separation energy (S_{2n})

The appearance of new and the disappearance of known magic number near the neutron drip-line is a well discussed topic currently in nuclear structure physics [208,224]. Some of the calculations in recent past predicted the disappearance of the known magic number N = 28 for the drip-line isotopes of Mg and S [156,225,226]. However, magic number 20 retains its magic properties even for the drip-line region. In one of our earlier publications, [105] we analyzed the spherical shell gap at N = 28 in ^{44}S and its neighboring ^{40}Mg and ^{42}Si using NL-SH [227] and TM2 parameter sets [34]. The spherical shell gap at N = 28 in ^{44}S was found to be intact for the TM2 and is broken for NL-SH parametrization. The known magic number N = 28 is noticed to be absent in ^{44}S. On the other hand, the appearance of a sudden decrease in S_{2n} energy at N = 34 in SHF result is quite prominent, which is not clearly visible in RMF prediction. This is just two units ahead than the experimental shell closure at $N = 32$ [228].

Table 4.6: Occupation of neutron orbits m^{π} in ^{47}Al and ^{46}Al driving by the deformation.

A	β_2	$n_{\frac{1}{2}^+}$	$n_{\frac{1}{2}^-}$	$n_{\frac{3}{2}^+}$	$n_{\frac{3}{2}^-}$	$n_{\frac{5}{2}^+}$	$n_{\frac{5}{2}^-}$	$n_{\frac{7}{2}^+}$	$n_{\frac{7}{2}^-}$	$n_{\frac{9}{2}^+}$
^{47}Al	0.09	8	10	4	6	2	2	0	2	0
^{47}Al	0.672	10	10	4	6	2	2	0	0	0
^{46}Al	0.109	8	9	4	6	2	2	0	2	0
^{46}Al	0.701	10	10	4	5	2	2	0	0	0

4.2.6 Superdeformation and Low Ω parity doublets

The deformation-driving $m = \frac{1}{2}^-$orbits come down in energy in superdeformed solutions from the shell above, in contrast to the normal deformed solutions. The occurrence of approximate $\frac{1}{2}^+$, $\frac{1}{2}^-$ parity doublets (degeneracy of $|m|^{\pi}$= $\frac{1}{2}^+$, $\frac{1}{2}^-$ states) for the superdeformed solutions are clearly seen in Fig. 4.2, where excited superdeformed configurations for ^{32}Mg and ^{34}Mg are given (RMF solutions). For each nucleus, we have compared the normal deformed ($\beta_2 \sim 0.1 - 0.3$) and the superdeformed configurations and analyzed the deformed orbits. The $\frac{1}{2}^+$ and $\frac{1}{2}^-$ states for the single particle levels are shown in Fig. 4.2 (for ^{32}Mg and ^{34}Mg). The occupation of neutron states (denoted by m^{π}) in ^{47}Al and ^{46}Al is given in Table 4.6. In both ^{47}Al and ^{46}Al two neutrons occupying oblate driving $f_{\frac{7}{2}}$ $m = \frac{7}{2}$ orbits in normal deformation are unoccupied in the superdeformed (SD) case. In ^{46}Al one $m = \frac{3}{2}^-$ neutron shifts to $m = \frac{1}{2}^-$, enhancing the prolate deformation.

Structure of Superdeformed Configuration:

We discus some clear and important characteristics of superdeformed solutions ($\beta \sim 0.5$ or more) obtained in mean field models as compared to the normal solutions of smaller deformation. Since the lowering and occupation of the deformation-driving $\Omega = \frac{1}{2}$ orbits from the shell above the usual valence space is so important in producing superdeformation we have emphasized their role in this discussion. There is the occurrence of $\frac{1}{2}^+$, $\frac{1}{2}^-$ orbits close together in energy (doublets) below and near the Fermi surface of the self-consistent superdeformed solutions. This feature also occurs broadly in Nilsson orbits at asymptotically large prolate deformations (see the Nilsson diagrams in Bohr and Mottelson vol. II [229]).

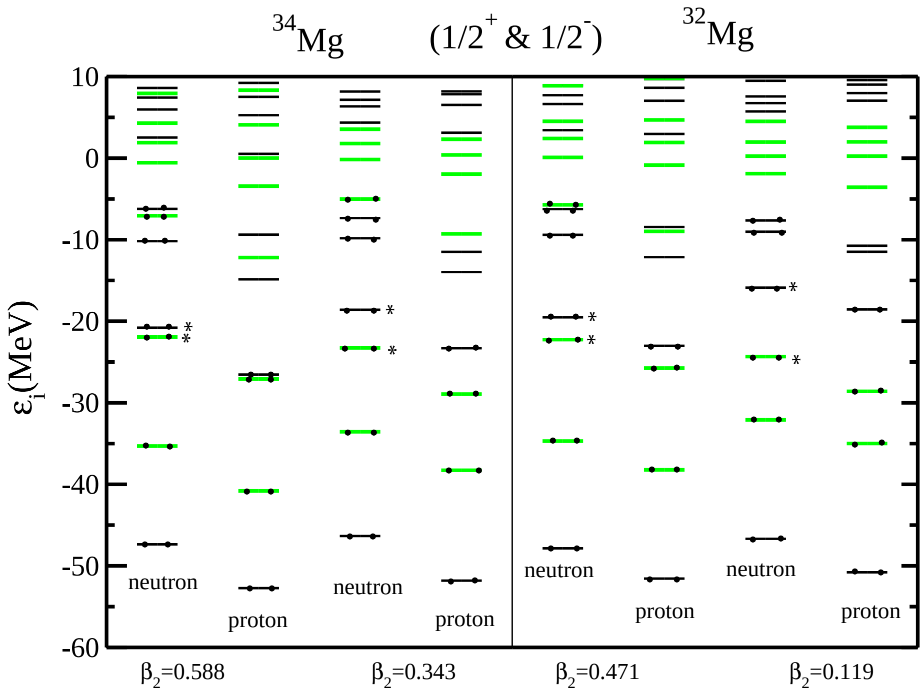

Figure 4.2: The $\frac{1}{2}^+$ and $\frac{1}{2}^-$ intrinsic single-particle states for the normal and superdeformed state for ^{32}Mg and ^{34}Mg. Doublets are noticed for the SD intrinsic states only. The $\pm\frac{1}{2}^-$ states are denoted by green lines and the $\pm\frac{1}{2}^+$ states are denoted by black.

Some features of superdeformed solutions:

In normal deformed case, the deformed orbits of a major shell form a "band"-like set of orbits, distinctly separated from the major shell above and below. Thus physical states obtained from such intrinsic states of low deformation will be well separated in energy from those intrinsic states where excitation occurs across a major shell (a single nucleon excitation across a major shell means a change in parity and significant energy change for small deformation).

The above mentioned "band"-like separation of orbits of major shells of unique parity is quite lost in the case of superdeformation. The "band"-like orbits now spread in energy (both downward and upward) and orbits of successive major shells come closer to each other in energy; an inter-mingling of orbits of different parities (see Fig. 4.2). This is a significant structural change from the case of small deformation. This has also been seen in the case of ^{84}Zr in Hartree-Fock study [230, 231].

In fact it is noticed that the $\Omega = \frac{1}{2}$ states of unique parity, seen clearly well separated in energy from the usual parity orbits in the normal deformed solutions, occurs closer to them in energy for the SD states, showing a degenerate parity doublet structure. In fact, for SD solution the $\frac{1}{2}^+$ and $\frac{1}{2}^-$ orbits are intermixed in the energy plot; while for the normal deformation they occur in distinct groups. This is true both in the Skyrme Hartree Fock and the RMF calculations.

This can be seen by examining the $\frac{1}{2}^+$ and $\frac{1}{2}^-$ orbits for small and large deformations in Fig. 4.2. This can lead to parity mixing and octupole deformed shapes for the SD structures [230]. Parity doublets and octupole deformation for superdeformed solutions have been discussed for ^{84}Zr [230, 231]. There is much interest for the experimental study of the spectra of neutron-rich nuclei in this mass region [232]. The highly deformed structures for the neutron-rich Ne-Na-Mg-Al nuclei are interesting and signature of such superdeformed configurations (with parity doublet structure) should be looked for.

4.3 Summary and Conclusions

In summary, we calculate the ground and low-lying excited state properties, like binding energy and quadrupole deformation β_2 using RMF (NL3) formalism for Ne, Na, Mg, Si, P and S isotopes, near the neutron drip-line region. In general, we find large deformed solutions for the neutron-drip nuclei which agree well with the experimental measurement. The calculation is also repeated in the frame-work of nonrelativistic Hartree-Fock formalism with Skyrme interaction SkI4. Both the relativistic and non-relativistic results are comparable to each other for the considered mass region. In the calculations a large number of low-lying intrinsic superdeformed excited states are predicted in many of the isotopes and some of them are reported.

From binding energy point of view, i.e. the sudden fall in S_{2n} value, the breaking of N = 28 magic number and the likely appearance of a new magic number at N = 34 noticed in our non-relativistic calculations, in contrast with RMF finding. This is an indication of more binding than the neighboring isotopes. However to confirm N = 34 as a magic /non-magic number more calculations are needed. In this study we find that, for the SD shape, the low Ω orbits (particularly $\Omega = \frac{1}{2}$) become more bound and nearly degenerate with the orbits of opposite parity, i.e. they show a parity doublet structure. Closely lying parity-doublet band structures and enhanced odd parity multipole transitions are possible for the superdeformed shapes.

Chapter 5

Relativistic mean field study of "Island of Inversion" in neutron rich $Z = 17 - 23, 37 - 40$ and $60 - 64$ nuclei

In this chapter, we study the extremely neutron-rich nuclei for $Z = 17 - 23$, $37 - 40$ and $60 - 64$ regions of the periodic table by using axially deformed relativistic mean field formalism with NL3* parametrization. Based on the analysis of binding energy, two neutron separation energy, quadrupole deformation and root mean square radii, we highlight the speciality of these considered regions which are the predicted *"Islands of inversion"* [217].

5.1 Introduction

The main aim of theoretical models in nuclear physics is to explain the available experimental results and predict the properties of the atomic nuclei through out the periodic table. A good description of the properties of known nuclei gives us more confidence in extrapolating to the yet unexplored areas of the nuclear chart. The systematics of two-neutron separation energy S_{2n} derived from the ground state binding energy (BE), reveal a new feature of the existence of *"Islands of inversion"* in the exotic neutron-rich regions of nuclear landscape. The Shell Model (SM) [233–235] is known to be quite successful in nuclear structure theory. Although the application of this model in various mass regions explains the data quite well, it fails to reproduce the binding energy for some of the neutron-rich

Ne, Na and Mg nuclei [233]. Almost two decades ago Patra et al. [236] performed the relativistic mean field (RMF) calculation with NL1 parameter set and could explain the reason of limitation of shell model for these nuclei. One of their explanation is the large deformation of these nuclei which is not taken into account in the SM calculations. Recently apart from supporting the presently known islands around ^{31}Na [237] and ^{62}Ti [238, 239] regions, the INM Model [240] predicts one more region around $Z = 60$. It was suggested that these nuclei of $Z = 17-23, N = 38-42, Z = 37-40, N = 70-74$ and $Z = 60-64, N = 110-116$ regions are deformed and form *islands of inversion* with more binding energy than their neighboring family of isotopes. This prediction motivates us to study the properties of such nuclei and to investigate the possible reasons of the extra stability.

5.2 Theoretical Framework

5.2.1 Choosing the Basis

We divide the calculations between three regions: first region having $Z = 17-23$, and second region $Z = 37-40$ and third region $Z = 60-64$. For choosing the proper basis, we calculate the physical observables like binding energy, root mean square (rms) radii and quadrupole deformation parameter (β_2). So, we have taken heavier nuclei from each region as a test example, for example ^{69}V from region I, ^{119}Zr from region II and ^{185}Gd from region III. We have presented our calculations in table 5.1, with N_F=N_B=6 to 16, in the interval of 2, at the initial deformation of β_2=0.2, using the NL3* parameter set. For ^{69}V; BE, rms radii and β_2 are almost same for N_F=$N_B \geq 10$. It means, we can take $N_{max} = 10$ for boson and Fermion harmonic basis for region I. In ^{119}Zr nucleus; these physical observables change from N_F=N_B= 10 to 12 but become constant after N_F=N_B= 12. Then, if we combine these two regions and take N_{max}=12, then we have sufficient space for both the regions. One can easily see that for ^{185}Gd nucleus, N_{max}=12 is not sufficient model space. It needs larger space for calculation. Therefore, in this work, we have taken N_{max}=12 for region I, II and N_{max}=14 for region III.

Table 5.1: Calculated binding energy BE (MeV), root mean square r_{ch}, r_n, r_p, r_m and quadrupole deformation parameter β_2 at different bosonic and Fermionic basis harmonic quanta. Root mean square radius are in fm. During this calculation we have taken initial deformation parameter β_0 equal to 0.2.

Nucleus	Basis	BE	r_{ch}	r_n	r_p	r_m	β_2
^{69}V	6	508.8	3.733	4.103	3.646	3.956	0.160
	8	525.8	3.822	4.236	3.738	4.077	0.220
	10	531.0	3.827	4.301	3.742	4.123	0.237
	12	531.5	3.831	4.330	3.747	4.145	0.247
	14	531.7	3.832	4.343	3.747	4.154	0.249
	16	531.8	3.831	4.355	3.747	4.162	0.251
^{119}Zr	6	817.0	4.302	4.810	4.227	4.622	0.139
	8	904.9	4.500	4.903	4.428	4.749	0.084
	10	919.5	4.518	4.986	4.447	4.811	0.055
	12	922.3	4.525	5.018	4.454	4.836	0.011
	14	922.8	4.525	5.025	4.454	4.841	0.006
	16	922.9	4.524	5.031	4.453	4.844	0.005
^{185}Gd	6	1057.4	4.783	5.507	4.716	5.247	0.139
	8	1341.9	5.155	5.520	5.092	5.376	0.106
	10	1395.8	5.280	5.661	5.219	5.512	0.118
	12	1407.0	5.294	5.721	5.233	5.557	0.122
	14	1408.4	5.289	5.737	5.228	5.566	0.114
	16	1408.2	5.289	5.741	5.228	5.569	0.114

Table 5.2: Calculated ground state binding energy BE (MeV), root mean square r_{ch}, r_n, r_p, r_m and quadrupole deformation parameter β_2 without blocking and with blocking. Root mean square radius are in fm.

Nucleus	Without Blocking						With Blocking					
	BE	r_{ch}	r_n	r_p	r_m	β_2	BE	r_{ch}	r_n	r_p	r_m	β_2
^{51}Cl	385.1	3.49	4.00	3.39	3.81	-0.25	384.5	3.49	4.00	3.39	3.81	-0.25
^{63}Cl	390.2	3.63	4.51	3.54	4.27	0.31	390.0	3.63	4.51	3.54	4.27	0.31
^{51}Ar	402.9	3.50	3.94	3.41	3.76	-0.23	402.5	3.50	3.94	3.40	3.76	-0.23
^{63}Ar	416.2	3.65	4.41	3.56	4.19	0.23	416.0	3.65	4.40	3.56	4.18	0.22
^{53}K	423.8	3.50	3.96	3.41	3.77	0.00	423.0	3.51	3.96	3.41	3.77	-0.01
^{62}K	441.4	3.65	4.30	3.56	4.09	0.12	440.8	3.65	4.30	3.56	4.09	0.12
^{55}Ca	446.5	3.56	3.98	3.47	3.80	0.00	445.9	3.56	3.98	3.47	3.80	-0.03
^{65}Ca	465.8	3.70	4.34	3.61	4.13	0.14	465.6	3.70	4.34	3.61	4.13	0.14
^{56}Sc	461.3	3.60	3.97	3.51	3.80	0.00	460.8	3.60	3.97	3.51	3.80	0.00
^{66}Sc	487.5	3.74	4.33	3.66	4.12	0.18	486.8	3.74	4.32	3.66	4.12	0.18
^{57}Ti	475.6	3.64	3.96	3.55	3.81	-0.10	475.1	3.64	3.96	3.55	3.81	-0.10
^{57}V	484.6	3.68	3.91	3.59	3.79	0.17	483.8	3.68	3.91	3.59	3.79	0.17
^{68}V	529.8	3.82	4.30	3.74	4.12	0.23	528.9	3.82	4.29	3.74	4.11	0.23
^{103}Rb	833.0	4.42	4.81	4.35	4.65	-0.27	832.4	4.41	4.81	4.34	4.65	-0.26
^{110}Rb	853.4	4.43	4.94	4.35	4.75	-0.06	852.7	4.43	4.94	4.35	4.75	-0.07
^{105}Y	863.8	4.44	4.79	4.37	4.64	-0.23	863.2	4.45	4.79	4.38	4.64	-0.24
^{107}Zr	882.9	4.47	4.81	4.40	4.66	-0.23	882.4	4.48	4.81	4.40	4.66	-0.24

5.2.2 Blocking Approximation

The physical observables like binding energy, root mean square (rms) radii and quadrupole deformation parameter (β_2) do not change much, when blocking is applied [141]. We have given our calculated results in table 5.2. The RMF values of the observables without blocking remains same as the values with blocking. If we see the table 5.2, the difference between blocking and without blocking is nearly less than 1 MeV. So, rest of the calculations are done without blocking approximation.

5.2.3 Choosing Reference Frame

While comparing our binding energy results with macro-microscopic (MM) approach, some important points need to be stated. It is a known feature in MM models that the order of accuracy varies from region to region [240] in the $N - Z$ plane. The degree of disagreement is unacceptably large even slightly away from the known domain (See Figs. 7-9, Ref. [240] and Fig. 1, Ref. [241]). On the other hand a microscopic formalism based on nuclear Lagrangian/Hamiltonian predicts physical observables through out the known/unknown territory of the periodic chart equally well. The parameters of these models have been determined by fitting the experimental data of few well known nuclei only. It is to be noted that the predictions of nuclei even in the known region are treated on an equal footing with the unknown region. Therefore, similar predictive power can be expected in the actual unknown region.

5.3 Calculations and Results

Relativistic mean field model has given very good results in β stable nuclei of the nuclear landscape. In this work we are analyzing the exotic neutron drip-line nuclei by using RMF model with recent well known NL3* [63] parameter set. We obtain matter radii, quadrupole deformation parameter and ground state binding energies of these exotic nuclei of $Z = 17 - 23, 37 - 40$ and $60 - 64$ regions. The calculated results, like binding energy, radii, quadrupole deformation are discussed in figures (5.1-5.10). In upcoming subsections we have described these results in detail.

5.3.1 Binding Energy

Binding energy (BE) is precisely measured from experiments and is responsible for stability and structure of the nuclei. The maximum binding energy corresponds to the ground state for a given nucleus and all other solutions are intrinsic excited states. The $\triangle E_1$ indicates the binding energy difference between FRDM and RMF, i.e. BE(FRDM) - BE(RMF) and $\triangle E_2$ indicates the binding energy difference between INM and RMF, i.e. BE(INM) - BE(RMF). In this subsection we are comparing RMF binding energy (BE) with INM (BE) [240] and well established FRDM (BE) [242] results.

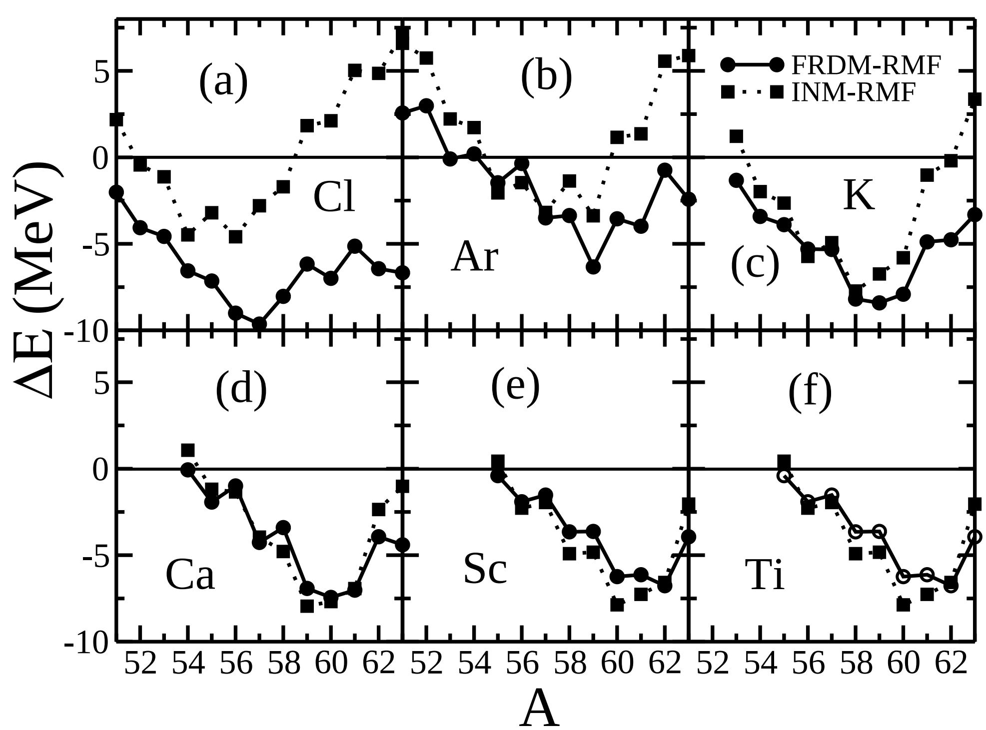

Figure 5.1: Difference between the binding energies using RMF, Finite Range Droplet Model (FRDM), Infinite Nuclear Matter (INM) model (a) The circles represent $\triangle E_1$(FRDM - RMF) (b) The squares represent $\triangle E_2$ (INM - RMF) for different mass values of $Z = 17 - 23$ region.

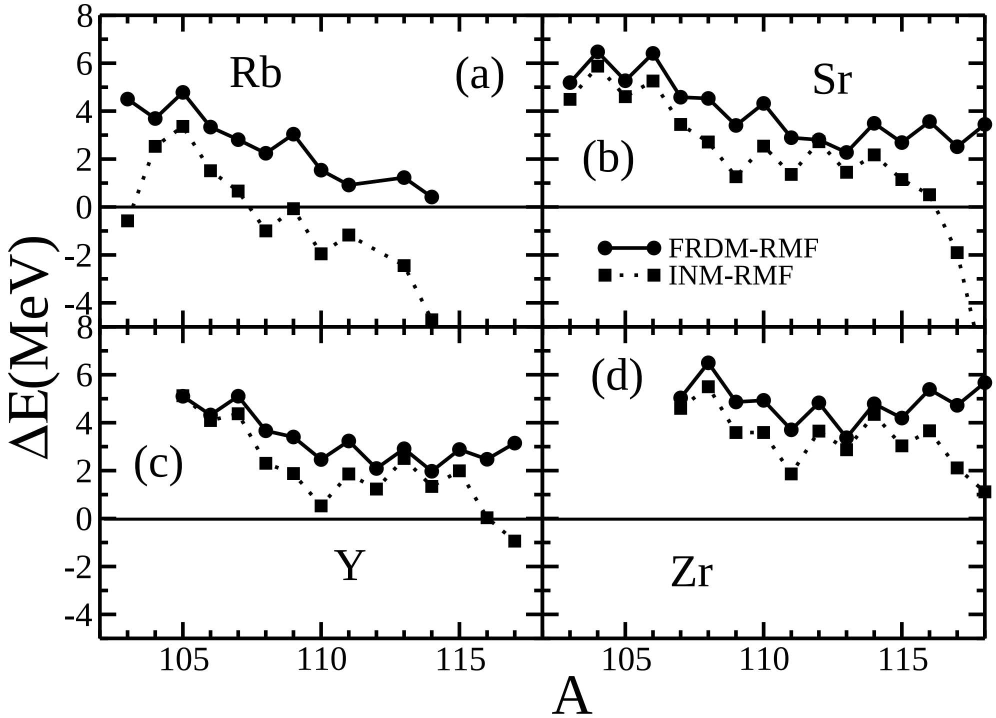

Figure 5.2: Same as Fig. 5.1 for $Z = 37 - 40$ region.

In Fig. 5.1(a), in $Z = 17 - 23$ region, we have plotted the binding energy difference $\triangle$E for Cl isotopes. $\triangle E_2$ is zero, so that RMF and INM binding energies are nearly same at lower mass region, but the difference increases in middle part and at A = 58, 59 again it goes to nearly zero, but diverges in higher mass region. If we compare our result with FRDM, then we get $\triangle E_1$ nearly zero at lower mass region, but it diverges at higher mass region. In Fig. 5.1(b), in case of Ar isotopes, the RMF BE is not consistent with INM at lower mass region but we get $\triangle E_2$ nearly zero at middle region at A = 54 - 60, which again diverges at higher mass region. If we compare our results with FRDM, then we get $\triangle E_1$ nearly zero at lower mass region at A = 51 - 56 then the difference increases at higher mass region at A = 56 - 61. In Fig 5.1(c), RMF binding energy is very close to INM in lower mass region at A = 52, 54 then $\triangle E_2$ increases within A = $55 - 60$ in the middle region. Further it is very close to INM binding energy. If we compare our results with FRDM, then $\triangle E_1$ tends to zero at A = 53 then $\triangle E_1$ increases further. In Fig 5.1(d), in case of Ca, RMF binding energy is very close to INM and FRDM binding energy at lower mass region at A = 53, 56. RMF binding energy diverges from both model (INM and FRDM) in the middle part A = 56 - 62 and then matches at higher mass region. In Fig 5.1(e), in case of Sc, we

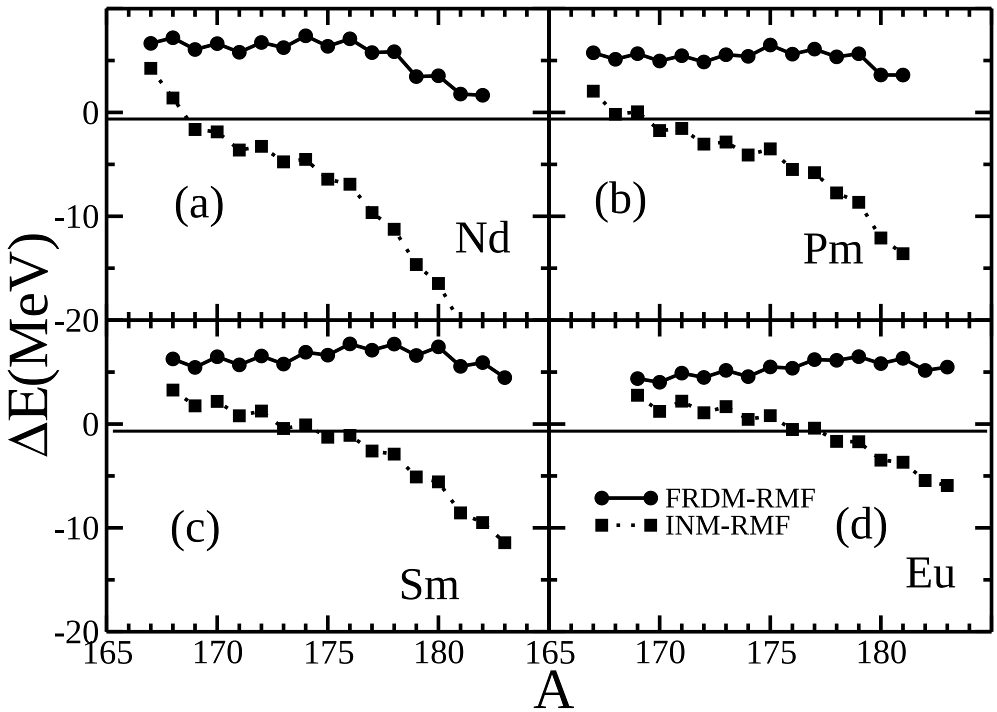

Figure 5.3: Same as Fig. 5.1 for $Z = 60 - 64$ region.

got $\triangle E_1$ and $\triangle E_2$ as zero in lower mass region , whereas both diverge in the middle part A = 53 - 63 then it further moves to zero. In the Fig 5.1(f), $\triangle E_1$ and $\triangle E_2$ are following the same trend as Fig 5.1(e) but it diverges in A = 58 - 62, and at higher region RMF BE matches with FRDM and INM predictions.

The binding energy difference for Rb isotopes is given in Fig. 5.2(a), $\triangle E_1$ has a large value at lower mass A = 103 - 107, then it tends to zero in higher region but if we compare RMF with INM results, $\triangle E_2$ increases in lower mass region and go to zero in middle region then diverges at higher mass A = 107 - 114 region. In Fig. 5.2(b), we plotted the $\triangle E_1$ and $\triangle E_2$ for Sr isotopes. We got same trend but RMF results diverges from INM at higher mass region while it closes to FRDM. In lower mass region RMF results are not matching with INM and FRDM results. Energy difference $\triangle$E for Y nuclei isotopes are given in Fig. 5.2(c), again RMF results are not consistent with INM and FRDM results at lower mass A = 105 - 108, but at higher mass region it matches with INM and FRDM results. Fig. 5.2(d), represent $\triangle E_1$ and $\triangle E_2$ for Zr isotopes, from figure it is clear that our RMF results are not matching with INM and FRDM results.

In Fig. 5.3, we have given $\triangle$E (binding energy difference) for region $Z = 60 - 64$

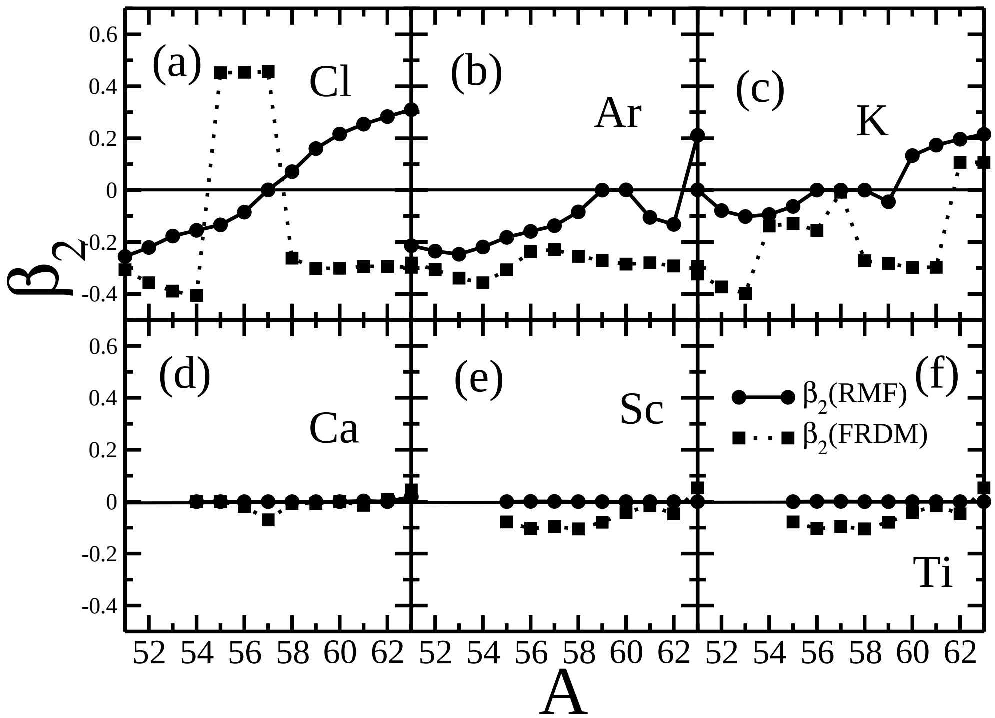

Figure 5.4: Quadrupole Deformation Parameter obtained from RMF(NL3*) (circle) compared with the FRDM(square) results for different isotopes of Z = 17 - 23 region.

nuclei. For Nd isotopes, RMF binding energy is not consistent with FRDM at $A = 166 - 180$. Later on RMF binding energy is close to FRDM result for few isotopes $A = 179 - 181$ then again diverges at $A = 182$. When we compare our result with INM binding energy, the binding energy of RMF is very close to it at $A = 168 - 170$ and later on diverges with increase in mass number. In case of Pm nuclei isotopes, which is plotted in Fig. 5.3(b), RMF result is not consistent with FRDM for the whole region. If we compare our result with INM region, it is consistent till $A = 168 - 172$ and then diverges. In Sm isotopes, RMF binding energy is not consistent with FRDM in whole region. $\triangle E$ for Sm has followed the same trend as $\triangle E$ of Pm nuclei isotopes i.e. matches at lower mass region and diverge at higher mass region for both FRDM and INM results. In Eu nuclei isotopes, RMF BE is not consistent with FRDM and INM binding energy, and in both cases △E increases with mass numbers.

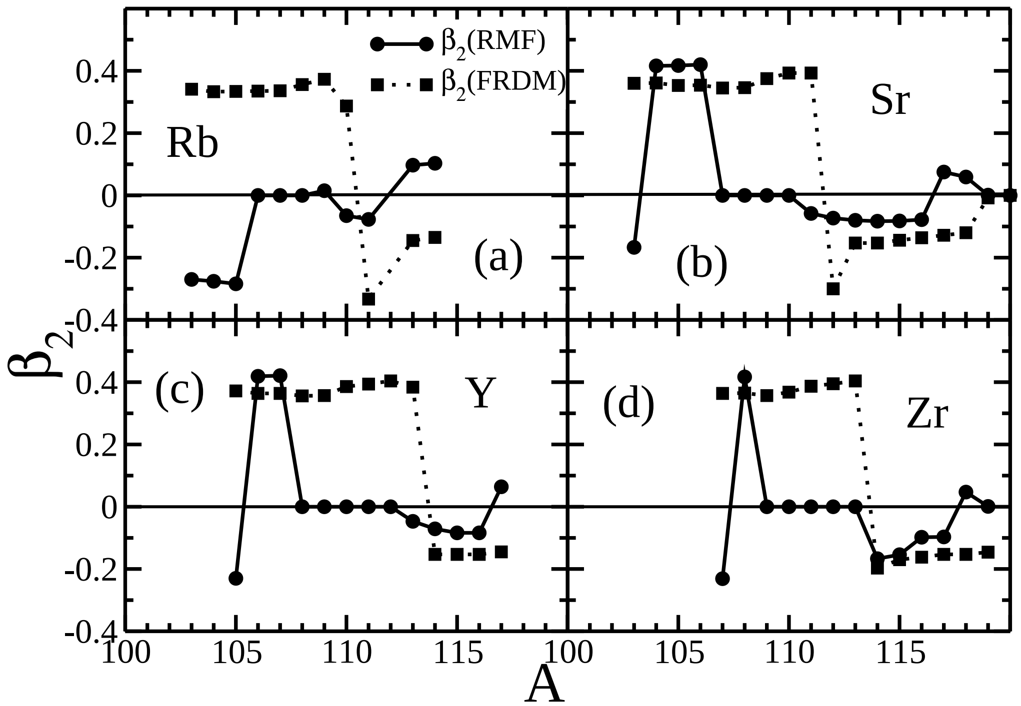

Figure 5.5: Same as Fig. 5.4 for Z = 37 - 40 region.

5.3.2 Quadrupole Deformation

Quadrupole deformation parameter (QDP) β_2 is directly connected to the shape of the nucleus. It is very common to say that if we go towards drip-line nuclei, deformation will gradually increase but recently experimental work of Tshoo [243] explains that ^{22}O is prolate in shape but ^{24}O is spherical in structure. Keeping this result in our mind we have calculated the QDP β_2 for recently predicted *island of inversion* region in nuclear landscape. Because of the unavailability of experimental data of these nuclei, we have compared our calculated QDP β_2 with well established FRDM [207] data. In Fig. 5.4, we have plotted the quadrupole deformation parameter β_2 for RMF and FRDM models as a function of mass number for Z = 17 - 23 region. In Cl case, QDP β_2 continuously increases with the mass number, as shown in Fig. 5.4(a). In lower mass region Cl isotopes are oblate and in higher mass region these are prolate and middle case A = 56 - 58, there is continuous shape change from oblate to prolate. If we compare RMF results with FRDM predictions then we get totally different result in FRDM. In FRDM, shape is suddenly changed from oblate to prolate (A = 54) and prolate to oblate (A = 57). Most of the Cl isotopes are oblate in FRDM model. There are continuous changes in deformation but there is very small

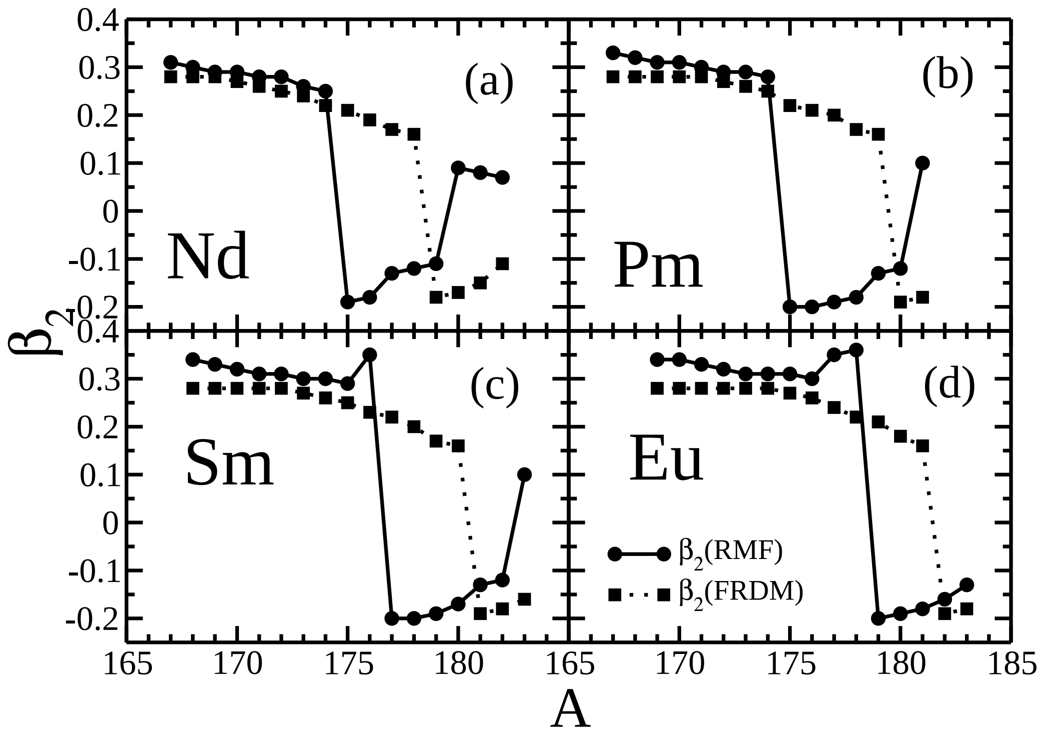

Figure 5.6: Same as Fig. 5.4 for Z = 60 - 64 region.

amount of energy difference (1 MeV) between ground state and first excited state. So we can say that other shape is also possible, But here we are taking only the ground state and neglecting the other possibility of shapes. In Ar case, most of the isotopes are oblate in lower mass region A = 52 - 57, and some are spherical at A = 59 - 60 then in higher region it again changes its shape from oblate to prolate in RMF model. When we compare with FRDM data, RMF is very close to FRDM except middle and high region in Fig. 5.4(b). FRDM is completely oblate in shape over the region. In Fig. 5.4(c), we have plotted the QDP β_2 for K isotopes. From figure it is very clear that most of the isotopes are spherical in shape. When we compare with FRDM data, it shows the same trend as RMF at A = 54 - 57 i.e. spherical in shape. In Ca, Sc, Ti case all are spherical in shape over all isotopes.

Deformation parameter for Rb isotopes are given in Fig. 5.5(a). From the figure, it is clear that most of the isotopes are spherical in shape but in lower mass region A = 103 - 105, it is oblate. If we see the QDP β_2 for Rb isotopes in FRDM model, we found that most are in prolate shape in lower mass region A = 103 - 110 then shape changes to oblate which is totally different from RMF result. Sr isotopes are given in Fig. 5.5(b), for Sr isotopes, most of the nuclei are in spherical but in lower mass A = 104 - 106 are prolate and at A

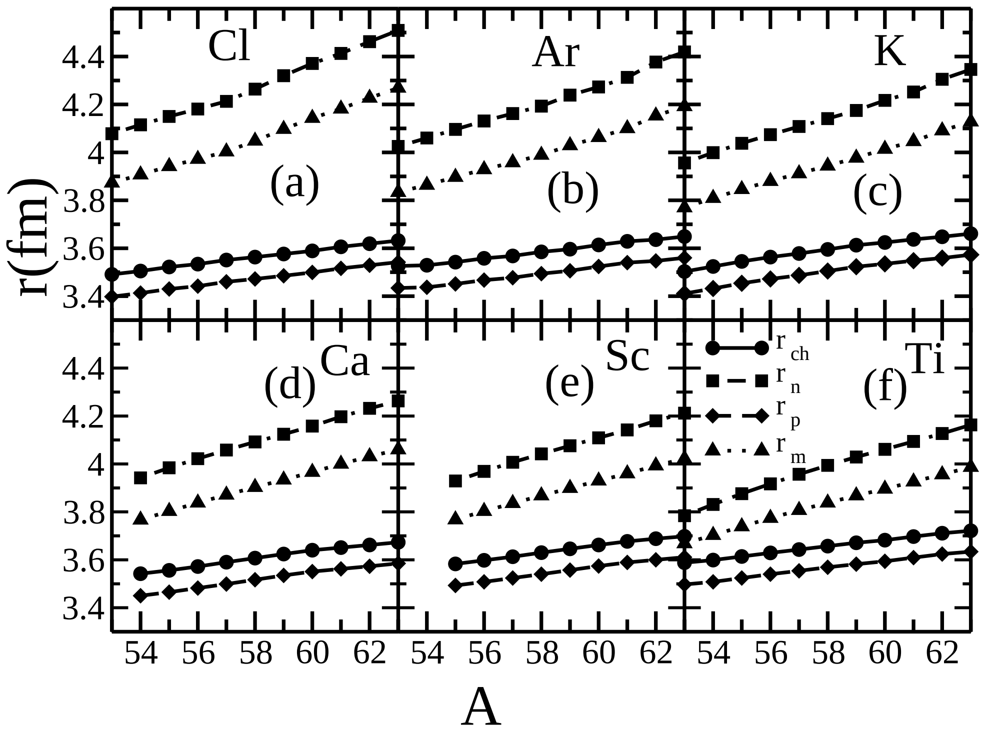

Figure 5.7: The charge radii r_{ch} (circle), The neutron radius r_n (square), The proton radius r_p (diamond), the rms radii r_m of matter distribution (triangle up) for different isotopes of Z = 17 - 23 region using the RMF(NL3*) formalism.

= 103 shape changes from prolate to oblate. If we see the result of FRDM, most of the Sr isotopes are prolate and in higher region it is spherical. RMF matches to FRDM at A = 104 - 106 and in higher region. Again we are getting spherical shape for A = 108 - 117 for Y isotopes in Fig. 5.5(c). RMF matches only at A = 106, 107 and in higher mass A = 114 - 116. In Zr isotopes, It is spherical in shape at A = 109 - 120 except A = 114, 115 as shown in the Fig. 5.5(d). If we go from A = 107 to 109, then we got a sharp shape change at A = 108 i.e. oblate to prolate and again prolate to spherical. FRDM have prolate shape in lower mass region A = 107 - 113 and then changes to oblate in A = 114 - 120.

In Fig. 5.6(a), for Nd isotopes, at A = 167 -174, both RMF and FRDM are prolate in shape but when we go further RMF changes its shape to oblate in A = 175 - 179 region while FRDM remains prolate in shape. In higher mass region A = 180 - 182 RMF goes oblate to nearly spherical and FRDM goes from prolate to oblate it means these two model are not consistent in A = 175 - 182. Isotopes of Pm are given in Fig. 5.6(b), here we get consistent result in RMF and FRDM model at A = 167 - 175. Then RMF changes to oblate

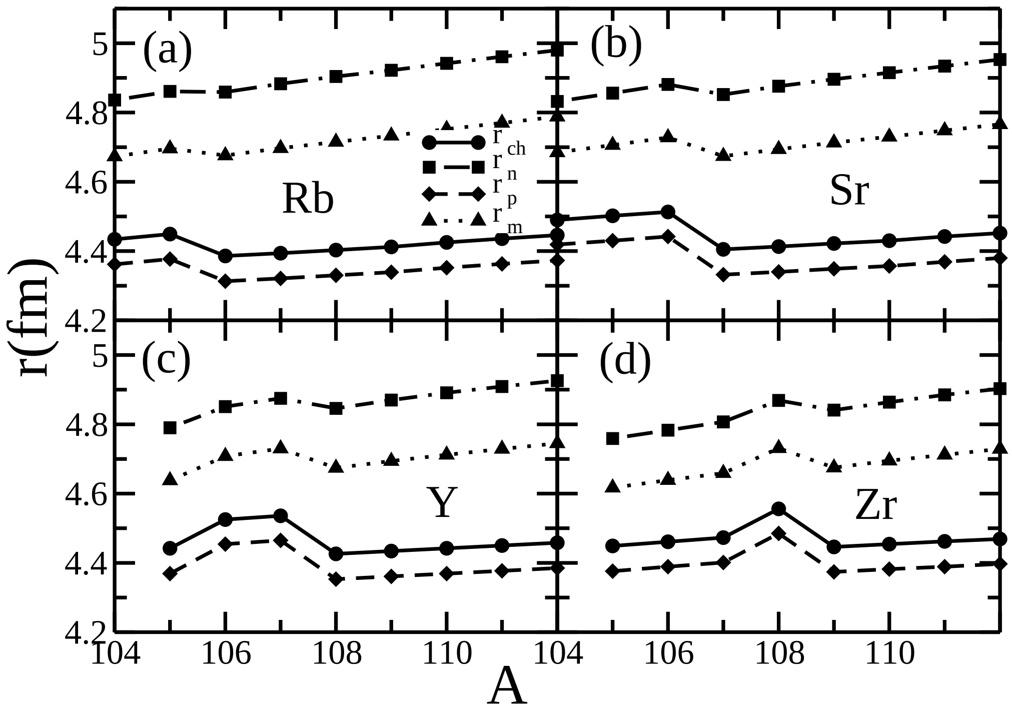

Figure 5.8: Same as Fig. 5.7 for Z = 37 - 40 region .

in higher mass region and goes to nearly spherical while FRDM does not change upto A = 179 then sharp decrease to oblate. In Sm case, both models match to each other in A = 168 - 176 then RMF goes to oblate and spherical shape where FRDM does not follow the RMF trend except A = 181, 182. In Eu isotopes as shown in Fig. 5.6(d), both RMF and FRDM show consistency at A = 169 - 178, later on RMF changes to oblate at A = 179 - 182. FRDM is matching with RMF at A = 181, 182 only at higher mass region.

5.3.3 Nuclear Radius

In this subsection we are concentrating on the neutron radius (r_n), proton radius (r_p), charge radius (r_{ch}) and matter radius (r_m) which are calculated by using RMF(NL3*) formalism. In Fig. 5.7, we have plotted the r_n, r_p, r_{ch}, and r_m for Cl, Ar, K, Ca, Sc, Ti and V nuclei. In $Z = 17 - 23$ region, all the radii increase monotonically with mass number. In Fig. 5.8, we have plotted the r_n, r_p, r_{ch}, r_m with mass number for $Z = 37 - 40$ region. In Rb isotopes, there is a sharp fall in radii till $A = 106$, then radii increase monotonically. In Sr isotopes, the radii follow same trend as Rb isotopes but in this case fall at $A = 107$, then the radii increase monotonically. In Y isotopes, the radii follow a jump at $A = 106$ and remain

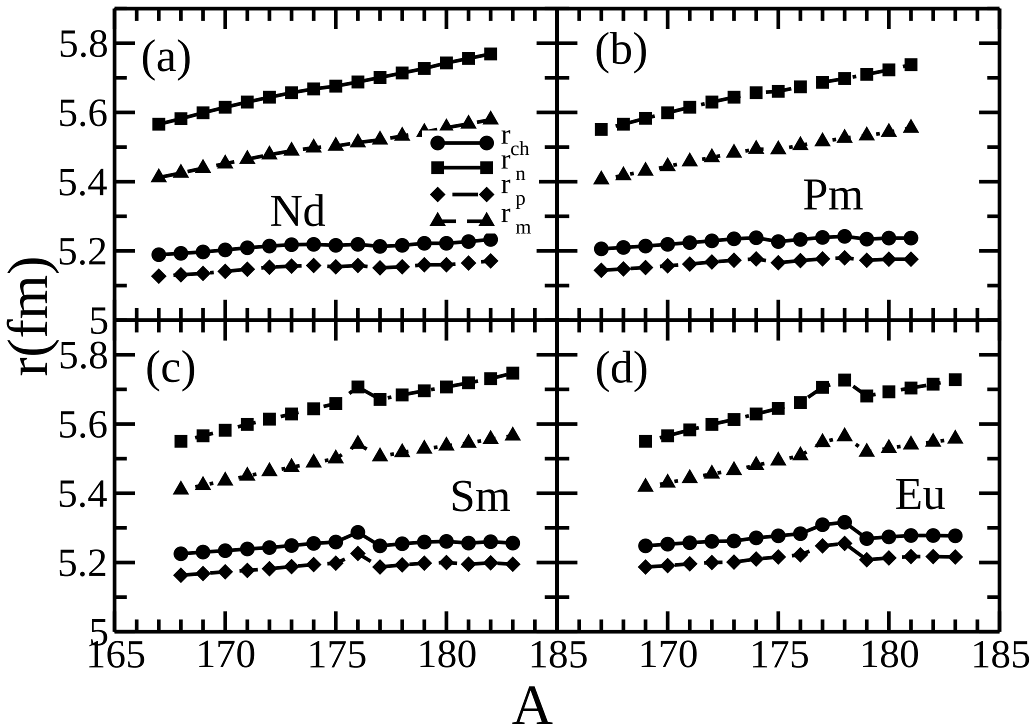

Figure 5.9: Same as Fig. 5.7 for Z = 60 - 64 region .

constant upto $A = 107$, then decrease at $A = 108$. Later on the radii follow the same trend means the radii increase monotonically with mass number. In Zr isotopes, the radii increase and it follows a jerk at $A = 108$ then go down at $A = 109$ and later on increase. In Fig. 5.9, we have plotted the radius curve for $Z = 60 - 64$ region, in the case of Nd, Pm isotopes the radii increase monotonically with atomic mass number. In Sm (Fig. 5.9c) isotopes, we get a small jerk in $A = 176$ while in Eu (Fig. 5.9d) isotopes this jerk arises at $A = 177 - 178$, then increases monotonically indicating a change in the deformation of the nuclei.

5.3.4 Two-neutron separation energy

The two-neutron separation energy S_{2n}(N,Z) = BE(N, Z) - BE(N-2, Z) is shown in Fig. 5.10. The S_{2n} values decrease gradually with increase in neutron number. It is indeed satisfying to note that in the recent years strong evidences both experimental and theoretical have emerged [238, 239] supporting the existence of this island of inversion centering around ^{62}Ti. We can predict the stability of these nuclei by S_{2n} energy. If S_{2n} is large, it means nuclei will be stable with two-neutron separation. As shown in first part (a) of Fig. 5.10, in

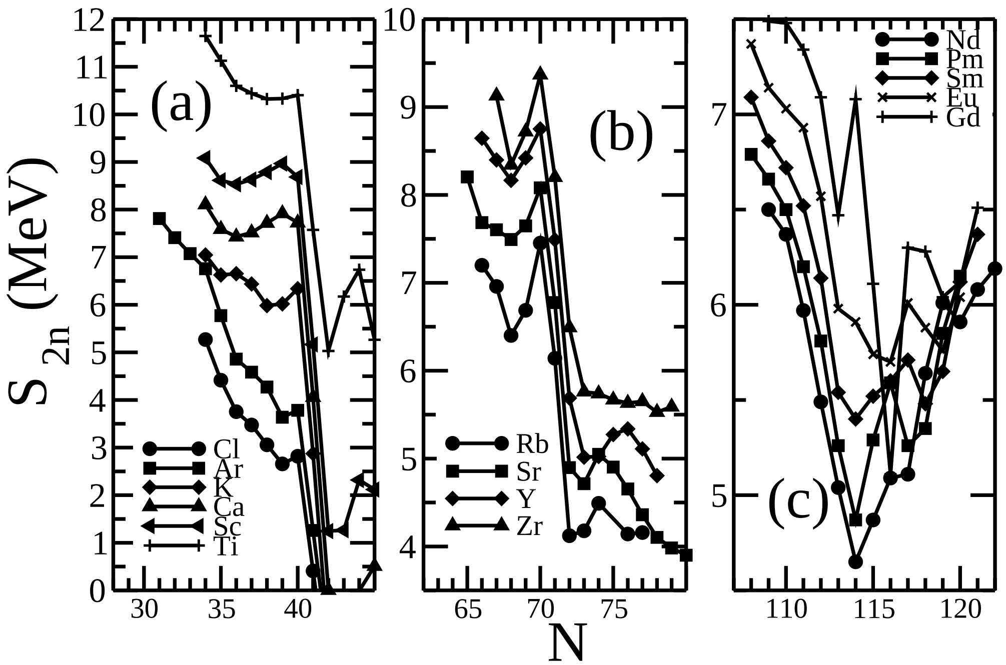

Figure 5.10: The two-neutron separation energy S_{2n} for different isotopes of $Z = 17 - 23, 37 - 40, 60 - 64$ region by using RMF(NL3*) formalism.

$Z = 17 - 23$ region, we are getting a sharp down curve for all the members of this region at N = 42. So we can say that this may be the neutron magic number in this neutron-dripline nuclei. In S_{2n} plot for Ti, we are getting a small considerable jerk at N = 44. This shows the extra stability of nuclei. In Sc, S_{2n} plot follow the same trend as in Ti, but the magnitude is very small. In other cases, i.e. $Z = 17, 18, 19, 20$ region, there is no any local extra stability. In second part (b), we are getting a sharp down curve at $N = 68$ for all the members of this region. In Sr, Rb, there is a small jerk at $N = 74$. In other cases, there is no local stability. In third part (c), for $Z = 60 - 64$ region, there is a sharp fall at $N = 112$ for all the members of this region. We get local extra stability in Nd, Pm and other nuclei also follow nearly the same trend.

5.4 Discussion and Remarks

Taking RMF as a reference, we evaluate $\triangle E_1$ and $\triangle E_2$. Analyzing Fig. 5.1, we find both $\triangle E_1$ and $\triangle E_2$ similar for all the considered six nuclei, Cl to Ti. The large value of $\triangle E_1$ and $\triangle E_2$ at middle of the region shows the speciality of these nuclei, except Cl isotopes

[Fig. 5.1(a)]. All other isotopes show similar trend with INM and FRDM. From Fig. 5.2 and Fig. 5.3, $\triangle E_1$ are almost constant, if one extends the calculation to higher mass number in isotopic chain. On the other hand, calculated $\triangle E_2$ goes on increasing with A. In this situation, the predictive power of RMF, FRDM and INM are questionable. For example, (1) if we consider RMF as absolute reference, then the large discrepancy of $\triangle E_2$ with mass number indicates the limitation of INM model near the drip-line region, or vice versa. (2) similarly if we analyze $\triangle E_1$, it is somewhat constant with RMF for the entire region. As we have discussed, the RMF is based on microscopic origin in mesons and nucleons level. Except few fitted nuclei, all others masses, radii and quadrupole deformation are the predicted results in a large region of the periodic chart. The RMF results are found to be good for almost all the known cases. This prediction not only confines to masses, radii, β_2 but also comes well for other observables. Thus, if we believe all these predictions as success, then the mass formula specially INM needs some modification, specially in the region of $Z = 37 - 40$ and $Z = 60 - 64$ which are considered in this chapter.

Chapter 6

The effect of isoscalar-isovector coupling in infinite nuclear matter

In the framework of relativistic mean field theory, we study the effect of non-linear cross coupling between the isoscalar-vector and isovector-vector mesons on top of the G2 parametrization. The energy density and pressure are calculated over a wide range of baryon density. The observables like symmetry energy and related coefficients are also evaluated systematically. The effect of the cross coupling on the symmetry energy of symmetric nuclear matter are studied. The work is further extended to $\beta-$equilibrium matter to estimate the mass and radius of neutron star and also to baryon octet to see the effect of the coupling over the equation of state.

6.1 Introduction

The best possible and well defined theoretical laboratory to study many body system is infinite nuclear matter at certain conditions. One can review the status of microscopic studies of nuclear matter and neutron rich matter, which is already reached to its destination by mean-field models (relativistic and non-relativistic) [62, 244–248] along with some other-microscopic studies such as Brueckner-Hartree-Fock (BHF) [249–252] and Dirac-Brueckner-Hartree-Fock (DBHF) [116, 186, 253–255]. The isospin and density dependence of the symmetry energy E_{sym} is one of the current interest for its implications in nuclear and astrophysics. The softening in equation of state (EOS) of nuclear matter likely leads to an exciting problem in astro-nuclear physics from last few decades. Meanwhile the phenomena like formation of superheavy nuclei in the astrophysical system and the location of neutron drip-line are some of the exciting studies which directly link with the symmetry energy [88]. A parameter set having large value of compressional modulus K_0 shows appropriately stiff symmetry energy i.e. rises rapidly with baryon density [256, 257]. This makes a passing reference between K_0 and E_{sym}, which is a function of density and isospin component of scalar and vector mesons. Thus, it is needed to explore the effects of E_{sym} in the RMF model, which was limited to a narrow range from the analysis of skin data, on the composition and structure of hot proton-neutron and cold neutron star matter that hold a large density range [36, 258–261].

In this work, we introduce an additional term on top of the $G1$ or $G2$ parameter sets to the Lagrangian, which comes from the cross-interaction between isoscalar and isovector fields with coupling constant Λ_v [91]. Although the inclusion of this term is not new, but it is not taken into account in the effective field theory motivated relativistic mean field (E-RMF) model [139]. This additional term on G2 affects the EOS, E_{sym}, slope- L_{sym}, curvature- K_{sym} and skewness- Q_{sym} parameters, considerably. Further, it may be expected that the full parameter set of the E-RMF formalism (E-RMF+Λ_v) overcomes the deficiency arises by other parametrizations [64, 96]. The stiffness of E_{sym} with respect to baryon density follows a softer path with this extra coupling. Without this additional coupling it may not be possible to overcome the hindrance of constraint between symmetry energy and slope parameter L_{sym} with G2 set only. The additional coupling does not affect other nuclear properties like energy and pressure of the symmetric nuclear matter as well as finite nuclei, which is an important prospectus of this coupling.

6.2 Formalism

Because of the uniformity of the nuclear system for infinite nuclear matter, all of the gradients of the fields in Eqs. (2.17)–(2.21) vanish and only the κ_3, κ_4, η_1, η_2 and ζ_0 non-linear couplings remain. Due to the fact that the solution of symmetric nuclear matter in mean field depends on the ratios g_s^2/m_s^2 and g_v^2/m_v^2 [26], we have seven unknown parameters. By imposing the values of the saturation density, total energy, incompressibility modulus and effective mass, we still have three free parameters (the value of g_ρ^2/m_ρ^2 is fixed from the bulk symmetry energy coefficient). The energy density and pressure of nuclear matter is given by

$$
\begin{aligned}
\mathcal{E} \;=\;& \frac{2}{(2\pi)^3}\int d^3k E_i(k) + \rho W + \frac{m_s^2\Phi^2}{g_s^2}\left(\frac{1}{2} + \frac{\kappa_3}{3!}\frac{\Phi}{M} + \frac{\kappa_4}{4!}\frac{\Phi^2}{M^2}\right) \\
& - \frac{1}{2}m_v^2\frac{W^2}{g_v^2}\left(1 + \eta_1\frac{\Phi}{M} + \frac{\eta_2}{2}\frac{\Phi^2}{M^2}\right) - \frac{1}{4!}\frac{\zeta_0 W^4}{g_v^2} + \frac{1}{2}\rho_3 R \\
& - \frac{1}{2}\left(1 + \frac{\eta_\rho\Phi}{M}\right)\frac{m_\rho^2}{g_\rho^2}R^2 - \Lambda_v R^2 \times W^2 + \frac{1}{2}\frac{m_\delta^2}{g_\delta^2}\left(D^2\right) \,, \qquad (6.1)
\end{aligned}
$$

$$
\begin{aligned}
\mathcal{P} \;=\;& \frac{2}{3(2\pi)^3}\int d^3k \frac{k^2}{E_i(k)} - \frac{m_s^2\Phi^2}{g_s^2}\left(\frac{1}{2} + \frac{\kappa_3}{3!}\frac{\Phi}{M} + \frac{\kappa_4}{4!}\frac{\Phi^2}{M^2}\right) \\
& + \frac{1}{2}m_v^2\frac{W^2}{g_v^2}\left(1 + \eta_1\frac{\Phi}{M} + \frac{\eta_2}{2}\frac{\Phi^2}{M^2}\right) + \frac{1}{4!}\frac{\zeta_0 W^4}{g_v^2} \\
& + \frac{1}{2}\left(1 + \frac{\eta_\rho\Phi}{M}\right)\frac{m_\rho^2}{g_\rho^2}R^2 + \Lambda_v R^2 \times W^2 - \frac{1}{2}\frac{m_\delta^2}{g_\delta^2}\left(D^2\right) \,, \qquad (6.2)
\end{aligned}
$$

where $E_i(k)$=$\sqrt{k^2 + M_i^{*2}}$ $(i = p, n)$. In the context of density functional theory, it is possible to parametrize the exchange and correlation effects through local potentials (Kohn-Sham potentials), as long as those contributions be small enough [262]. The Hartree values are the ones that control the dynamics in the relativistic Dirac-Brückner-Hartree-Fock (DBHF) calculations. Therefore, the local meson fields in the RMF formalism can be interpreted as Kohn-Sham potentials and in this sense equations (2.16)-(2.21) include effects beyond the Hartree approach through the non-linear couplings [139–143].

The bulk properties like binding energy and charge radius do not isolate the contribution from the isoscalar or isovector channels. These are estimated by an overall fitting of the parameters, precisely with the help of the $\rho-$meson coupling. That is the reason, the modern relativistic Lagrangian ignores the contribution of $\delta-$ and $\rho-$ meson separately, i.e. once $\rho-$meson is included, it takes care of the bulk properties of the nucleus (isovector part) and does not need of $\delta-$meson [41–44]. However, the importance of the $\delta-$meson is realized, when we study the properties of highly asymmetry system, such as drip-line nuclei and neutron star [45–57]. In particular, at high density, neutron star and heavy ion collisions, the proton fraction of $\beta-$stable matter may increase and the splitting of the effective mass should affect the transfer properties. Hence, the isovector-scalar meson are taken into account, while its individual contribution is little in the NN-interaction due to its heavy mass (∼980 MeV, more than nucleon mass). But for highly asymmetry system, the total contribution of the $\delta-$meson can not be ignored.

6.2.1 Symmetry Energy

The symmetry energy E_{sym} is important in infinite nuclear matter and finite nuclei, because of isospin dependence in the interaction. The isospin asymmetry arises due to the difference in number densities and masses of the neutron and proton, respectively. The expression of symmetry energy E_{sym} is a combined expression of $\rho-$ and $\delta-$mesons, which is defined as [45, 89, 141, 263]:

$$E_{sym}(\rho) = E_{sym}^{kin}(\rho) + E_{sym}^{\rho}(\rho) + E_{sym}^{\delta}(\rho), \tag{6.3}$$

with

$$E_{sym}^{kin}(\rho) = \frac{k_F^2}{6E_F};\ E_{sym}^{\rho}(\rho) = \frac{g_\rho^2 \rho}{8m_\rho^{*2}} \tag{6.4}$$

and

$$E_{sym}^{\delta}(\rho) = -\frac{1}{2}\rho \frac{g_\delta^2}{m_\delta^2}\left(\frac{M^*}{E_F}\right)^2 u_\delta\left(\rho, M^*\right). \tag{6.5}$$

The last function u_δ is from the discretness of the Fermi momentum. This momentum is quite large in nuclear matter and can be treated as a continuum and continuous system. The function u_δ is defined as:

$$u_\delta\left(\rho, M^*\right) = \frac{1}{1 + 3\frac{g_\delta^2}{m_\delta^2}\left(\frac{\rho_s}{M^*} - \frac{\rho}{E_F}\right)}. \tag{6.6}$$

In the limit of continuum, the function $u_\delta \approx 1$. The whole symmetry energy ($E_{sym}^{kin} + E_{sym}^{pot}$) arises from $\rho-$ and $\delta-$mesons, given as:

$$E_{sym}(\rho) = \frac{k_F^2}{6E_F} + \frac{g_\rho^2 \rho}{8m_\rho^{*2}} - \frac{1}{2}\rho \frac{g_\delta^2}{m_\delta^2}\left(\frac{M^*}{E_F}\right)^2 u_\delta\left(\rho, M^*\right), \tag{6.7}$$

where the effective energy $E_F = \sqrt{(k_F^2 + M^{*2})}$, k_F is the Fermi momentum. The effective mass of the ρ-meson modified, because of cross coupling of $\rho - \omega$ is given by

$$m_\rho^{*2} = \left(1 + \eta_\rho \frac{\Phi}{M}\right) m_\rho^2 + 2g_\rho^2(\Lambda_v W^2). \tag{6.8}$$

The cross coupling of isoscalar-isovector mesons (Λ_v) modified the density dependent of E_{sym} without affecting the saturation properties of the symmetric nuclear matter (SNM). In E-RMF model with pure G2 set, the symmetric nuclear matter saturates at $\rho_0 = 0.153 fm^{-3}$, BE/A = 16.07 MeV, compressibility K_0 = 215 MeV and symmetry energy of E_{sym}= 36.42 MeV [142, 143].

In the numerical calculation, the coefficient of symmetry energy E_{sym} is obtained by the energy difference between symmetric and pure neutron matter at saturation and it is defined by Eqn. (6.7) for a quantitative description at various densities. The symmetry energy of a nuclear system is a function of baryonic density ρ, hence can be expanded in a Taylor series around the saturation density ρ_0 as (6.7):

$$E_{sym}(\rho) = E_0 + L_{sym}\mathcal{Y} + \frac{1}{2}K_{sym}\mathcal{Y}^2 + O[\mathcal{Y}^3], \tag{6.9}$$

where $E_0 = E_{sym}(\rho = \rho_0)$, $\mathcal{Y} = \frac{\rho-\rho_0}{3\rho_0}$ and the coefficients L_{sym} and K_{sym} are defined as:

$$L_{sym} = 3\rho \left(\frac{\partial E_{sym}}{\partial \rho}\right)_{\rho=\rho_0}, \; K_{sym} = 9\rho^2 \left(\frac{\partial^2 E_{sym}}{\partial \rho^2}\right)_{\rho=\rho_0}.$$

Here L_{sym} is the slope parameter defined as the slope of E_{sym} at saturation. The quantity K_{sym} represents the curvature of E_{sym} with respect to density. A large number of investigation have been made to fix the value of E_{sym}, L_{sym} and K_{sym} [117, 264–269].

6.3 Calculations and Discussions

The mean field equations for the mesons and fermions are solved self-consistently. Using these fields, we estimate $\mathcal{E}$ and $\mathcal{P}$ as a function of baryon density. The G2 parameter set [139] along with the additional Λ_v coupling in the E-RMF (G2+Λ_v) formalism are used in the calculations. In G2 set, ζ_0 is the self-coupling constant of ω-meson [34, 35, 37] which is responsible for the major softening of the EOS at high density and reproduced the maximum mass of neutron star. For softening the symmetry energy of the system at nuclear matter density, we have added an extra coupling on G2 set between isoscalar and isovector fields with coupling constant Λ_v. This makes possible to soften the E_{sym} and reproduce saturation properties without affecting other physical observables.

Infinite nuclear matter is important for the investigation of physical quantities relevant to heavy nuclei and compact objects like neutron star. At saturation density ρ_0, the binding

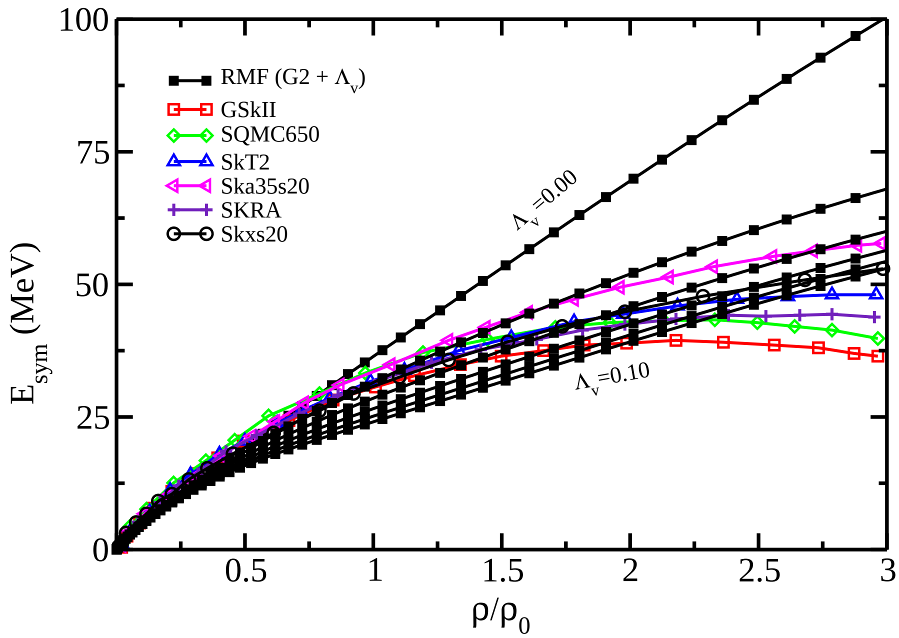

Figure 6.1: The results of symmetry energy E_{sym} is a function of ρ/ρ_0 from RMF for different values of Λ_v compare with others non-relativistic SHF predictions of parameters GSkII [270], SQMC650 [271], SKT2 [272], Ska35s20 [273], SKRA [274], Skxs20 [275].

energy per particle as a function of density is an established quantity from the empirical and experimental observation. The cross coupling $\omega - \rho$ does not effect the energy per particle and pressure density of symmetric nuclear matter. It is easily reflect from the $\mathcal{E}$ and $\mathcal{P}$ equations 6.1 and 6.2. The obtained results for $\mathcal{E}$/A and $\mathcal{P}$ are exactly similar as that of Ref. [36] irrespective of the Λ_v values. Being insensitive to Λ_v, the aim of this work is to pursue the systematic variation of E_{sym} by employing the $\omega - \rho$ coupling parameter Λ_v, which is discussed below.

Figure 6.1, shows the variation of symmetry energy E_{sym} with nuclear matter density for different values of Λ_v. From the figure, it is clear that at $\Lambda_v = 0.0$, the symmetry energy curve increases linearly. However, this linearity deviates with increasing value of Λ_v. For smaller Λ_v, the E_{sym} curve is more stiffer and becomes softer with Λ_v. The variation of E_{sym} can be quantitatively seen from Table 6.1, which display the maximum $E_{sym} = 36.42$ MeV at $\Lambda_v = 0.0$ and $E_{sym} = 21.06$ MeV (minimum) at $\Lambda_v = 0.21$. It is clear that, after certain value of Λ_v, the changes of E_{sym} is minimal. To compare our results of E_{sym} with other calculations, we display the symmetry energy obtained by

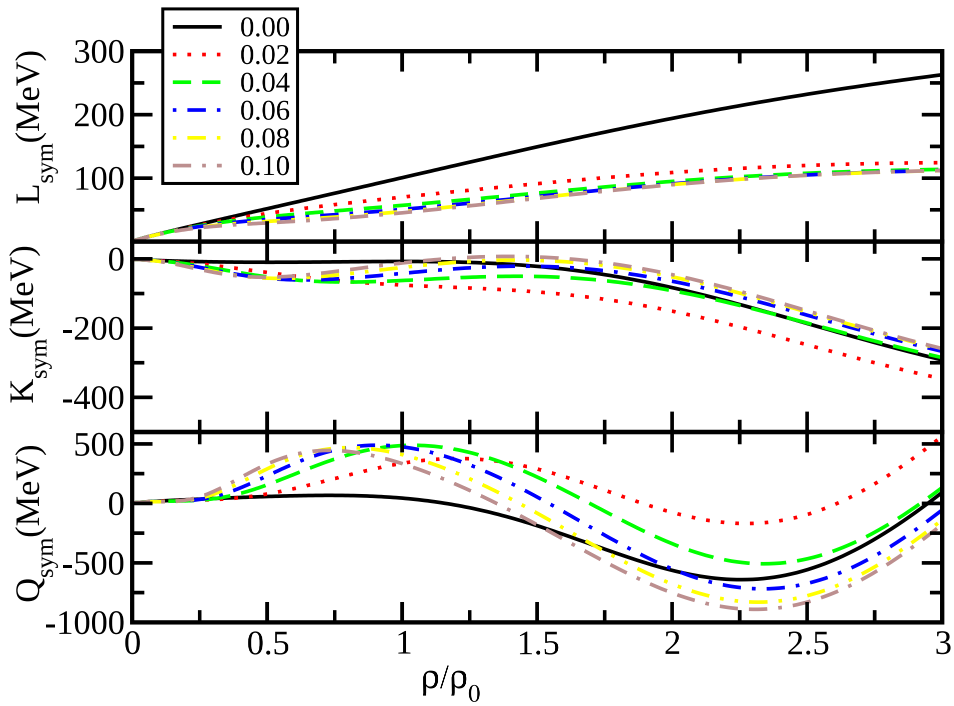

Figure 6.2: The slope L_{sym}, curvature K_{sym} and skewness Q_{sym} parameters of symmetry energy have been plotted with ρ/ρ_0 for different value of Λ_v (with $G2$ parameter set).

various non-relativistic Skyrme Hartree-Fock (SHF) parametrizations, like GSkII [270], SQMC650 [271], SKT2 [272], Ska35s20 [273], SKRA [274], Skxs20 [275]. Most of these results deviate from the $\Lambda_v = 0.0$ curve, but matches well with our calculations for non-zero value of Λ_v within a considerable density.

The slope parameter L_{sym}, curvature K_{sym} and skewness Q_{sym} for different values of Λ_v are displayed in Fig. 6.2. From the figure, it is clear that the variation of L_{sym}, K_{sym} and Q_{sym} with Λ_v is quite substantial.

$$Q_{sym} = 27\rho^3 \left(\frac{\partial^3 E_{sym}}{\partial \rho^3}\right)_{\rho=\rho_0}. \tag{6.10}$$

Recently, several studies have been done to fix the constraint on E_{sym} and L_{sym} [117, 264–267,269]. We also calculate the constraint on E_{sym} and L_{sym} at saturation density (ρ_0) with various Λ_v as shown in Fig. 6.3. The experimental data at HIC [276], PDR [277,278], IAS [279] and the theoretical predictions of finite range droplet model (FRDM) [280] and Skyrme Hartree-Fock formalism [117] are given for comparison.

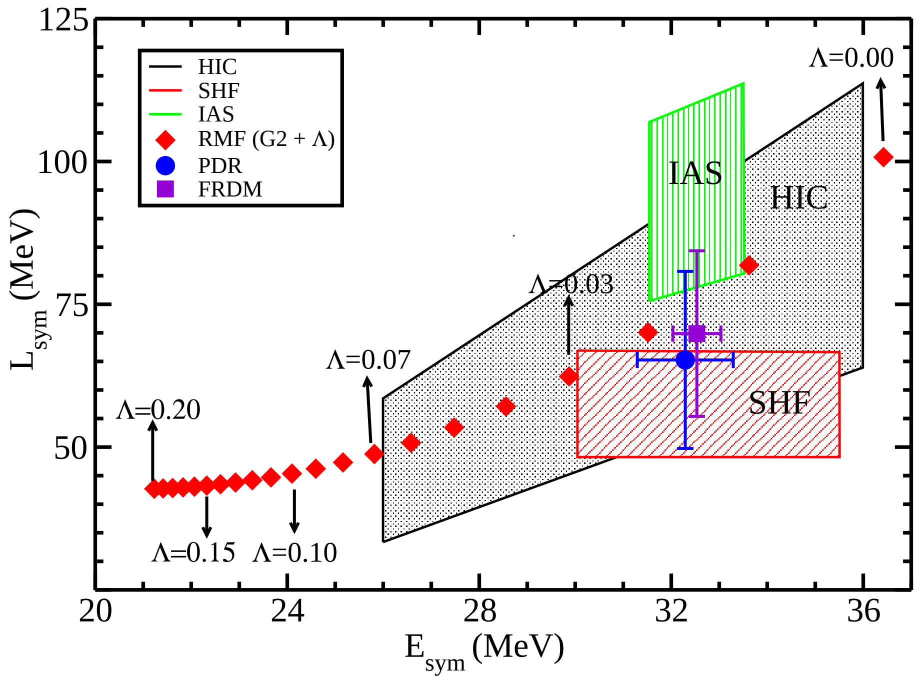

Figure 6.3: The L_{sym} with respect to Symmetry energy E_{sym} on saturation density at different values of Λ compare with SHF [117], HIC [276], PDR [277, 278], IAS [279], and FRDM [280] flow data results.

Table 6.1: The numerical results of symmetry energy E_{sym}(MeV), slope co-efficient L_{sym}(MeV), K_{sym}(MeV) and Q_{sym}(MeV) at different values of Λ_v are listed.

Λ_v	E_{sym}	L_{sym}	K_{sym}	Q_{sym}	Λ_v	E_{sym}	L_{sym}	K_{sym}	Q_{sym}
0.00	36.42	100.75	-7.44	44.02	0.11	23.66	44.71	-6.66	297.27
0.01	33.62	81.83	-63.61	169.40	0.12	23.27	44.20	-2.27	263.20
0.02	31.52	70.07	-75.61	336.90	0.13	22.92	43.81	1.50	231.61
0.03	29.87	62.36	-71.69	440.67	0.14	22.61	43.50	4.74	202.57
0.04	28.56	57.11	-62.41	485.92	0.15	22.32	43.26	7.53	176.02
0.05	27.48	53.41	-51.91	492.07	0.16	22.07	43.08	9.94	151.83
0.06	26.58	50.75	-41.81	474.95	0.17	21.83	42.94	12.02	129.84
0.07	25.82	48.79	-32.69	445.14	0.18	21.61	42.83	13.82	109.89
0.08	25.16	47.32	-24.68	409.26	0.19	21.41	42.75	15.38	91.78
0.09	24.60	46.21	-17.74	371.28	0.20	21.23	42.69	16.74	75.36
0.10	24.10	45.36	-11.78	333.52	0.21	21.06	42.66	17.92	60.47

From the figure, it is clear that for Λ_v=0.0, E_{sym} is out side the experimental region. The calculated results are within the range for $\Lambda_v \sim$ 0.02 - 0.06. It goes again beyond the shaded region (HIC data) [276] for larger value of Λ_v. This analysis suggests the limiting value of Λ_v as well as to include the $\omega-\rho-$coupling in the E-RMF Lagrangian to improve the E-RMF(G2) parametrization. Thus an improve parameter set E-RMF(G2+Λ_v) on top of G2 is the need of present day research keeping in view of the upcoming experiments [281–283].

6.4 Baryonic Matter in $\beta-$equilibrium

6.4.1 Neutron Star (n, p, e)

In this section, we study the effect of isoscalar-scalar and isovector-vector coupling with different coupling strength Λ_v on top of G2 parameter set in neutron star. Here we consider the equilibrium system with n, p and e only, with n is denoted as neutron, p is the proton and e is the electron of the system. In the interior of the neutron star, the neutron chemical potential exceeds the combined mass of the proton and electron. Therefore, asymmetric matter with an admixture of electrons rather than pure neutron matter, is a more likely composition of matter in neutron star interiors. The concentrations of neutrons, protons and electrons can be determined from the condition of $\beta-$equilibrium $1n \leftrightarrow 1p + 1e + 1\bar{\nu}$ and from charge neutrality, assuming that neutrinos are not degenerate. We have $\nu_n = \nu_p + \nu_e$, $n_p = n_e$, where $\nu_n = \mu_n - g_\omega V_0 + \frac{1}{2}g_\rho b_0$ and $\nu_p = \mu_p - g_\omega V_0 - \frac{1}{2}g_\rho b_0$ with $\mu_n = \sqrt{(k_{fn}^2 + M^{*2})}$ and $\mu_p = \sqrt{(k_{fp}^2 + M^{*2})}$ are the chemical potential, and k_{fn} and k_{fp} are the Fermi momentum for neutron and proton, respectively. Imposing this conditions, in the expressions of $\mathcal{E}$ and $\mathcal{P}$ (Eqns. 6.1-6.2), we evaluate $\mathcal{E}$ and $\mathcal{P}$ as a function of density. To calculate the star structure, we use the Tolman-Oppenheimer-Volkoff (TOV) equations for the structure of a relativistic spherical and static star composed of a perfect fluid were derived from Einstein's equations [99], where the pressure and energy densities obtained from equations (9) and (10) are the inputs. The TOV equation is [99]:

$$\frac{d\mathcal{P}}{dr} = -\frac{1}{r}\frac{[\mathcal{E}+\mathcal{P}]\,[M+4\pi r^3\mathcal{P}]}{(r-2GM)}, \tag{6.11}$$

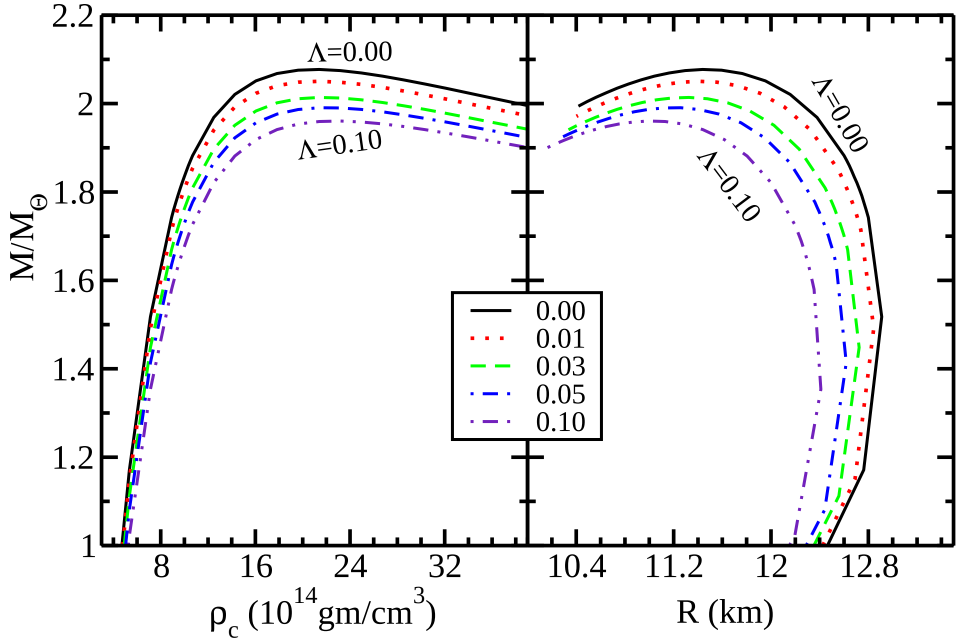

Figure 6.4: The neutron star (n, p, e) mass as a function density and radius for G2 parameter set at different value of Λ_v.

$$\frac{dM}{dr} = 4\pi r^2 \mathcal{E}, \tag{6.12}$$

with G as the gravitational constant and $M(r)$ as the enclosed gravitational mass. We have used $c = 1$. Given the $\mathcal{P}$ and $\mathcal{E}$, these equations can be integrated from the origin as an initial value problem for a given choice of central energy density, (ε_c). The value of $r\ (= R)$, where the pressure vanishes defines the surface of the star.

We calculate the mass of the neutron star as a function of density and radius. The results are given in the right and left panel of the Fig. 6.4, respectively. We find a variation of star mass from 2.077 $M_\odot$ to 1.961 $M_\odot$ with a change of $\Lambda_v = 0.0$ to 0.1 and the respective radii are 11.438 Km and 10.994 Km. This change is about 4% in radius and $\sim\ 6\%$ in mass of the star. Thus a finer tuning in mass and radius of neutron star is possible by a suitable adjustment on Λ_v value in the extended parametrization of $G2 + \Lambda_v$ to keep the star properties within the recent experimental observations [96].

6.4.2 Neutron Star (Octet, e, μ)

Upto this level we are considering the composition of neutron star is only neutron, proton and electron. But due to the very high density ($\sim$ 7-8ρ_0) of neutron star at the core, other baryons of the octet family apart from neutron and proton become important in the equation of state [284–288]. It is to be noted that other strange mesons (like $\sigma*, \omega*$) are also important at such high density [289], however we are confined to the E-RMF (G2) model and not included their effects in the calculations. In this section, we extend our calculations to the octet system (n, p, Λ^0,$\Sigma^{0,\pm1}$, $\Xi^{-,0}$) of neutron star (Hyperon Star) with Λ_v to see the effect. Although, a large number of studies have been done [36, 290, 291] using $G1$ and $G2$ forces for finite and infinite nuclear matter properties, not much applications have done for octet system. For simplicity, on the basis of the quark model, one can assume all the hyperons in the octet system have the same coupling ratio with mesons, they are expressed as [292]: $x_\sigma = x_{H_\sigma}/x_{N_\sigma} = \sqrt{2/3}$, $x_\omega = x_{H_\omega}/x_{N_\omega} = \sqrt{2/3}$ and $x_\rho = x_{H_\rho}/x_{N_\rho} = \sqrt{2/3}$. However, this assumption is considered to be naive and unrealistic [293, 294]. It is worthy to mention that, although we calculate the properties of baryonic systems with various parametrizations [293, 295], in the work, we have only used the coupling strengths of Ref. [295]. This parametrization also helps to investigate the relevance of the considered EOS at high density. The electron e and muon μ are included for maintaining the charge neutrality and $\beta-$ equilibrium condition for the octet system under the weak interaction [291, 296]:

$$B_1 \to B_2 + l + \overline{\nu_l}; \qquad\qquad B_2 + l \to B_1 + \nu_l,$$

where B_1, B_2, l, ν, $\overline{\nu}$ are baryons, leptons, neutrino and antinuetrino respectively. In case of octet system, we are dealing with neutron star (real system), which become unstable with a small change in the system. The equation of state obtained for nuclear matter (proton and neutron only) as well as for octet system are shown in Fig. 6.5 for $G2 + \Lambda_v$. At high density, the octet EOS becomes stiffer by increasing the value of Λ_v, but it behaves in different way at low density region. The equation of state for pure nucleon (with $\beta-$equilibrium and charge neutrality condition) becomes softer with increasing Λ_v over the whole density region (see Fig. 6.5). We compare the results with the empirical data for r_{ph}=R with uncertainty 2σ of Steiner *et al.* [297, 298]. Here R is neutron radius and r_{ph} is photospheric radius. Including the octet, we also plotted the results of nucleon EOS at different values of Λ_v. The nucleon EOS well matches with the data at low and high densities, but the octet

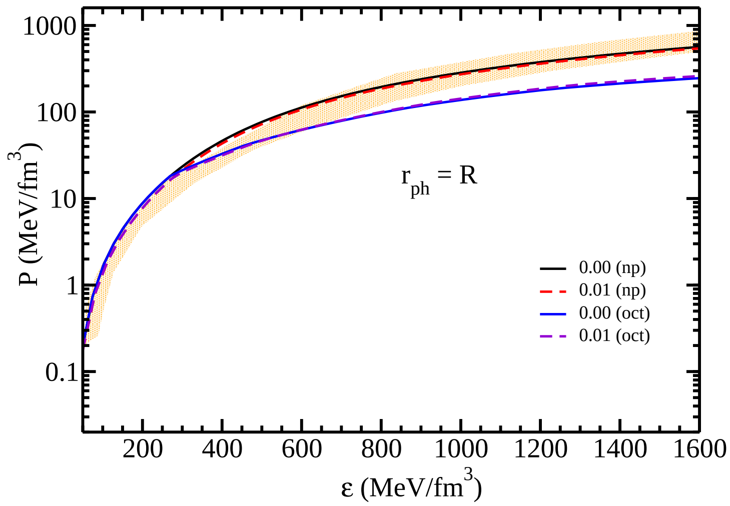

Figure 6.5: Equation of states (EOS) for octet and nucleon system at different Λ_v. G2 set is used for nucleonic and the coupling strength for hyperons are used from Ref. [295]. The empirical EOS obtained by Steiner *et al.* for r_{ph}=R with uncertainty of 2σ [297] (shaded region in the graph) is given for comparison.

EOS deviates at high value of ρ_B. It only coincides with the empirical values at intermediate density. Inclusion of these other octet family with neutron and proton make the EOS softer as shown in Fig. 6.5 and reduce the neutron star mass [299–302]. We also calculated the mass of neutron star with the baryonic octet and two leptons (e, μ) (Hyperon Star) as shown in Fig. 6.6. The ratio of hyperon star to the solar mass (M/M$_\odot$) with respect to density (10^{14} gm/cm^3) of the system at different values of Λ_v are shown in Figure 6. One can easily see that the effect of Λ_v in hyperon star behaves in different way as correspond to the neutron star with only n, p and e, i.e. mass of the star increases with Λ_v. The radius R of the hyperonic star is also estimated and it is decreases with Λ_v which can be realized from Fig. 6.5. From this analysis, we noticed an impressive observation, the influence of Λ_v in addition with the G2 parameter set is not much on the octet equation of state, because of the dominance of the self interaction of the isoscalar vector meson (ζ_0 coupling constant). But this isoscalar-vector and isovector-vector coupling is crucial for a finer refinement of the octet system.

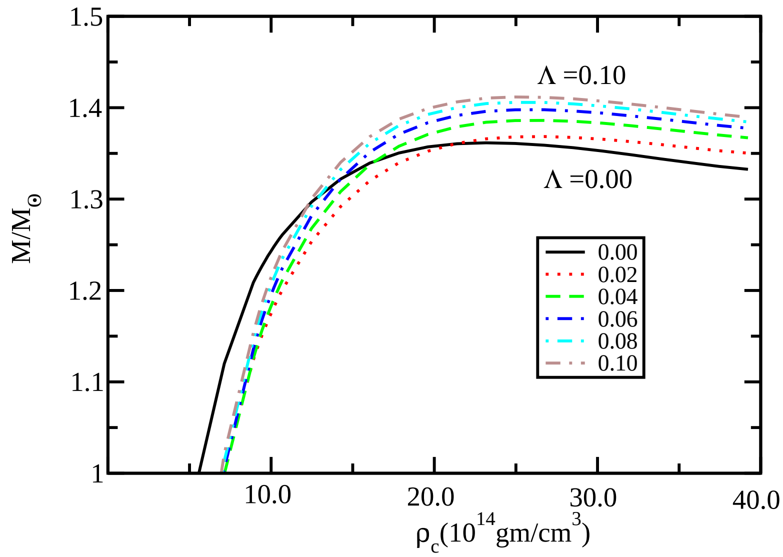

Figure 6.6: The hyperon star (octet, e, μ) mass as a function density for G2 parameter set at different value of Λ_v.

6.4.3 Composition of nuclear Matter

The relative yields of the octet system is calculated in two different parametrizations: (i) same coupling ratios as assumed by the quark model [292] and (ii) different couplings for different baryons [293, 295]. These results are shown in Fig. 7 (a) and Fig. 7 (b) for different Λ_v, respectively. The solid line presents the yield at Λ_v=0.00 and at Λ_v=0.01 by dashed line. One can easily see that within the constant coupling approximation, first Σ^-hyperon generate at $\sim 1.9\rho_0$. The yield of this hyperon increases rapidly upto $\sim 3\rho_0$ and then saturated. Just after this, the $\Lambda-$ hyperon generated at $\sim 2.1\rho_0$ and the yield becomes constant at $\sim 5.1\rho_0$. The effect of $\omega - \rho$ coupling can be easily seen from the yield curve (solid and dashed lines) for $\Xi^{-,0}$ which are started from $\sim 4.5\rho_0$ and $\sim 7.0\rho_0$, respectively. By increasing the cross-coupling constant Λ_v, the origin of the $\Xi^{-,0}$ changes significantly. In Fig. 7(b), different coupling constants are used for various hyperons and nucleons family to see the effect of Λ_v particle fraction in nuclear matter within $\beta-$equilibrium and charge neutrality condition. Here, we get almost similar results for p, n, and $\Sigma^{\pm,0}$ as in Fig. 7(a). A further inspection of these two figures reveals that the production of different hyperons occur at a higher density when we consider different coupling strengths ((ii) case). For example, Σ^0 produced at $\sim 4.0\rho_0$ in case (i) and it is at $\sim 5.4\rho_0$ for case (ii). In general, the effect of Λ_v coupling on the yield product on the octet family does not seem significant,

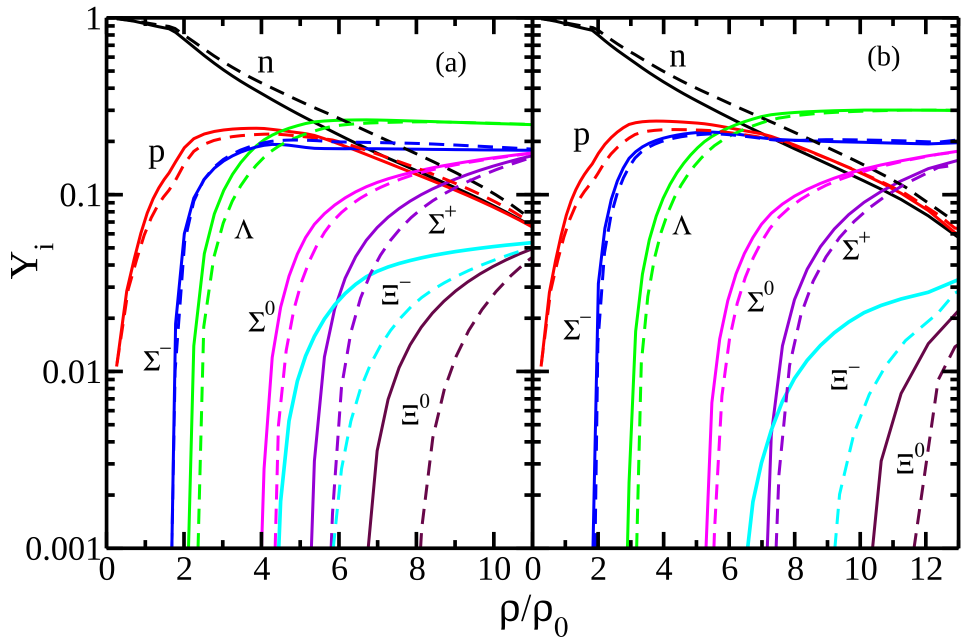

Figure 6.7: The yield of $nucleon$, Λ, Σ and Ξ (Y_i) as a function of baryon density for G2 parameter set at different value of Λ_v. The results are obtained for constant [292] (a) and different coupling strengths [295] (b) for baryon-hyperon.

except for Ξ.

6.5 Summary and Conclusions

We study the sensitivity of the cross-coupling $\omega - \rho$ with the coupling constant Λ_v on symmetry energy E_{sym} and nuclear equation of state. The constant Λ_v is introduced on top of the recently developed G2 parameter set. From the analysis, we found that Λ_v is a crucial quantity responsible for a finer tuning of the symmetry energy as well as EOS. The E_{sym} is found to be softer with Λ_v to a maximum value of $\Lambda_v \sim 0.15$. Our calculated result matches well with the experimental data as well as other theoretical predictions for E_{sym} and L_{coeff} at $\rho = \rho_0$ for different values of Λ_v. However, this results deviate from the experimental range when ignore the cross-coupling. The effect of Λ_v on neutron star properties, such as mass $M/M_\odot$ and radius (R) are also studied and found that, with the help of this coupling, one can modify these observables to some limit. In case of octet system, the coupling term containing Λ_v plays an important role in finer adjustment of the equation of state and Y_i. Thus, we may say that this interaction $\omega - \rho$ is crucial for both cases (nucleon and hadron).

Chapter 7

Effect of isospin asymmetry in nuclear system

The effect of $\delta-$ and $\omega-\rho-$meson cross couplings on asymmetric nuclear systems are analyzed in the frame-work of an effective field theory motivated relativistic mean field formalism. The calculations are done on top of the G2 parameter set, where these contributions are absent. We analyzed the root mean square charge radius, binding energy, single particle energy (for the 1^{st} and last occupied orbits), density and spin-orbit interaction potential for some selected nuclei. We evaluate the $L_{sym}-$ and $K_{sym}-$ coefficients for nuclear matter as function of $\delta-$ and $\omega-\rho-$meson coupling strengths. As expected, the influence of these effects are negligible for symmetry nuclear system and these effects are important for systems with large isospin asymmetry.

7.1 Introduction

In recent years the effective field theory approach to quantum hadrodynamic (QHD) has been studied extensively. The parameter set G2 [142,143], obtained from the effective field theory motivated Lagrangian (E-RMF) approach, is quite successful in reproducing the nuclear matter properties including the structure of neutron star as well as of finite nuclei [36]. This model well reproduce the experimental values of binding energy, root mean square (rms) radii and other finite nuclear properties [103,173]. Similarly, the prediction of nuclear matter properties including the phase transition as well as the properties of compact star are remarkably good [291]. The G2 force parameter is the largest force set available, in the relativistic mean field model. It contains almost all interaction terms of nucleon with mesons, self and cross coupling of mesons upto 4^{th} order.

In the E-RMF model of Furnstahl et al. [142,143], the coupling of $\delta-$meson is not taken into account. Also, the effect of ρ and ω meson cross coupling was neglected. It is soon realized that the importance of δ meson [45] and the cross coupling of ω and $\rho-$mesons [303] can not be neglected while studying the nuclear and neutron matter properties. Horowitz and Piekarewicz [91] studied explicitly the importance of $\rho-$ and $\omega-$ cross coupling to finite nuclei as well as to the properties of neutron star structures. This coupling also influences the nuclear matter properties, like symmetry energy E_{sym}, slope parameters L_{sym} and curvature K_{sym} of E_{sym} [268].

The observation of Brown [88] and later on by Horowitz and Piekarewicz [91] make it clear that the neutron radius of heavy nuclei has a direct correlation with the equation of state (EOS) of compact star matter. It is shown that the collection of neutron to proton radius difference $\triangle r = r_n - r_p$ using relativistic and nonrelativistic formalisms show two different patterns. Unfortunately, the error bar in neutron radius makes no difference between these two pattern. Therefore, the experimental result of JLAB [304] is much awaited. To have a better argument for all this, Horowitz and Piekarewicz [91] introduced Λ_s and Λ_v couplings to take care of the skin thickness in ^{208}Pb as well as the crust of neutron star. The symmetry energy, and hence the neutron radius, plays an important role in the construction of asymmetric nuclear EOS. Although, the new couplings Λ_s and Λ_v take care of the neutron radius problem, the effective mass splitting between neutron and proton is not taken care. This effect can not be neglected in a highly neutron-rich dense matter system and drip-line nuclei. In addition to this mass splitting, the rms charge radius anomaly of ^{40}Ca and ^{48}Ca may be resolved by isovector-scalar $\delta-$meson inclusion to the E-RMF model.

7.2 Results and Discussions

As we know isospin of the system plays a very crucial role in drip-line nuclei and its contribution can not be ignored in the asymmetric system. Now a days, going far from the

$\beta-$stable line nuclei to unstable one easy due to the availability of the experimental facilities in the international communities. By keeping these facts, we included the extra degree of freedom in the system by introducing the $\delta-$meson in well established Lagrangian of Ref. [143]. For our analysis, we took two type of methodology:

- We included the delta meson on top of G2 Lagrangian and analyzed behaviour of the system by changing the coupling strength of $\delta-$meson. First part of this chapter will mainly focus on this methodology and see the effect of $\delta-$meson coupling on finite and infinite nuclear systems and we extend our calculation to neutron star [305].
- We split the isospin contribution of the system between $\rho-$ and $\delta-$meson. The behavior of system within this modified parameter are analyzed and given in separate section. We follow the similar strategy as discussed in first point [306].

7.2.1 The $\delta-$meson coupling on top of G2 parameter

Our calculated results are shown in Figs. 7.1-7.9 for both finite nuclei and infinite nuclear matter systems. The effect of $\delta-$meson and the crossed coupling constant Λ_v of $\omega-\rho$ fields on some selected nuclei like ^{48}Ca and ^{208}Pb are demonstrated in Figs. 7.1-7.4 and the nuclear matter outcomes are displayed in rest of the figures and table. In one of our recent publication [268], the explicit dependence of $\Lambda_v(\omega-\rho)$ on nuclear matter properties are shown and it is found that it has significant implication on various physical properties, like mass and radius of neutron star and E_{sym} asymmetry energy and its slope parameter L_{sym} for infinite nuclear matter system at high densities. Here, only the influence of Λ_v on finite nuclei and that of g_δ on both finite and infinite nuclear systems are studied.

Finite Nuclei

In this section we analyzed the effects of δ meson and Λ_v coupling in finite nuclei. For this, we calculate the binding energy (BE), rms radii (r_n, r_p, r_{ch}, r_{rms}), and energy of first and last filled orbitals of ^{48}Ca and ^{208}Pb with g_δ and Λ_v. The finite size of the nucleon is taken into account for the charge radius using the relation $r_{ch}=\sqrt{r_p^2+0.64}$. The results are shown in Figs. 7.1, 7.2.

In our calculations, while analyzing the effect of g_δ, we keep $\Lambda_v=0$ and vice versa. From the figures, it is evident that the binding energy, radii and single particle levels $\epsilon_{n,p}$

Figure 7.1: Binding energy (BE), root mean square radius and first ($1s^{n,p}$) and last ($1f^{n}$, $2s^{p}$) occupied orbits for ^{48}Ca as a function of g_δ and Λ_v.

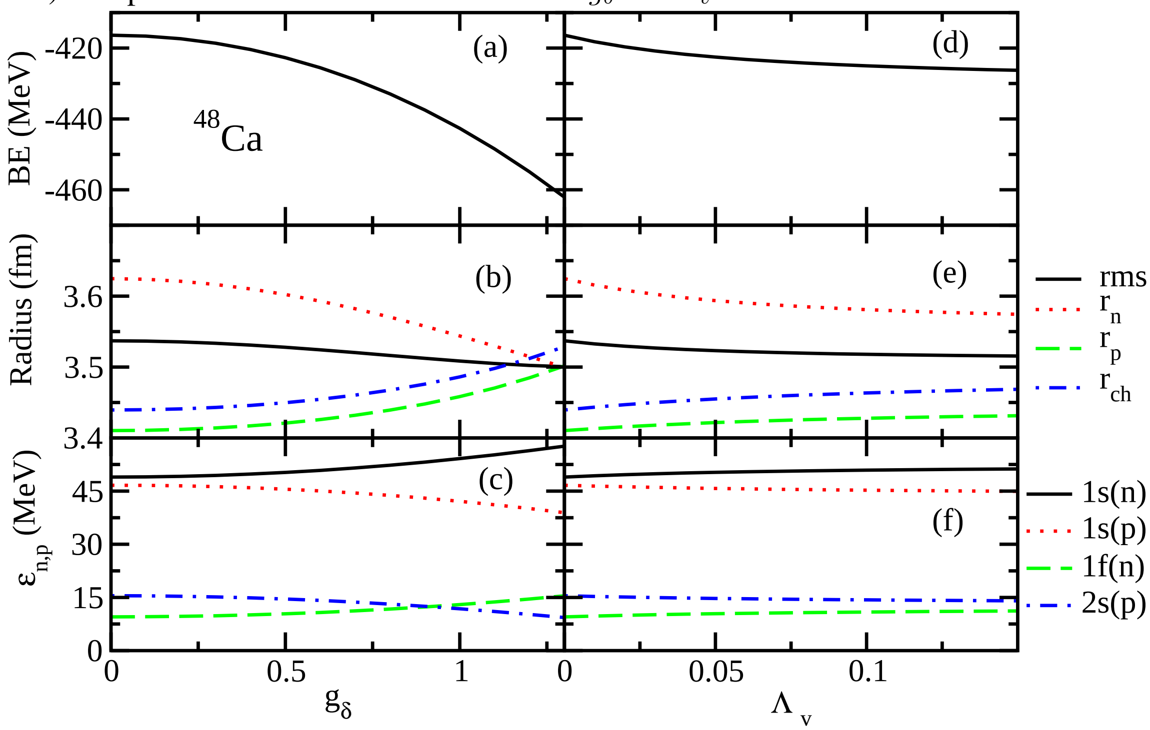

Figure 7.2: Same as Fig. 7.1 for ^{208}Pb.

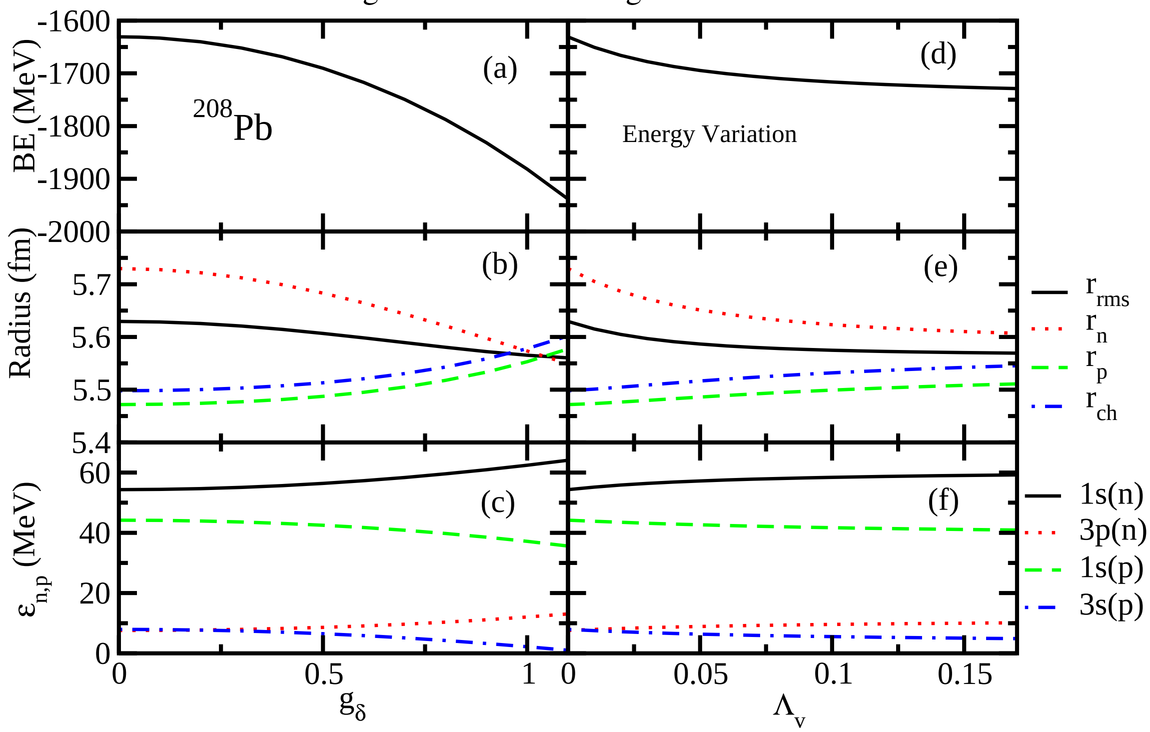

affected drastically with g_δ contrary to the effect of Λ_v. A careful inspection shows a slight decrease of r_n with the increase of Λ_v consistent with the analysis of [307]. Again, it is found that the binding energy increases with increasing of the coupling strength upto $g_\delta \sim 1.5$ and no convergence solution available beyond this value. Similar to the g_δ limit, there is limit for Λ_v also, beyond which no solution exist. From the anatomy of g_δ on r_n and r_p, we find their opposite trend in size. That means the value of r_n decreases and r_p increases with g_δ for both ^{48}Ca and ^{208}Pb. It so happens that both the radii meet at a point near $g_\delta = 1.0$ (Fig 7.1 and Fig. 7.2) and again shows reverse character on increasing g_δ, i.e., the neutron skin thickness ($r_n - r_p$) changes its sign with g_δ. This interesting results may help us to settle the charge radius anomaly of ^{40}Ca and ^{48}Ca.

In Fig. 7.1(c), we have shown the first ($1s^{n,p}$) and last ($1f^n$ and $2s^p$) filled orbitals for ^{48}Ca as a function of g_δ and Λ_v. The effect of Λ_v is marginal, i.e., almost negligible on $\epsilon_{n,p}$ orbitals. However, this is significance with the increasing value of g_δ. The top most filled orbital even crosses each other at $g_\delta \sim 1$, although initially, it is well separated. On the other hand, the first filled orbital $1s$ both for proton and neutron get separated more and more with g_δ, which has almost same single particle energy $\epsilon_{n,p}$ at $g_\delta = 0$. We get similar trend for ^{208}Pb, which is shown in Fig. 7.2(c). In both the representative cases, we notice orbital flipping only for the last filled levels.

The nucleon density distribution (proton ρ_p and neutron ρ_n) and spin orbit interaction potential E_{so} of finite nuclei are shown in Figs. 7.3 and 7.4. The calculations are done with two different values of g_δ and Λ_v as shown in the figures. Here, the solid line is drawn for initial and dotted one is for the limiting values. In Fig. 7.3(a), we have depicted the neutron, proton and total density distribution for ^{48}Ca at values of $g_\delta = 0.0$ and 1.3. Comparing Figs. 7.3(a) and 7.3(c), one can see that the sensitivity of g_δ is more than Λ_v on density distribution. The spin-orbit potential E_{so} of ^{48}Ca with different values of g_δ are shown in Fig. 7.3(b) and for Λ_v in Fig. 7.3(d). Similarly, we have given these observables for ^{208}Pb in Fig. 7.4. In general, for light mass region both coupling constants g_δ and Λ_v are less effective in density distribution and spin-orbit potential. It is clear from this analysis that the coupling strength of $\delta-$meson is more influential than the isoscalar-vector and isovector-vector cross coupling. This effect is mostly confined to the central region of the nucleus.

Figure 7.3: The neutron, proton and total density with radial coordinate $r(fm)$ at different values of g_δ (a) and Λ_v (c). The variation of spin-orbit potential for proton and neutron are shown in (b) and (d) by keeping the same g_δ and Λ_v as (a) and (c) respectively.

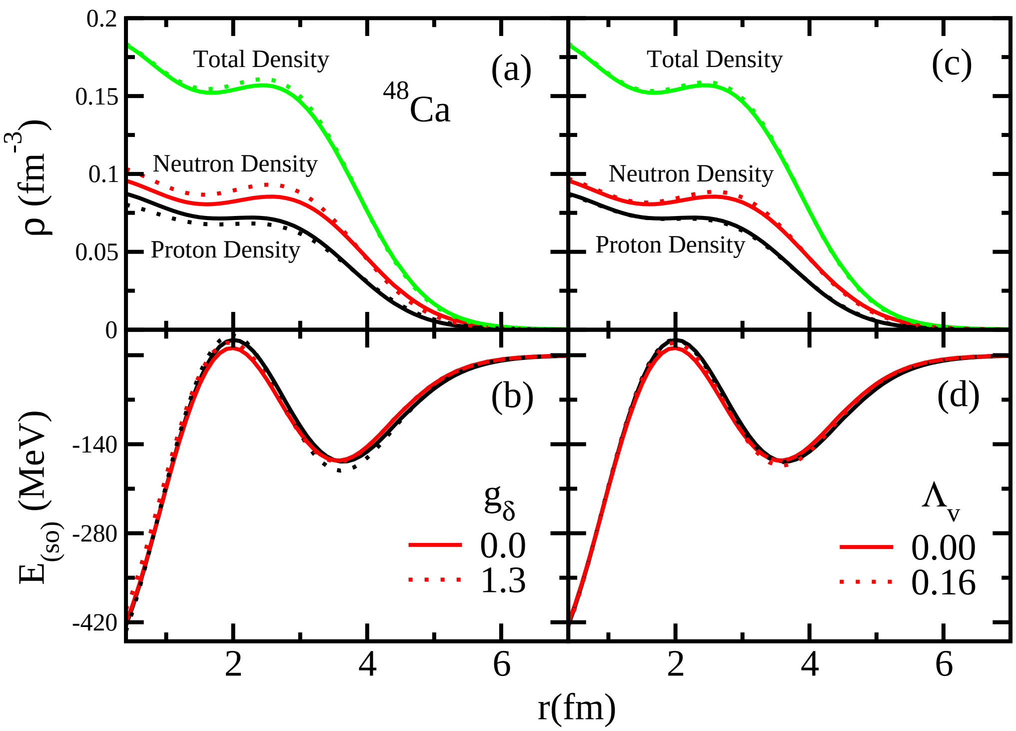

Figure 7.4: Same as Fig. 7.3 for ^{208}Pb.

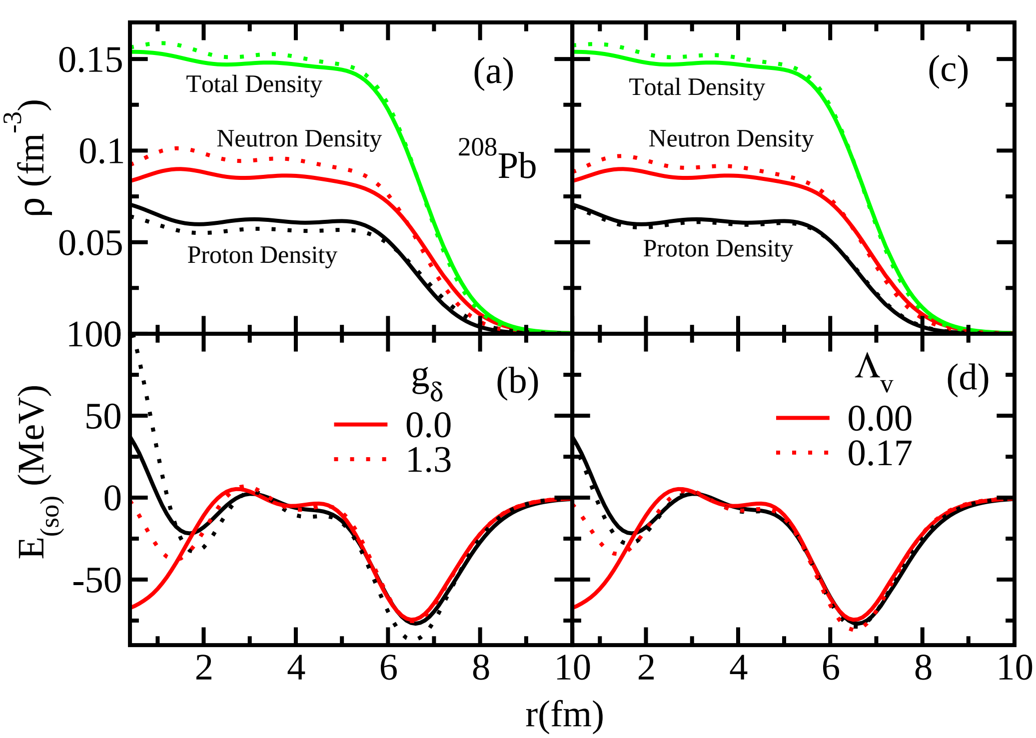

Nuclear Matter

In this section, we do calculation for nuclear matter properties like energy density and pressure, symmetry energy, radii and mass of the neutron star using $\omega - \rho$ and δ couplings on top of G2 parametrization. Recently, it is reported [268] that the $\omega - \rho$ cross coupling plays a vital role for nuclear matter system on important physical observables like equation of state, symmetry energy coefficient, L_{sym} coefficient etc. A detail account is available in Ref. [268] for $\omega - \rho$ coupling on nuclear matter system. The main aim of this section is to take δ meson as an additional degree of freedom in our calculations and elaborate the effect on nuclear matter system within G2 parameter set. In highly asymmetric system like neutron star and supernova explosion, the contribution of δ meson is important. This is because of the high asymmetry due to the isospin as well as the difference in neutron and proton masses. Here, in the calculations the $\beta-$equilibrium and charge neutrality conditions are not considered. We only varies the neutron and proton components with an asymmetry parameter α, defined as $\alpha = \frac{\rho_n - \rho_p}{\rho_n + \rho_p}$. The splitting in nucleon masses is evident from equations (16) and (17) due to the inclusion of isovector scalar $\delta-$meson. For α=0.0, the nuclear matter system is purely symmetrical and for other non-zero value of α, the system get more and more asymmetry. For $\alpha = 1.0$, it is a case of pure neutron matter.

In Fig. 7.5(a), the effective masses of proton and neutron are given as a function of g_δ. As we have mentioned, $\delta-$meson is responsible for the splitting of effective masses (Eqns. (16) and (17)), this splitting increases continuously with coupling strength g_δ. In Fig. 7.5, the splitting is shown for few representative cases at α=0.0, 0.75 and 1.0. The solid line is for α=0.0 and α=0.75, 1.0 are shown by dotted and dashed line, respectively. From the figure, it is clear that the effective mass is unaffected for symmetric matter. The proton effective mass M_p^* is above the reference line with $\alpha = 0$ and the neutron effective mass always lies below it. The effect of g_δ on binding energy per nucleon is shown in Fig. 7.5(b) and pressure in Fig. 7.5(c). One can easily see the effect of δ meson interaction on the energy density and pressure of the nuclear system. The energy density and pressure show opposite trend to each other with the increase function of g_δ.

Figure 7.5: Variation of nucleonic effective masses, binding energy per particle (BE/A) and pressure as a function of g_δ on top of G2 parameter set for nuclear matter.

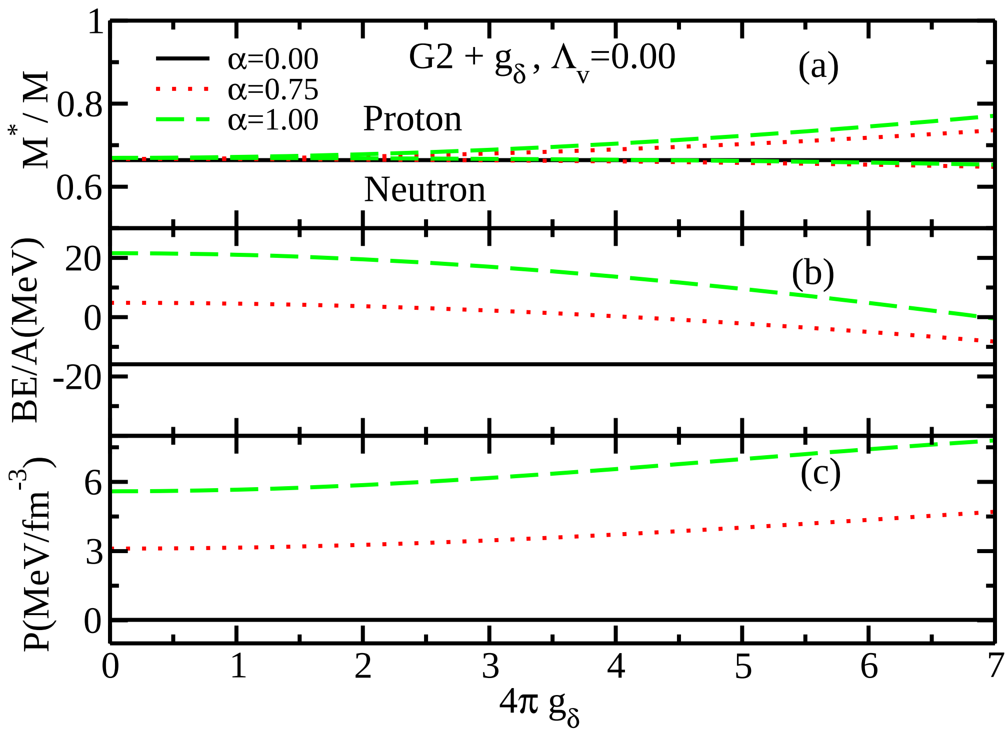

Energy and Pressure Density

We analyze the binding energy per nucleon and pressure including the contribution of $\delta-$meson in the G2 Lagrangian as a function of density. As it is mentioned earlier, the addition of $\delta-$meson is done due to its importance on asymmetry nuclear matter as well as to make a full fledged E-RMF model. This is tested by calculating the observables at different values of $\delta-$meson coupling strength g_δ. In Fig. 7.6, the calculated BE/A and $\mathcal{P}$ for pure neutron matter with baryonic density for different g_δ are shown. Unlike to the small value of g_δ upto 1.5 in finite nuclei, the instability arises at g_δ=7.0 in nuclear matter. Of course, this limiting value of g_δ depends on the asymmetry of the system.

In Fig. 7.6(a), we have given BE/A for different values of g_δ. It is seen from Fig. 7.6(a), the binding increases with g_δ in the lower density region and maximum value of binding energy is $\sim$ 7 MeV for g_δ=7.0. On the other hand, in higher density region, the binding energy curve for finite g_δ crosses the one with g_δ=0.0. That means, the EOS with $\delta-$meson is stiffer than the one with pure G2 parametrization. As a result, one get a heavier mass of the neutrons star, which suited with the present experimental finding [96]. For comparing the data at lower density (dilute system, $0 < \rho/\rho_0 < 0.16$) the zoomed version of the region is shown as an inset Fig. 7.6(c) inside Fig. 7.6(a). From the zoomed inset portion, it is clearly seen that the curves with various g_δ at $\alpha = 1.0$ (pure neutron matter) deviate from other theoretical predictions, such as Baldo-Maieron [308], DBHF [309], Friedman [310], auxiliary-field diffusion Monte Carlo (AFDMC) [311] and Skyrme interaction [117]. This is an inherited problem in the RMF or E-RMF formalisms, which need more theoretical attention. Similarly, the pressure for different values of g_δ with G2 parameter set are given in Fig. 7.6(b). At high density we can easily see that the curve becomes more stiffer with the coupling strength g_δ. The experimental constraint of equation of state obtained from heavy ion flow data for both stiff and soft EOS is also displayed for comparison in the region $2 < \rho/\rho_0 < 4.6$ [312]. Our results match with the stiff EOS data of Ref. [312].

Symmetry Energy

The symmetry energy E_{sym} is obtained by the energy difference of symmetry and pure neutron matter at saturation. The results for E_{sym} are given in Fig. 7.7 with experimental heavy ion collision (HIC) data [269] and other theoretical predictions of non-relativistic

Figure 7.6: Energy per particle and pressure with respect to density with various g_δ.

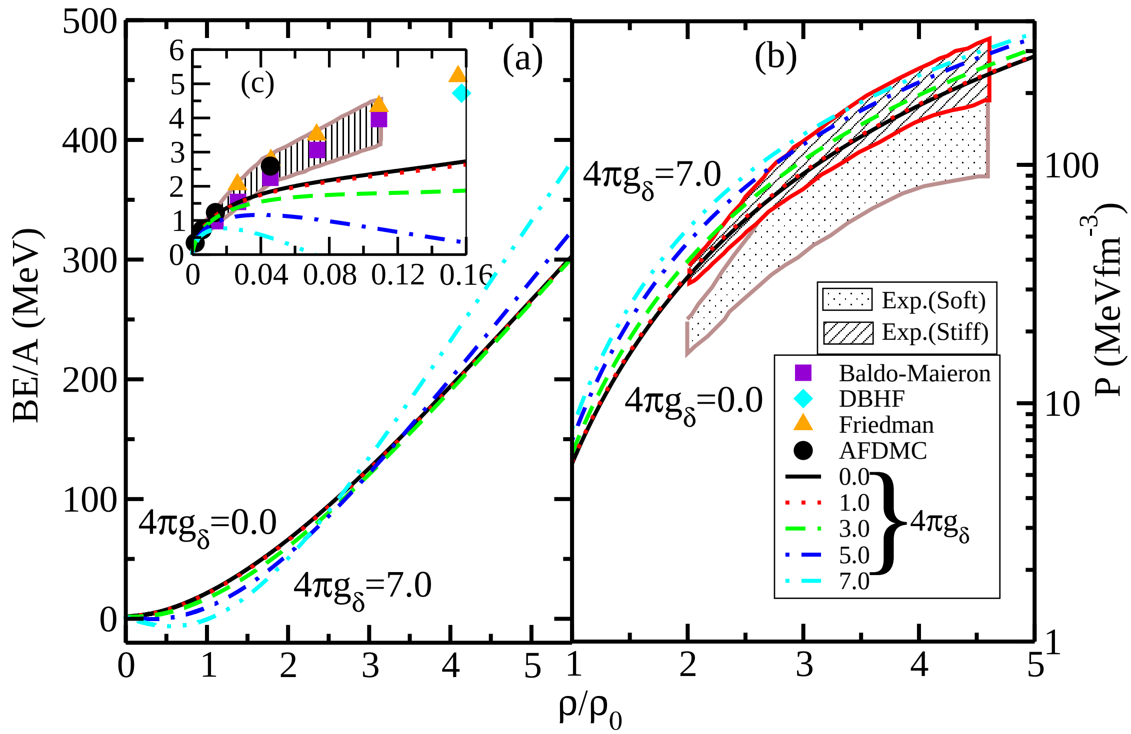

Skyrme-Hartree-Fock model. The calculation is done for pure neutron matter with different values of g_δ, which are compared with two selective force parameter sets GSkII [270] and Skxs20 [275]. For more discussion one can see Ref. [117], where 240 different Skyrme parametrization are used. Here, the calculations are performed by taking $\Lambda_v = 0$ to see the effect of $\delta-$meson coupling on E_{sym}. In this figure, shaded region represent the HIC data [269] within $0.3 < \rho/\rho_0 < 1.0$ region and the symbols square and circle represent the SHF results for GSkII and Skxs20, respectively. Analysing the Fig. 7.7, E_{sym} of G2 force matches with the shaded region in low density region, however as the density increases, the value of E_{sym} moves away. Again, the symmetry energy becomes softer by increasing the value of coupling strength g_δ. For higher value of g_δ, again the curve moves far from the empirical shaded area. In this way, one can fix the limiting constraint on coupling strength of $\delta-$meson with the nucleons. Similar to the finite nuclear case, the nuclear matter system becomes unstable for excessive value of g_δ (> 7.0). This constrained may help to improve the G2+g_δ parameter set for both finite and infinite nuclear systems.

In Fig. 7.8, we have given the symmetry energy with its first derivative at saturation density (L_{sym}) with different values of coupling strength staring from $g_\delta \times 4\pi = 0.0 - 7.0$. The variation in symmetry energy takes place from 45.09 to 20.04 MeV, L_{sym} from 120.60 to 55.78 MeV and K_{sym} from -29.28 to 13.27 MeV at saturation density corresponding to $0.0 < g_\delta \times 4\pi < 7.0$. From this investigation, one can see that G2 set is not sufficient to predict the constrained on E_{sym} and L_{sym}. It is suggestive to introduce the $\delta-$meson as an extra degree of freedom into the model to bring the data within the prediction of experimental and other theoretical constraints.

Neutron Star

In this section, we study the effect of $\delta-$meson on mass and radius of neutron star. Recently, experimental observation predicts the constraint on mass of neutron star and its radius [96]. This observation suggests that the theoretical models should predict the star mass and radius as $M \geq (1.97 \pm 0.04)M_\odot$ and $11 < R(km) < 15$. Keeping this point in mind, we calculate the mass and radius of neutron star and analyzed their variation with g_δ.

The results of mass and radius with various $\delta-$meson coupling strength g_δ is shown in Fig. 7.9. In left panel, the neutron star mass with density (gm/cm^3) is given, where we can see the effect of the newly introduced extra degree of freedom $\delta-$meson into the system.

Figure 7.7: Symmetry energy E_{sym} (MeV) of neutron matter with respect to different value of g_δ on top of G2 parameter set. The heavy ion collision (HIC) experimental data [269] (shaded region) and non-relativistic Skyrme GSkII [270], and Skxs20 [275] predictions are also given. Λ_v=0.0 is taken.

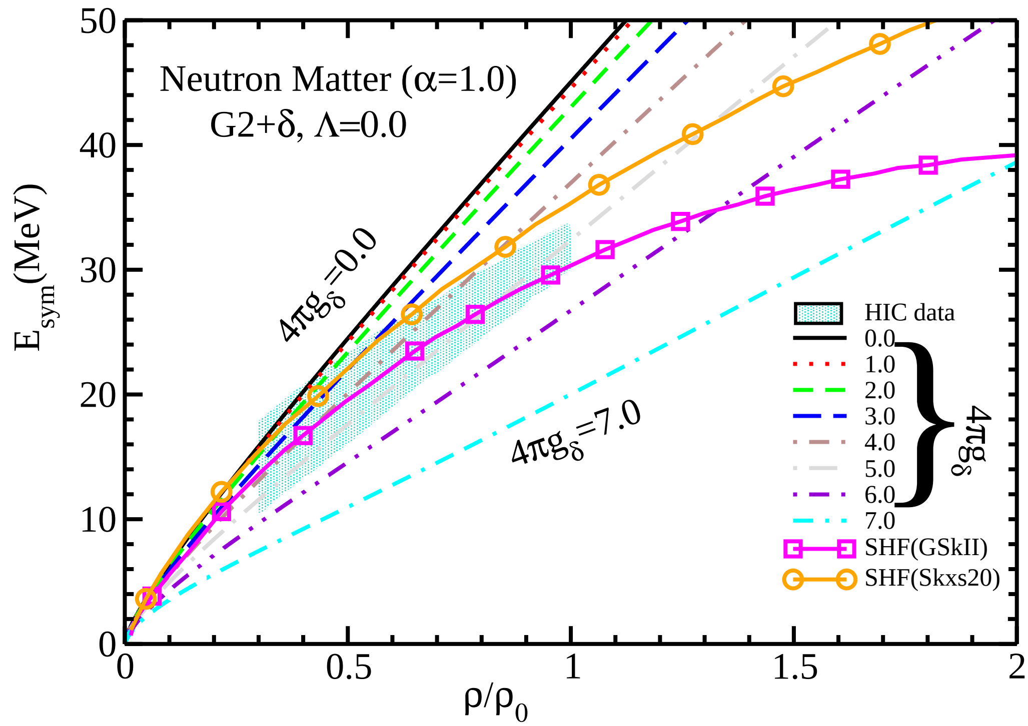

Figure 7.8: Constraints on E_{sym} with its first derivative, i.e., L_{sym} at saturation density for neutron matter. The experimental results of HIC [269], PDR [277, 278] and IAS [279] are given. The theoretical prediction of finite range droplet model (FRDM) [280] and Skyrme parametrization [117] are also given.

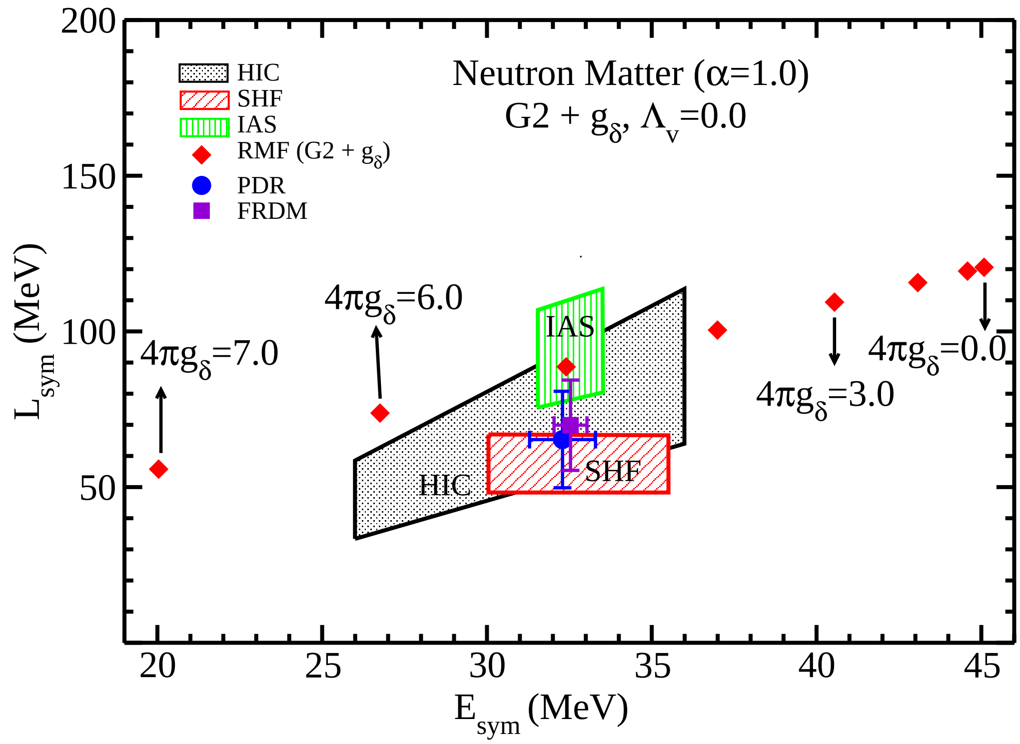

Figure 7.9: The mass and radius of neutron star at different values of g_δ. (a) $M/M_\odot$ with neutron star density (gm/cm^3), (b) $M/M_\odot$ with neutron star radius (km).

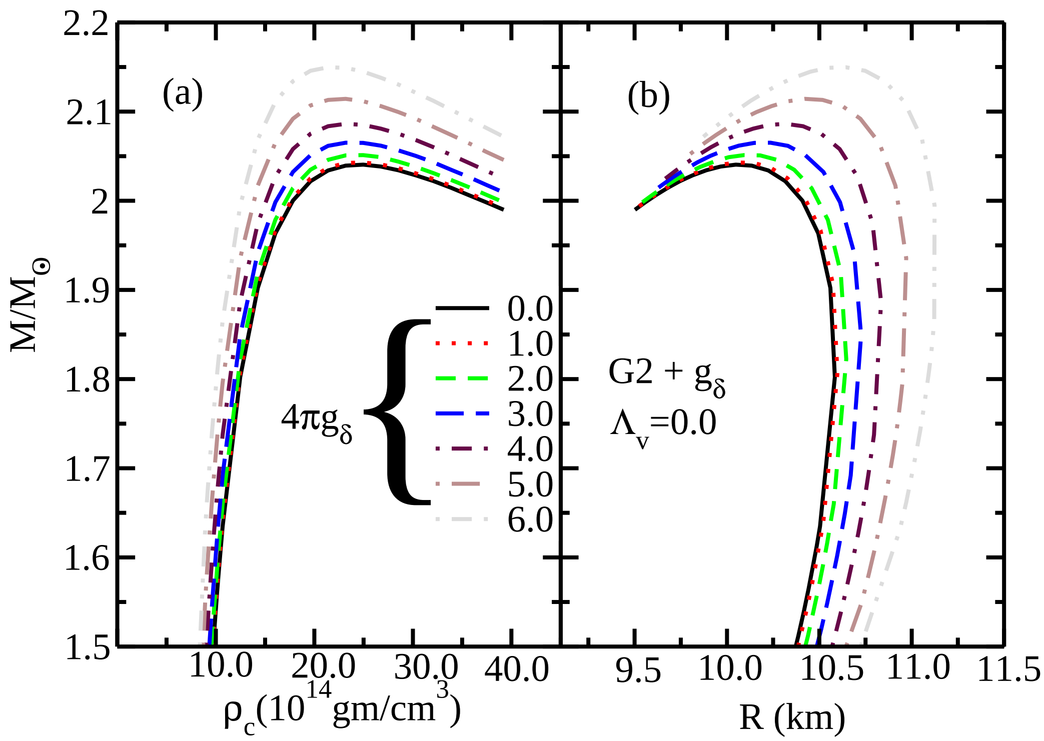

On the right side of the figure, [Fig. 7.9], $M/M_\odot$ is depicted with respect to radius (km), where M is the mass of the star and $M_\odot$ is the solar mass. The g_δ coupling changes the star mass by ∼5.41% and radius by 5.39% with a variation of g_δ from 0 to 6.0. From this observation, we can say that $\delta-$meson is important not only for asymmetry system normal density, but also substantially effective in high density system. If we compare this results with the previous results [268], i.e., with the effects of cross coupling of $\omega - \rho$ on mass and radius of neutron star, the effects are opposite to each other. That means, the star masses decreases with Λ_v, whereas it is increases with g_δ.

7.2.2 Selection of g_δ, g_ρ and Λ_v:

The G2 set is a phenomenological parametrization. All the parameters in this set are adjusted to reproduce some specific experimental data. Therefore, each of the coupling constant contains physics and it is difficult to disentangle the influence of the various physical properties on these parameters. Apart from this, all the parameters depend on the underlying fitting strategy. Thus we can not just add one more parameter like g_δ to study it's effect keeping all the other parameters of G2 fixed. Because the physics described by this g_δ might be included already in the other parameters and leading towards a double counting. Since, both g_δ and g_ρ depends on the isospin symmetry, we expect that, some parts of the effects of g_δ might be taken into account in the parameter g_ρ at the time of fitting the G2 set. Fortunately, in this particular case of g_δ, we expect a connection between the parameters g_δ and g_ρ as both of them carry isospin. In such a situation, there are two possible solutions to this problem (i) the dependence on both g_δ and g_ρ independently. In this case, modify the parameter g_ρ to fit an experimental data which is linked to both g_ρ and g_δ for each new given value of g_δ, such as binding energy or (ii) get a completely new parameter set as it is done for G2 including $\delta-$meson as a degree of freedom from the beginning, i.e., start from an *ab initio* calculations as done in [313].

Here, we study the effect of g_δ on finite and infinite nuclear matter systems adopting the first approach. The combination of g_δ and g_ρ are chosen in such a way that for a given value of g_δ, the combined values of g_δ and g_ρ on top of G2 (with changed g_ρ) reproduce the physical observable of a particular experimental measure. In this case, we have taken the binding energies of ^{48}Ca and ^{208}Pb as the experimental data. These values change from their original prediction of G2 with the addition a given g_δ. To bring back the G2 binding energies of ^{48}Ca and ^{208}Pb, we modified the g_ρ coupling. This is done because of the isospin coupling linked with both g_δ and g_ρ. In this way, we get various combinations of (g_ρ, g_δ) for different given value of g_δ. The combination of g_ρ and g_δ are listed in Table 7.1 which are used in the calculations for both finite nuclei and infinite nuclear matter. It is to be noted that while setting the $g_\delta - g_\rho$ combination, the Λ_v is taken as zero. On the other hand, Λ_v changes on top of the pure G2 parameter set to see the influence of Λ_v for finite nuclei, as the binding energy and proton radius r_p are almost insensitive to Λ_v [307].

Finite Nuclei

In Fig. 7.10(a), we have shown the binding energy difference ΔBE of ^{48}Ca between the two solutions obtained with (g_ρ, g_δ=0) and (g_ρ, g_δ), i.e.

$$\Delta BE = BE(g_\rho, g_\delta = 0) - BE(g_\rho, g_\delta), \tag{7.1}$$

here $BE(g_\rho, g_\delta = 0)$ is the binding energy at $g_\delta = 0$ in the adjusted combination of (g_ρ, g_δ) and $BE(g_\rho, g_\delta)$ is the binding energy with non-zero g_ρ and g_δ combined which reproduce the same binding of pure G2. Thus, the contribution of $\delta-$ meson to the binding energy is obtained from this ΔBE. Similarly, the effect of $\delta-$meson in radius of finite nuclei is seen from:

$$\Delta r = r(g_\rho, g_\delta = 0) - r(g_\rho, g_\delta), \tag{7.2}$$

where $r(g_\rho, g_\delta = 0)$ is the radius at $g_\delta = 0$ in the adjusted (g_ρ, g_δ) and $r(g_\rho, g_\delta)$ is the G2 radius after reshuffling g_ρ and g_δ combination. The Δr with corresponding g_δ for ^{48}Ca are shown in the Fig. 7.10(b). We have adopted the same scheme to estimate the effect of $\delta-$meson on the first and last occupied levels, which are shown in Fig. 7.10(c). It is given as:

$$\Delta\epsilon = \epsilon(g_\rho, g_\delta = 0) - \epsilon(g_\rho, g_\delta), \tag{7.3}$$

where $\epsilon(g_\rho, g_\delta = 0)$ is the single-particle energy at $(g_\rho\ g_\delta = 0)$ combination, g_ρ is not same as G2 set and $\epsilon(g_\rho, g_\delta)$ is energy of the occupied level with different values of g_ρ and g_δ sets.

The effect of Λ_v coupling on ^{48}Ca properties like binding energy, radius and single-particle energy of the first and last occupied levels are shown in the second column of Figure 7.10. Here, we have taken g_δ=0. Following the same procedure of g_δ to evaluate ΔBE, Δr and $\Delta\epsilon$, we estimate the contributions of Λ_v on the physical quantities. The variation of binding energy (ΔBE) with Λ_v can be written as:

$$\Delta BE = BE(G2) - BE(G2 + \Lambda_v), \tag{7.4}$$

with $BE(G2)$ is the binding energy with pure G2 set and $BE(G2 + \Lambda_v)$ is for G2 with additional $\omega - \rho-$ cross coupling. The changes in radius with Λ_v is given by:

$$\Delta r = r(G2) - r(G2 + \Lambda_v), \tag{7.5}$$

where $r(G2)$ is the radius of ^{48}Ca with pure G2 and $r(G2 + \Lambda_v)$ with additional Λ_v on top of pure G2. This results are shown in Fig. 7.10(e). The effect of Λ_v on the first and last filled single-particle levels are given in the Fig. 7.10(f) using:

$$\Delta\epsilon = \epsilon(G2) - \epsilon(G2 + \Lambda_v), \tag{7.6}$$

where ϵ(G2) is the single-particle energy of the first and last occupied levels of ^{48}Ca with original G2 and $\epsilon(G2 + \Lambda_v)$ at various Λ_v values on top of G2 parameter set. Similar to ^{48}Ca, we have repeated the calculations for ^{208}Pb in Figure 7.11 to study the effect of g_δ and Λ_v. We have followed exactly the same method as that of ^{48}Ca and calculated the variation in binding energy, radii and single-particle levels. We obtained almost similar results as that of Fig. 7.10.

From the figures (Fig. 7.10 and Fig. 7.11), it is evident that the binding energy, radii and single particle levels $\epsilon_{n,p}$ affected drastically with g_δ contrary to the effect of Λ_v. A careful inspection shows a slight decrease of r_n with the increase of Λ_v consistent with the analysis of [307]. Again, it is found that the binding energy increases with increasing of the coupling strength upto $g_\delta \sim 1.1$ and no convergence solution available beyond this value. Similar to the g_δ limit, there is limit for $\Lambda_v \sim 0.16$ also, beyond which no solution exist. From the anatomy of g_δ on r_n and r_p (or Δr), we find their opposite trend in size. That means the value of r_n decreases and r_p increases with g_δ for both ^{48}Ca and ^{208}Pb. This interesting results may help us to settle the charge radius anomaly of ^{40}Ca and ^{48}Ca.

In Figs. 7.10(c) and 7.10(f), we have shown the change in single-particle energy $\Delta\epsilon_{n,p}$ of the first ($1s^{n,p}$) and last ($1f^n$ and $2s^p$) filled orbitals for ^{48}Ca as a function of g_δ and

Figure 7.10: Binding energy (BE), root mean square radius and first ($1s^{n,p}$) and last ($1f^n$, $2s^p$) occupied orbits for ^{48}Ca using various (g_ρ, g_δ, Λ_v) combination of Table 7.1.

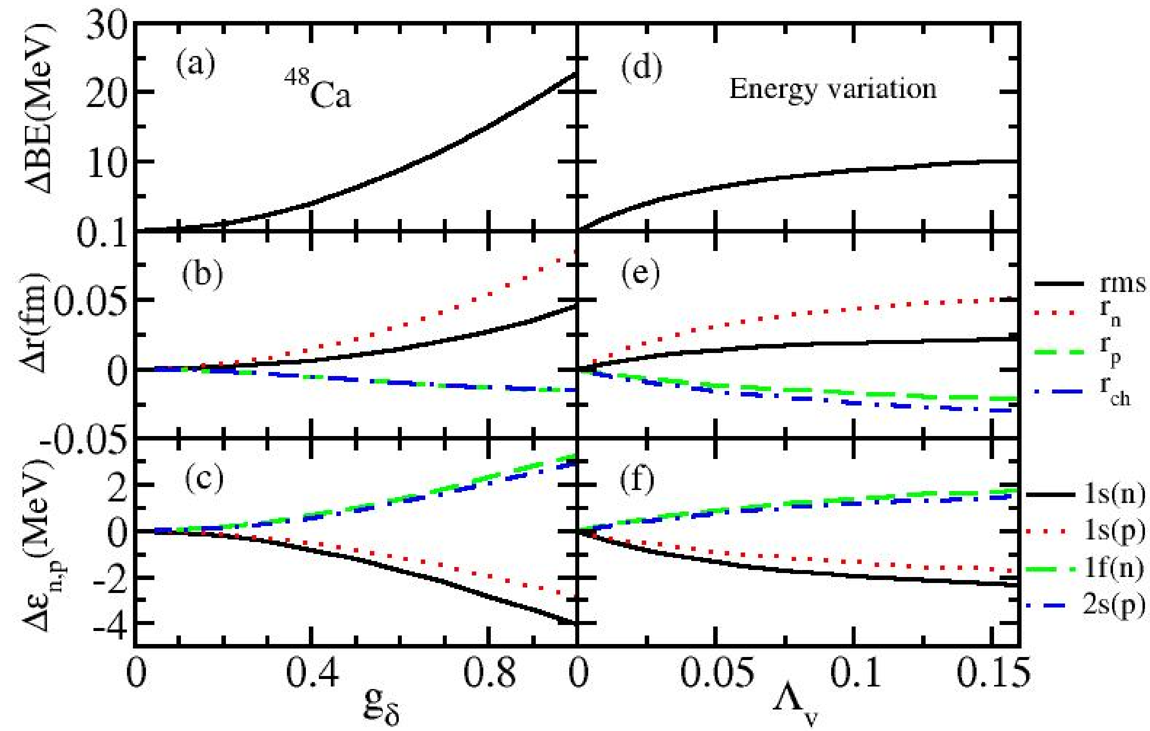

Λ_v, respectively. The effect of Λ_v is marginal, i.e., almost negligible on $\epsilon_{n,p}$ orbitals which is given in Fig. 7.10(f). However, this is significance with the increasing value of g_δ. We get similar trend for ^{208}Pb also, which is shown in Fig. 7.11(c). In both the representative cases, we notice orbital shifting only for the last filled levels (for $g_\delta \geq 1.0$, not shown in the figure). The change in nucleon density $\Delta\rho$ distribution (proton ρ_p and neutron ρ_n) and spin orbit interaction potential ΔU_{so} for finite nuclei are shown in Figs. 7.12 and 7.13. The calculations are done with one set of (g_ρ, g_δ) for checking the effect of g_δ in finite nuclei, and shown in the Figs. 7.12(a) and 7.12(b) for ^{48}Ca. Here, we have taken g_δ=1.0 and corresponding modified g_ρ=1.3634 for calculating the $\Delta\rho$ [ρ(g_ρ=1.3634, g_δ=0) - ρ(g_ρ=1.3634, g_δ=1.0)] and ΔU_{so}[U_{so}(g_ρ=1.3634, g_δ=0) - U_{so}(g_ρ=1.3634, g_δ=1.0)]. To see the effectiveness of Λ_v on nucleon distribution and spin orbit interaction potential, we have estimated the $\Delta\rho$[ρ(G2) - ρ(G2 + Λ_v=0.16)] and ΔU_{so}[U_{so}(G2) - U_{so}(G2 + Λ_v=0.16)] for both neutron

Figure 7.11: Same as Fig. 7.10 for ^{208}Pb.

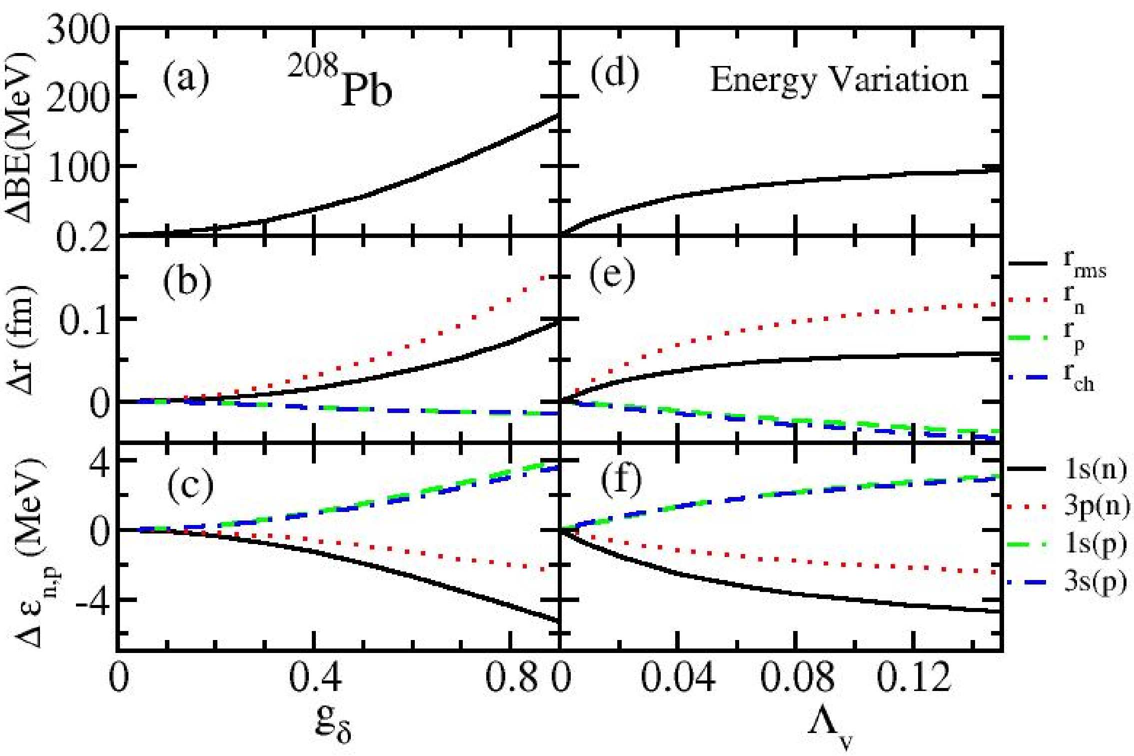

Figure 7.12: The neutron and proton density with radial coordinate $r(fm)$ at different combination of (g_ρ, g_δ) in (a) and with Λ_v in (c). The variation of spin-orbit potential for proton and neutron are shown in (b) and (d) by keeping the same g_δ and Λ_v as (a) and (c) respectively.

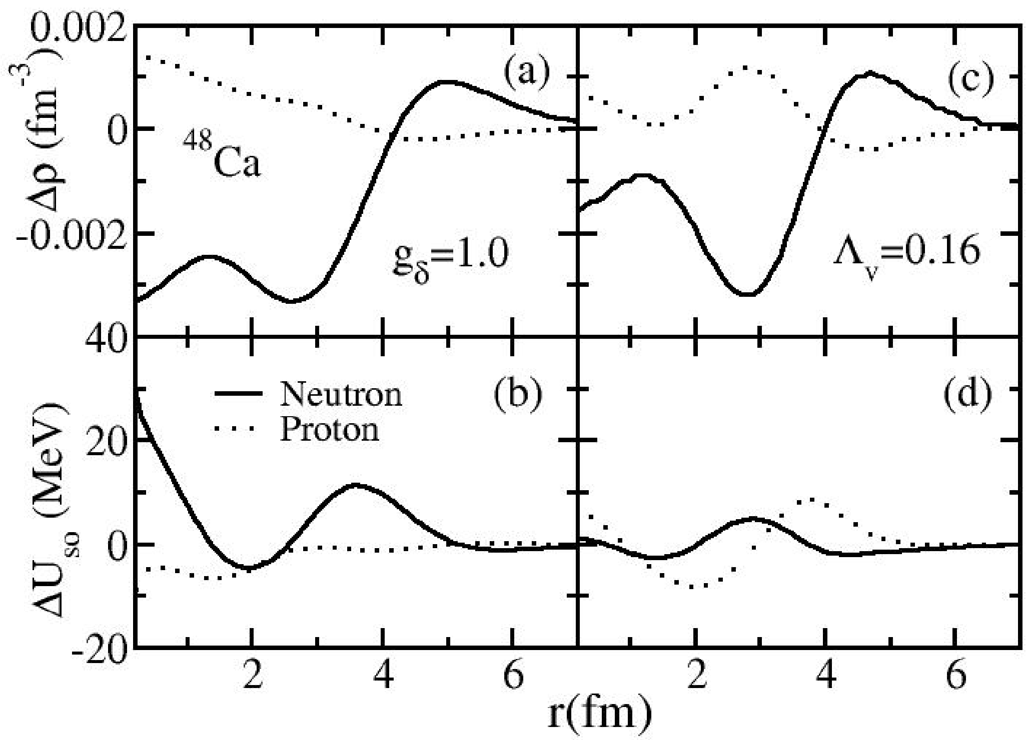

and proton, respectively. The results are shown in figures 7.12(c) and 7.12(d). Similarly, we have given these observables for ^{208}Pb in Fig. 7.13. It is clear from this analysis that the coupling strengths of $\delta-$meson and the isoscalar-vector and isovector-vector cross coupling are quite influential for the density and spin-orbit interaction. This effect is mostly confined to the central and intermediate region of the nucleus.

Nuclear Matter

In Fig. 7.14(a), the effective masses of proton and neutron are given as a function of g_δ. As we have mentioned, $\delta-$meson is responsible for the splitting of effective masses (Eqns. (16) and (17)), this splitting increases continuously with coupling strength g_δ. In Fig. 7.14,

Figure 7.13: Same as Fig. 7.12 for ^{208}Pb.

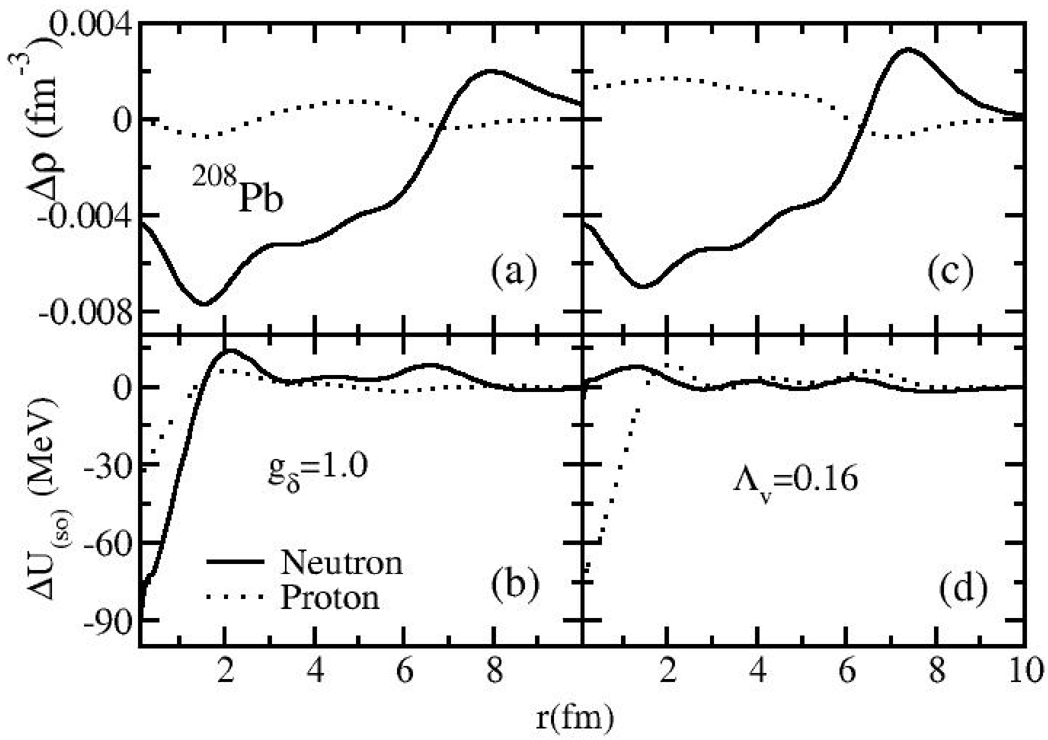

Figure 7.14: Variation of nucleonic effective masses, binding energy per particle (BE/A) and pressure as a function of g_δ on saturation density of G2 parameter set for nuclear matter.

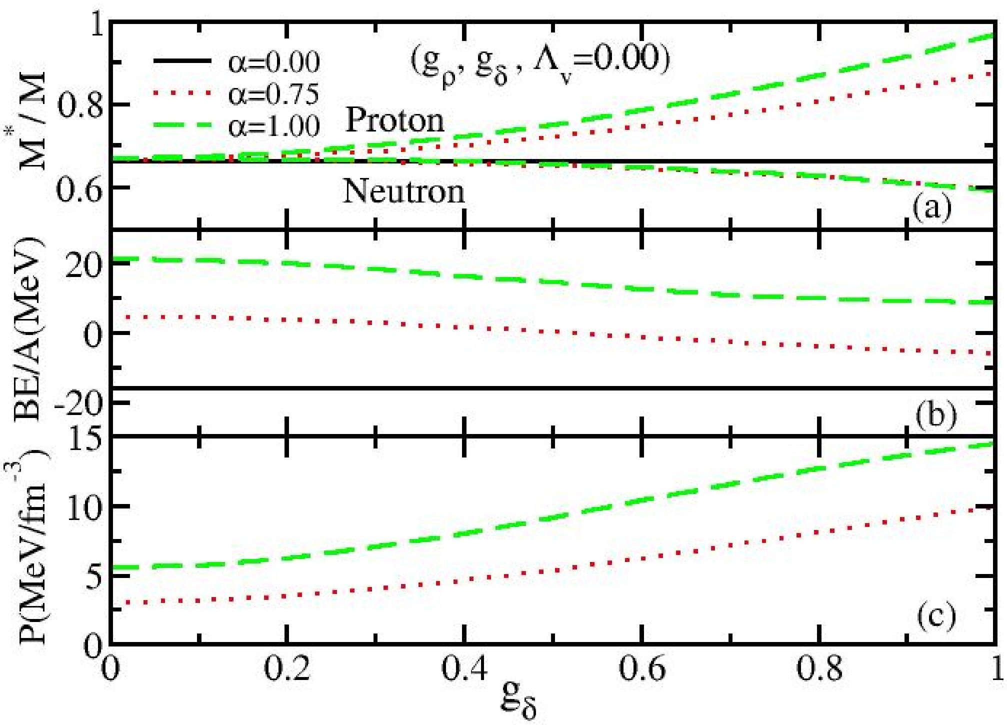

the splitting is shown for few representative cases at α=0.0, 0.75 and 1.0. The solid line is for α=0.0 and α=0.75, 1.0 are shown by dotted and dashed line, respectively. From the figure, it is clear that the effective mass is unaffected for symmetric matter. The proton effective mass M_p^* is above the reference line with $\alpha = 0$ and the neutron effective mass always lies below it. The effect of g_δ on binding energy per nucleon is shown in Fig. 7.14(b) and pressure in Fig. 7.14(c). One can easily see the effect of $\delta-$ meson interaction on the energy density and pressure of the nuclear system. The energy density and pressure show opposite trend to each other with the increase of g_δ.

Energy and Pressure Density

In Fig. 7.15, the calculated BE/A and $\mathcal{P}$ for pure neutron matter ($\alpha = 1.0$) with baryonic density for different combination of g_ρ and g_δ values which is shown in the first column in Table 7.1.

It is seen from Fig. 7.15(a), the binding increases with g_δ in the lower density region and in higher density region, the binding energy curve for finite g_δ crosses the curve of g_δ=0.0. The EOS with $\delta-$meson is stiffer than the one with pure G2 set at higher density. As a result, one will get a heavier mass of the neutrons star, which suited with the present experimental finding [96]. For comparing the data at lower density (dilute system, $0 < \rho/\rho_0 <$ 0.16) the zoomed version of the region is shown as an inset Fig. 7.15(c) inside Fig. 7.15(a). From the zoomed inset portion, it is clearly seen that the curves with various combination of g_ρ and g_δ at $\alpha = 1.0$ (pure neutron matter) deviate from other theoretical predictions, such as Baldo-Maieron [308], DBHF [309], Friedman [310], auxiliary-field diffusion Monte Carlo (AFDMC) [311] and Skyrme interaction [117]. Similarly, the pressure for different sets of (g_ρ, g_δ) are given in Fig. 7.15(b). At high density we can easily see that the curve becomes more stiffer with the coupling strength g_δ. The experimental constraint of equation of state obtained from heavy ion flow data for both stiff and soft EOS is also displayed for comparison in the region $2 < \rho/\rho_0 <$ 4.6 [312]. Our results match with the stiff EOS data of Ref. [312].

Symmetry Energy

The results for E_{sym} are shown in Fig. 7.16 with experimental heavy ion collision (HIC) data [269] and other theoretical predictions of non-relativistic Skyrme-Hartree-Fock model.

Figure 7.15: Energy per particle and pressure with respect to baryon density at various combination of g_δ of Table 7.1.

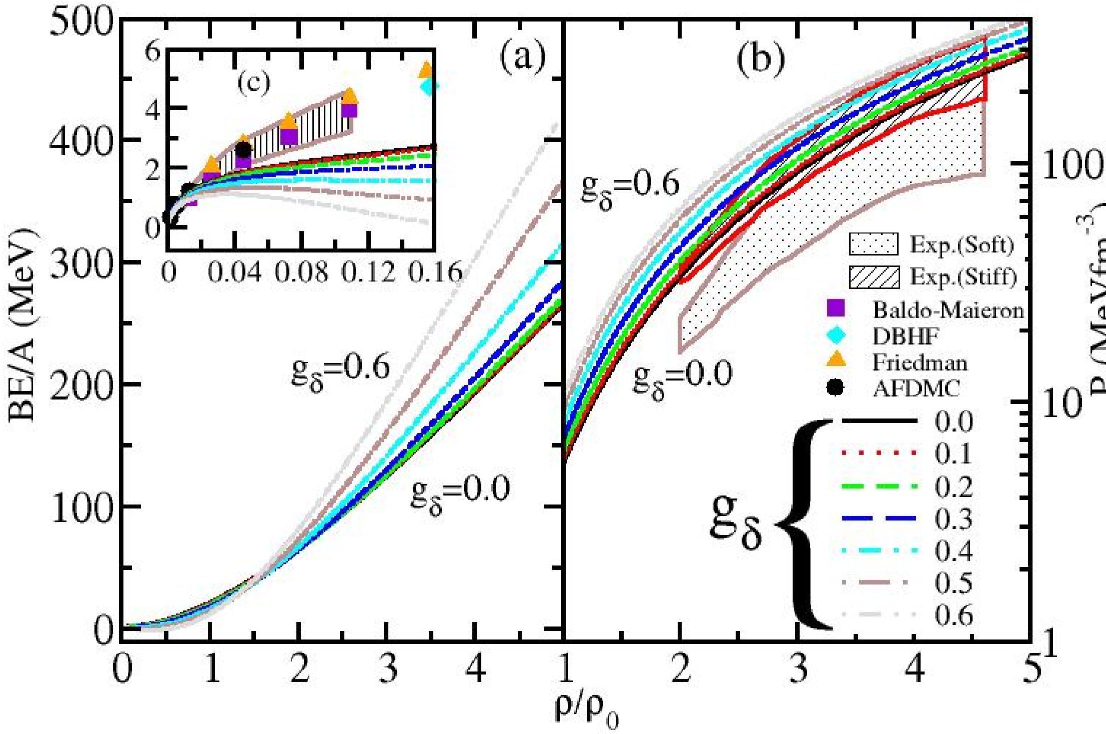

The calculation is done for symmetric nuclear matter with different values of g_δ, which are compared with two selective force parameter sets GSkII [270] and Skxs20 [275]. Here in our calculations, as usual $\Lambda_v = 0$ to see the effect of $\delta-$meson coupling on E_{sym}. In figure Fig. 7.16, shaded region represent the HIC data [269] within $0.3 < \rho/\rho_0 < 1.0$ region and the symbols square and circle represent the SHF results for GSkII and Skxs20 respectively. Analyzing Fig. 7.16, E_{sym} of G2 matches with the shaded region in low density region, however as the density increases, the value of E_{sym} moves away. Again, the symmetry energy becomes softer by increasing the value of coupling strength g_δ. For higher value of g_δ, again the curve moves far from the empirical shaded area. In this way, we can fix the limiting constraint on coupling strength of $\delta-$ meson and nucleon. Analysing the results of EOS with the DD-ME2 and DD-MEδ parametrizations [89], we find that DD-ME2 overestimates the data, while DD-MEδ matches well. On the other hand the symmetry energy with these sets coincides upto $2\rho_0$ of nuclear matter density. From this result, we can not isolate the contribution of $\delta-$meson on E_{sym} or EOS. Because, the goal of the two parametrizations is to reproduce the empirical data. However, in our present case, our aim is to entangle the contribution of $\delta-$meson with and without g_δ coupling keeping all other parameters intact.

In Fig. 7.17, we have given the symmetry energy with its first derivative at saturation density with different values of coupling strength staring from $g_\delta = 0.0 - 0.6$. The variation of E_{sym}, L_{sym} and K_{sym} with g_δ are listed in Table 7.1. The variation in symmetry energy takes place from 36.48 to -0.89 MeV, L_{sym} from 100.91 to 28.71 MeV and K_{sym} from -7.57 to 322.51 MeV at saturation density corresponding to $0.0 \leq g_\delta \leq 1.0$. The pure G2 set (0.755, 0.0) is not sufficient to predict this constrained on E_{sym} and L_{sym}. It is suggestive to introduce the $\delta-$ meson as an extra degree of freedom into the model to bring the data within the prediction of experimental and other theoretical constraints. From this investigation, one can see that the permissible values of E_{sym}, L_{sym} and K_{sym} do not obtain by all the combinations of g_ρ and g_δ. Thus, it is needed to choose a suitable set of g_ρ and g_δ for proper parametrization both for finite nuclei or infinite nuclear matter.

Neutron Star

The results of mass and radius with various $\delta-$meson coupling strength g_δ is shown in Fig. 7.18. In left panel, the neutron star mass with density (gm/cm^3) is given, where we can

Figure 7.16: Symmetry energy E_{sym} (MeV) of symmetric nuclear matter with respect to density by taking different value of g_δ sets. The heavy ion collision (HIC) experimental data [269] (shaded region) and non-relativistic Skyrme GSkII [270], and Skxs20 [275] predictions are also given. Λ_v=0.0 is taken.

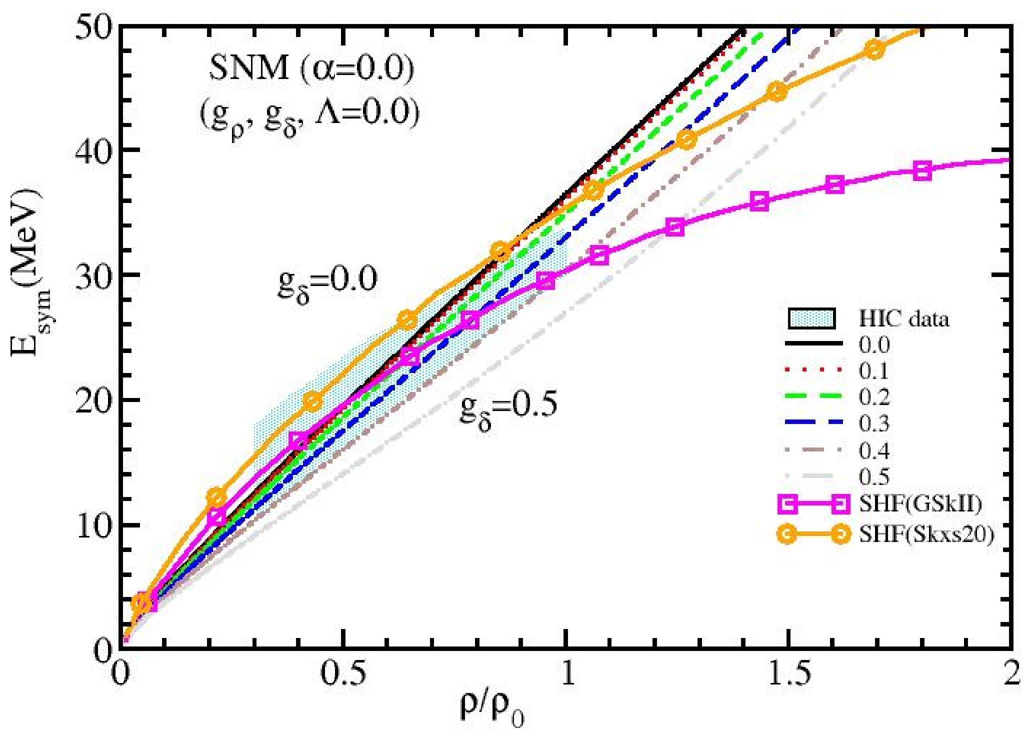

Figure 7.17: Constraints on E_{sym} with its first derivative, i.e., L_{sym} at saturation density for symmetric nuclear matter. The experimental results of HIC [269], PDR [277, 278] and IAS [279] are given. The theoretical prediction of finite range droplet model (FRDM) [280] and Skyrme parametrization [117] are also given.

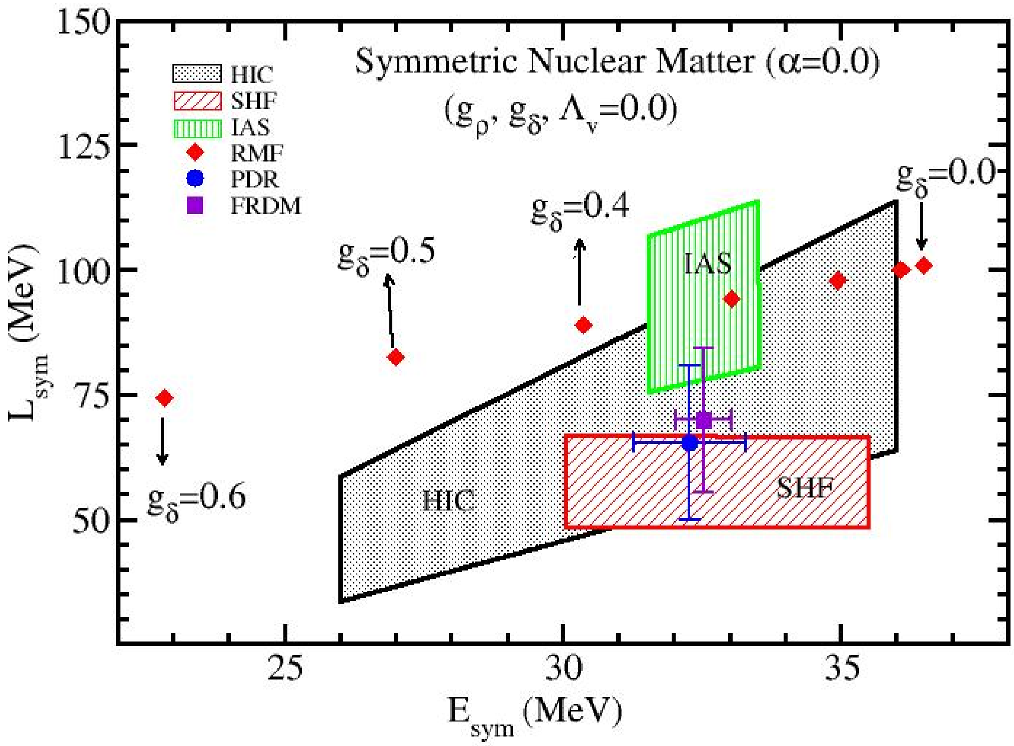

Figure 7.18: The mass and radius of neutron star at different values of g_δ. (a) $M/M_\odot$ with neutron star density (gm/cm^3), (b) $M/M_\odot$ with neutron star radius (km).

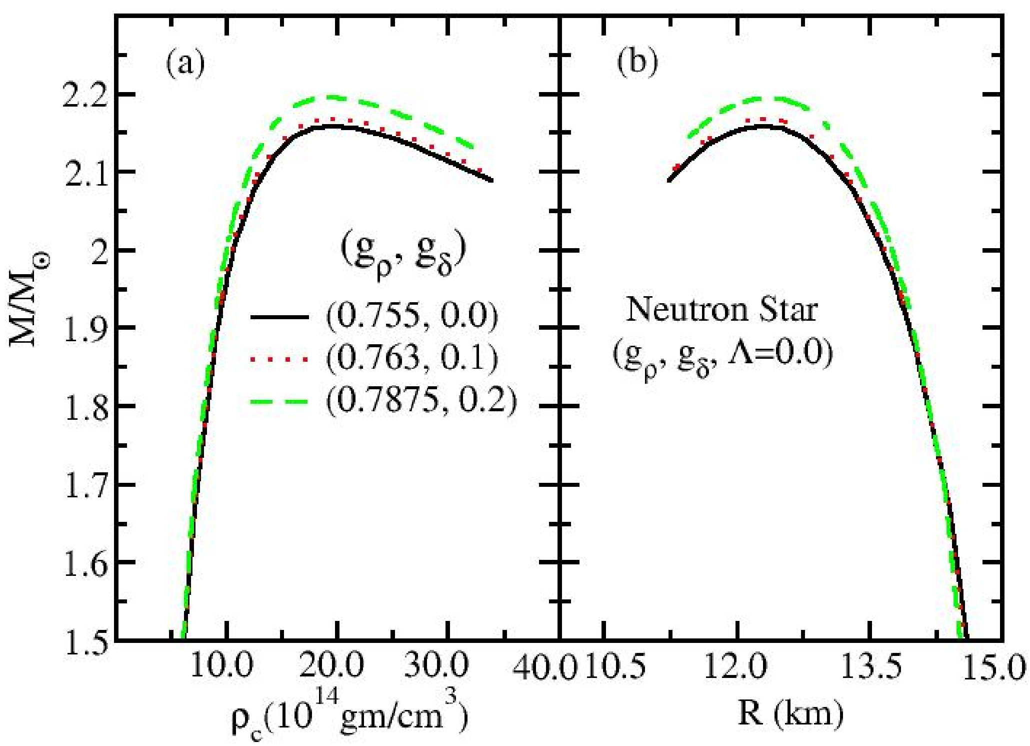

Table 7.1: The symmetry energy E_{sym} (MeV), slope co-efficient L_{sym} (MeV) and K_{sym} (MeV) at different sets of (g_ρ, g_δ).

(g_ρ, g_δ)	E_{sym}	L_{sym}	K_{sym}
(0.755, 0.0)	36.48	100.91	-7.57
(0.763, 0.1)	36.08	100.11	-4.25
(0.7875, 0.2)	34.94	97.88	5.68
(0.827, 0.3)	33.05	94.21	22.21
(0.879, 0.4)	30.38	89.01	45.37
(0.9423, 0.5)	26.99	82.45	75.10
(1.0142, 0.6)	22.84	74.40	111.45
(1.0937, 0.7)	17.98	65.02	154.36
(1.179, 0.8)	12.39	54.24	203.85
(1.2691, 0.9)	6.09	42.10	259.91
(1.3634, 1.0)	-0.89	28.71	322.51

see the effect of the newly introduced extra degree of freedom $\delta-$meson into the system. On the right side of the figure, [Fig. 7.18], $M/M_\odot$ is depicted with respect to radius (km), where M is the mass of the star and $M_\odot$ is the solar mass. Here, we used the different set of g_ρ and g_δ coupling constants for calculating the star properties. From this observation, we can say that $\delta-$meson is important not only for asymmetry system at normal density, but also substantially effective in high density system also.

7.3 Summary and Conclusions

In summary, we rigorously discussed the effects of cross coupling of $\omega-\rho-$mesons in finite nuclei on top of the pure G2 parameter set. The variation of binding energy, rms radii and energy levels of protons and neutrons are analyzed with increasing values of Λ_v. The change in neutron distribution radius r_n with Λ_v is found to be substantial compared to the less effectiveness of binding energy and proton distribution radius for the two representative nuclei ^{48}Ca and ^{208}Pb. Thus, to fix the neutrons distribution radius depending on the outcome of PREX experimental [304] result, the inclusion of Λ_v coupling strength is crucial. As it is discussed widely, the role of cross coupling of $\omega-\rho-$mesons in the nuclear matter system is important.

We emphasized strongly the importance of the effect of the extra degree of freedom, i.e., $\delta-$meson coupling into the standard RMF or E-RMF model, where, generally it was ignored. We have seen the effect of this coupling strength of $\delta-$meson in finite and infinite matter which is substantial and very different in nature. It may be extremely helpful to fix various experimental constraints. For example, with the help of g_δ, it is possible to modify the binding energy, charge radius and flipping of the orbits in asymmetry finite nuclei systems. The nuclear equation of state can be made stiffer with inclusion of $\delta-$meson coupling. On the other hand, softening of symmetry energy is also possible with the help of this extra degree of freedom. In compact system, it is possible to fix the limiting values of g_δ and Λ_v by testing the effect on available constraints on symmetry energy and its first derivative with respect to the matter density. This coupling may be extremely useful to fix the mass and radius of neutron star keeping in view of the recent observation [96].

Chapter 8

Gravitational wave strain amplitude from rotating compact neutron star

8.1 Introduction

About 96 percent mass-energy of the Universe is chargeless [314]. Thus, unlike electromagnetic radiation, it is difficult to get information from this huge part of cosmos either directly or indirectly. The only possible way to study this neutral part of the Universe is the gravitational wave (GW) radiation. The main disadvantage of the gravitational radiation is its production in laboratories. One has to depend for its sources on extra-celestial body which has a large mass with a compact dimension in size. In this context, neutron star could be a probable candidate to generate the gravitational wave radiation and its possible detection on earth. A rotating deformed neutron star emits gravitational waves. Therefore, it is very important to discuss the upper limit of GW amplitude, rotational frequency ν_r, quadrupole moment Φ_{22} and ellipticity ϵ of a neutron star predicted by various theoretical models and will open up a door for the experimental facilities to arrange their detectors accordingly to detect the gravitational amplitude [100, 315].

The recently measured static mass of the neutron star (NS) [96] is quite massive than the earlier measured mass from the neutron star pulsar PSR 1913+16 ($M = 1.144 M_\odot$) [316]. Those equation of states (EOS) give the mass of Taylor et al. [316] fails to reproduce the maximum mass of $(1.97 \pm 0.04) M_\odot$ [96]. To get a larger mass, one needs a stiff EOS, which again oppose the softer EOS of kaon production [317, 318]. To make such a model in the same footing, extra interactions are needed as it is done in G1 and G2 parametrizations [142, 143]. In this work, we have used 20 different force parameters for both non-relativistic Skyrme and relativistic mean field (RMF) equation of states (EOS) to calculate the gravitational wave strain amplitude of rotating neutron stars. The detection of GW amplitude has the following implications:

- It will verify the General Theory of Relativity.
- The zero mass of the graviton with a speed of velocity of light will be verified.

The general expression for the energy and pressure density for asymmetric nuclear matter (ANM) including with $\beta-$equilibrium condition for neutron star equation of states as a function of number density ρ can be found in Refs. [117, 118, 319]. The 13 Skyrme parameter sets used in the calculations are SGII, SkM*, RATP, SLy23a, SLy23b, SLy4, SLy5, SkT1, SkT2, KDE0v1, LNS, NRAPR, SkMP [100, 117, 319] and the 7 RMF sets are G2, G1, NL3, TM1, FSU, L1 and SH [100, 142, 143]. These all parameters along with their saturation properties are given in Table 8.1.

8.2 Formalism

For neutron star, the neutron chemical potential exceeds the combined masses of the proton and electron. Therefore, asymmetric matter with an admixture of electrons rather than pure neutron matter, is a more likely composition. The concentrations of neutron (n), proton (p) and electron (e) can be determined from the condition of $\beta-$equilibrium $n \leftrightarrow p + e + \bar{\nu}$ and from charge neutrality, assuming that neutrinos ν are not degenerated. Imposing these conditions in the expressions of $\mathcal{E}$ and $\mathcal{P}$, we evaluate $\mathcal{E}$ and $\mathcal{P}$ as functions of density. To calculate the star structure, we use the Tolman-Oppenheimer-Volkoff (TOV) equations for a relativistic spherical and static star composed of a perfect fluid (derived from Einstein's equations of General Theory of Relativity [99]). The pressure and energy densities are the input ingredients. The TOV equation is given by [99]:

$$\frac{d\mathcal{P}}{dr} = -\frac{1}{r}\frac{[\mathcal{E}+\mathcal{P}]\,[M+4\pi r^3\mathcal{P}]}{(r-2M)}, \tag{8.1}$$

$$\frac{dM}{dr} = 4\pi r^2\mathcal{E}, \tag{8.2}$$

with $M(r)$ as the enclosed gravitational mass. We have used $c = 1, G = 1$, the velocity of light and universal gravitational constant, respectively. Given $\mathcal{P}$ and $\mathcal{E}$, these equations can be integrated from the origin as an initial value problem for a given choice of central energy density. The value of r $(= R)$, where the pressure vanishes defines the surface of the star [99].

Another realistic approximation, when neutron star is rotating with static, axial symmetric, space-time, the time translational invariant and axial-rotational invariant metric in spherical polar coordinate (t, r, θ, ϕ) can be written as:

$$\begin{aligned} ds^2 &= -e^{2\nu}dt^2 + e^{2\alpha}(dr^2 + r^2 d\theta^2) \\ &\quad + e^{2\beta}r^2 sin^2\theta(d\phi - \omega dt)^2, \end{aligned} \tag{8.3}$$

where the metric functions ν, α, β, ω depend only on r and θ. For a perfect fluid, the energy momentum tensor can be given by:

$$T^{\mu\nu} = Pg^{\mu\nu} + (\mathcal{P} + \mathcal{E})u^\mu u^\nu, \tag{8.4}$$

with the four-velocity

$$u^\mu = \frac{e^{-\nu}}{\sqrt{1 - v^2}}(1, 0, 0, \Omega), \tag{8.5}$$

here

$$v = (\Omega - \omega)r\ sin\ \theta e^{\beta - \nu}, \tag{8.6}$$

is the proper velocity relative to an observer with zero angular velocity and Ω is the angular velocity of the star measured from infinity. Now, we can compute the Einstein field equation given by

$$R_{\mu\nu} - \frac{1}{2}g_{\mu\nu}R = 8\pi T_{\mu\nu}, \tag{8.7}$$

where $R_{\mu\nu}$ is Ricci tensor and R is the scalar curvature. From this, we can solve the equation of motion for metric function:

$$\Delta\left[\rho e^{\zeta}\right] = S_\rho(r, \mu), \tag{8.8}$$

$$\left(\Delta + \frac{1}{r}\frac{\partial}{\partial r} - \frac{1}{r^2}\mu\frac{\partial}{\partial r}\right)\gamma e^{\zeta} = S_\gamma(r, \mu), \tag{8.9}$$

$$\left(\Delta + \frac{2}{r}\frac{\partial}{\partial r} - \frac{2}{r^2}\mu\frac{\partial}{\partial r}\right)\omega e^{\frac{\gamma - 2\rho}{2}} = S_\omega(r, \mu), \tag{8.10}$$

where $\gamma = \beta + v$, $\rho = v - \beta$ and μ =cosθ. The right hand side of the equations contains the source terms. One can find more details about these equations in Ref. [320]. We can put the limit on the maximum rotation i.e. Kepler frequency Ω_k, by the onset of mass shedding from the equator of the star. The final expression for Ω_k, in general relativistic formalism is given as:

$$\Omega_K = \omega + \frac{\omega'}{2\psi'} + e^{v-\beta}\left[\frac{1}{R^2}\frac{v'}{\psi'} + \left(\frac{e^{\beta-v}\omega'}{2\psi'}\right)^2\right]^{\frac{1}{2}}, \tag{8.11}$$

where $\psi = \beta' + \frac{1}{R}$ and the prime denotes the differentiation with respect to the radial coordinate. For the calculation of rotational neutron star properties like mass, radius, rotational frequency, we used the well established rotational neutron star (RNS) code of Stergioulas [321, 322].

8.2.1 Properties of Rotating Neutron Star

We have calculated the maximum mass and radius of static and rotating neutron star by using the well established RNS code. For this, we need only energy and pressure density which will be provided by non-relativistic and relativistic models of equation of state. Now, our aim is to calculate the quadrupole moment in maximum projection state $m = 2$ for neutron star by using a chemically detailed model for the crust [323]. The relation of quadrupole moment with maximum mass M $(M_\odot)$ and radius R (km) is given as:

$$\begin{aligned}\Phi_{22} &= 2.4 \times 10^{38} gcm^2 \left(\frac{\sigma_{max}}{10^{-2}}\right)\left(\frac{R}{10km}\right)^{6.26} \\ &\times \left(\frac{1.4M_\odot}{M}\right)^{1.2},\end{aligned} \tag{8.12}$$

where σ_{max} is called breaking strain of the crust. In the calculations, we have taken its two possible values, i.e. 10^{-2} and 10^{-3}.

The quadrupole moment [Eqn. (8.12)] and ellipticity of the neutron star is connected to each other by a simple relation [323]:

$$\epsilon = \sqrt{\frac{8\pi}{15}}\frac{\Phi_{22}}{I_{zz}}, \tag{8.13}$$

where the z axis is the rotation axis and I_{zz} is the moment of inertia along the z-axis and for conventional neutron star, it is given as [324]:

$$I_{zz} = 9.2 \times 10^{44} gcm^2 \left(\frac{M}{1.4M_\odot}\right)\left(\frac{R}{10km}\right)^2 \times \left[1 + 0.7\left(\frac{M}{1.4M_\odot}\right)\left(\frac{10km}{R}\right)\right]. \tag{8.14}$$

For each (non-relativistic and relativistic) parameter sets, we can calculate the maximum mass and radius of the neutron star and then other observables like quadrupole, ellipticity and moment of inertia. The maximum rotational frequency ν_{max} of the stable rotationary neutron star can be given by the simple relation [118]:

$$\nu_{max} = 1.22 \times 10^3 \left(\frac{M}{M_\odot}\right)^{1/2} \left(\frac{R}{10\text{km}}\right)^{-3/2}, \tag{8.15}$$

The gravitational wave has two polarization states ($h_+, h_\times$). The h_+ polarization component of a plane gravitational wave with frequency f propagating in z-direction has the form $h_+(z = 0, t) = h_0 e^{2\pi ift}$, where h_0 is gravitational wave strain amplitude and t is time coordinate. The cross polarization $h_\times$ has its principle axes rotated 45 degrees relative to the plus polarization, which is a consequence of the spin-2 nature of the gravitational field. We use eqns. (8.12 - 8.15) to calculate the gravitational wave strain amplitude h_0 which is given by [325]:

$$h_0 = \frac{16\pi^2 G}{c^4} \frac{\epsilon I_{zz} f^2}{r}, \tag{8.16}$$

with r is the distance of neutron star from the earth [326]. After getting the mass and radius, we have calculated other properties like Φ_{22}, ϵ, I and h_0 of rotating neutron star.

Table 8.1: The Skyrme and RMF force parameters and their nuclear matter properties, like BE/A (MeV), compressibility K_0 (MeV), nucleon effective mass ratio M*/M, symmetry energy E_{sym} (MeV), L_{sym} (MeV), K_{sym} (MeV) at saturation density ρ_0.

Skyrme effective interaction																
	Coupling Constants									Nuclear Saturation Properties						
Parameter	t_0	t_1	t_2	t_3	x_0	x_1	x_2	x_3	σ	ρ_0	M^*/M	BE/A	K_0	E_{sym}	L_{sym}	K_{sym}
SGII	-2645.0	340.0	-41.9	15595.0	0.09	-0.06	1.43	0.06	0.17	0.16	0.79	-15.6	214.7	26.8	37.6	-145.9
SkM*	-2645.0	410.0	-135.0	15595.0	0.09	0.00	0.00	0.00	0.17	0.16	0.79	-15.8	216.6	30.0	45.8	-155.9
SkMP	-2372.2	503.6	57.3	12585.3	-0.16	-0.40	-2.96	-0.27	0.17	0.16	0.65	-15.6	230.9	29.9	70.3	-49.8
RATP	-2160.0	513.0	121.0	11600.0	0.42	-0.36	-2.29	0.59	0.20	0.16	0.67	-16.1	239.5	29.3	32.4	-191.2
SLy23a	-2490.2	489.5	-566.6	13803.0	1.13	-0.84	-1.00	1.92	0.17	0.16	0.70	-16.0	229.9	32.0	44.3	-98.2
SLy23b	-2488.9	486.8	-546.4	13777.0	0.83	-0.34	-1.00	1.35	0.17	0.16	0.69	-16.0	229.9	32.0	46.0	-119.7
SLy4	-2488.9	486.8	-546.4	13777.0	0.83	-0.34	-1.00	1.35	0.17	0.16	0.69	-16.0	229.9	32.0	45.9	-119.7
SLy5	-2483.5	484.2	-556.7	13757.0	0.78	-0.32	-1.00	1.26	0.17	0.16	0.70	-16.0	229.9	32.0	48.2	-112.8
SkT1	-1794.0	298.0	-298.0	12812.6	0.15	-0.50	-0.50	0.09	0.33	0.16	1.00	-16.0	236.2	32.0	56.2	-134.8
SkT2	-1791.6	300.0	-300.0	12792.0	0.15	-0.50	-0.50	0.09	0.33	0.16	1.00	-15.9	235.7	32.0	56.2	-134.7
KDE0v1	-2553.1	411.7	-419.9	14603.6	0.65	-0.35	-0.93	0.95	0.17	0.17	0.74	-16.2	227.5	34.6	54.7	-127.1
LNS	-2485.0	266.7	-337.1	14588.2	0.06	0.66	-0.96	-0.03	0.17	0.18	0.83	-15.3	210.8	33.4	61.5	-127.4
NRAPR	-2719.7	417.6	-66.7	15042.0	0.16	-0.05	0.03	0.14	0.14	0.16	0.69	-15.9	225.7	32.8	59.6	-123.3

Relativistic Mean field interaction																	
	Coupling Constants										Nuclear Saturation Properties						
Parameter	g_σ	g_ω	g_ρ	$k3$	$k4$	ζ_0	η_1	η_2	η_r	Λ_v	ρ_0	M^*/M	BE/A	K_0	E_{sym}	L_{sym}	K_{sym}
G2	0.84	1.02	0.76	3.25	0.63	2.64	0.65	0.11	0.39	0.00	0.15	0.66	-16.1	214.7	36.4	100.7	-7.4
G1	0.79	0.97	0.70	2.21	-10.09	3.53	0.07	-0.96	-0.27	0.00	0.15	0.60	-16.2	215.0	37.9	118.6	91.7
NL3	0.81	1.02	0.71	1.47	-5.67	0.00	0.00	0.00	0.00	0.00	0.15	0.60	-16.3	271.8	37.4	118.9	103.4
TM1	0.80	1.00	0.74	1.02	0.12	2.69	0.00	0.00	0.00	0.00	0.15	0.63	-16.3	281.1	36.9	110.6	33.8
FSU	0.84	1.14	0.94	0.62	9.75	12.27	0.00	0.00	0.00	0.03	0.15	0.61	-16.3	230.0	32.6	60.4	-50.5
L1	0.76	0.93	0.00	0.00	0.00	0.00	0.00	0.00	0.00	0.00	0.19	0.56	-15.8	546.6	22.1	74.6	73.6
SH	0.83	1.10	0.64	0.00	0.00	0.00	0.00	0.00	0.00	0.00	0.15	0.54	-15.8	545.0	35.0	115.6	92.8

8.3 Results and Discussions

The parameters are fitted to the saturation properties of symmetric nuclear matter like binding energy per nucleon (BE/A), effective mass of nucleons M^*, incompressibility modulus K_0, symmetry energy E_{sym} and density (ρ_0). We have shown these empirical values in Table 8.1. For a general idea and to see the behavior of these forces on binding energy per nucleon and pressure density, we have plotted Fig. 8.1(a). We get a stiff EOS for SH parameter, which is one of the oldest RMF interaction and a soft EOS for LNS parameter. The rest of the EOS's for various parameter sets are between these two extremes. Our theoretical EOS for RMF and SHF results are compared with the most accepted experimental data of Danielewicz et al. [312] in Fig. 8.1(b). From the figure, it is seen that all the EOS predicted with SHF formalism passes nicely through the experimental shaded region. On the other hand, the RMF based EOS of NL3, SH and TM1 are far from the experimental observation.

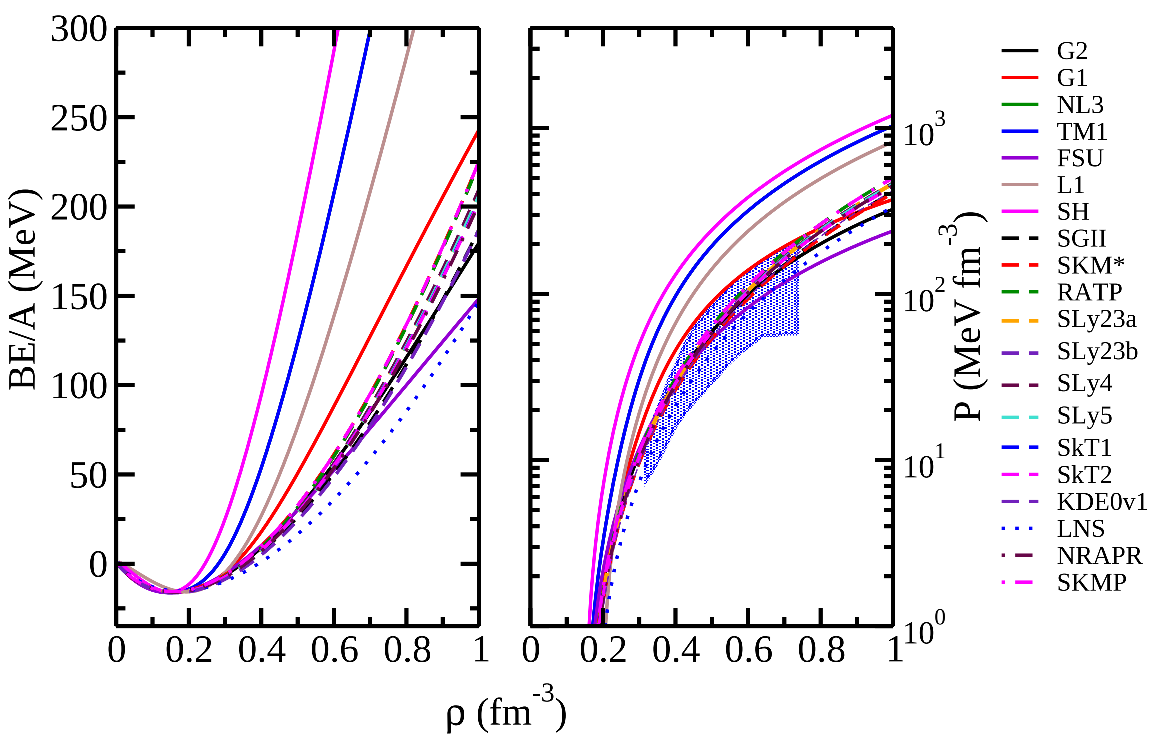

Figure 8.1: (a) Binding energy per nucleon (BE/A) (MeV) and (b) Pressure density for symmetric nuclear matter with non-relativistic and relativistic models as a function of baryon density.

However, the recently proposed G1 and G2 sets of RMF formalism very much within the experimental shaded region. These parameters not only match with the EOS of Ref. [312] but also predict the recent mass of neutron star [96].

We have noted down the maximum mass and the corresponding radius obtained from various parameter sets using TOV solution in Fig. 8.2 (a). Again from the rotating neutron star (RNS) code, we collected the M_{max} and R_{max} for the rotational cases in Fig. 8.2 (b). Here also, we put the result of pulsar J1614-2230 [96] as a standard reference shown by the horizontal strip and compared our results. Comparing the mass of static and rotational star, one can easily see that rotational neutron star mass is larger than the static one. As Demorest et al. [96] stated that the theoretical models should have the maximum mass more or near to $(1.97 \pm 0.04)M_{\odot}$, the Shapiro delay provides no information for the neutron star's radius and we can not put any constraint on the radius of neutron star. The non-relativistic model parameter LNS is not comfortable in static case, but it is within the cut off region for rotational NS.

From the figure, a larger number of parameter sets, like FSU, SGII, SkM*, LNS, RATP and SkT2 are not crossing the horizontal strip, which is the experimental constraint on static/slowly rotating neutron star mass ($\frac{M}{M_{\odot}}$) [96]. To reproduce the recent star mass [96] (as the masses do not lie within the experimental strip) FSU parameter set [64] has been extended to IUFSU [65] to keep the prediction within the experimental constraint. For non-relativistic sets, the forces are chosen by taking into consideration their success in finite nuclei. For more descriptive study, we refer the readers to go through Refs. [117, 319], where one will get 214 sets of SHF parametrization and their applications to various systems.

Before going to discuss the gravitational wave frequency ν_{gw}, we would like to see the rotational frequency $\nu_r = \frac{\Omega_K}{2\pi}$ of neutron star and the related quantities, such as I, Φ_{22} and ϵ used for the evaluation of gravitational wave strain h_0. The value of ν_r obtained from various parameter sets are shown in Figure 8.3 (a). The ν_r of a NS are found to be within 700 to 1200 Hz for all the considered SHF and RMF parameter sets. The maximum rotational frequency 1200 Hz is predicted by the non-relativistic SGII and RATP sets. Unlike to the rotational Keplerian frequency Ω_K, the gravitational frequency ν_{gw} is a tedious experimental exploration [325, 327]. The calculated values of ν_{gw} obtained by various SHF and RMF parametrizations are almost double of the rotational frequency ν_r, because of its polarity.

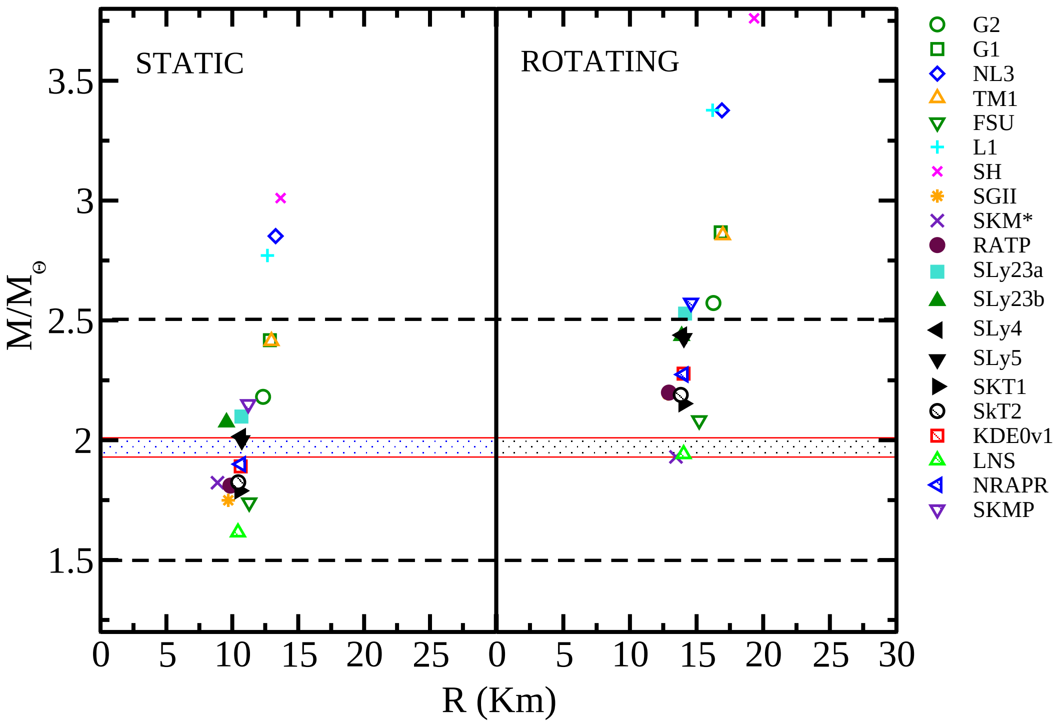

Figure 8.2: Maximum mass ratio ($M/M_{\odot}$) and radius R (km) of static and rotating neutron star obtained from TOV and RNS models with various non-relativistic and relativistic model parameters.

In Fig. 8.3(b), we have given the moment of inertia I of the rotating neutron star. Since, inertia is a static property, it is totally depends on its mass distribution, i.e. the maximum mass and corresponding radius. The APR and DBHF + Born B results are also given in the figure for comparison. For quantitative understanding of the quadrupole moment Φ_{22} in different relativistic and non-relativistic models parameters, we have calculated Φ_{22}. Although, it is not valid for high frequency rotating star, but for qualitative behavior of model parameter, we can use this approximate relation, which depends only on the mass and radius of the neutron star with the breaking strain of the neutron star crust σ. At present, the σ value is very much uncertain and its limiting range is $\sigma = 10^{-5} - 10^{-2}$ [328]. In the calculations, the two chosen values of σ (10^{-2} and 10^{-3}) are taken to evaluate Φ_{22} and the

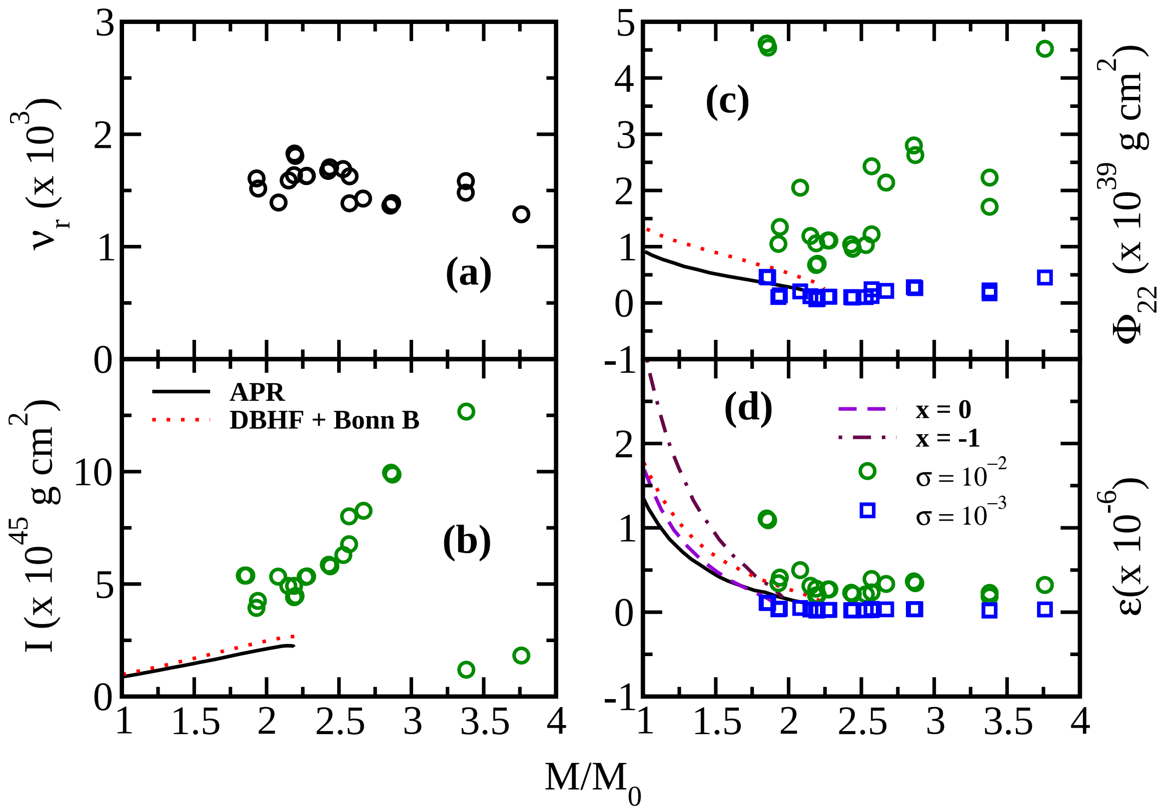

Figure 8.3: Rotational frequency ν_r, moment of inertia I, quadrupole deformation Φ_{22} and ellipticity ϵ from various parameter sets.

results are shown in Fig. 8.3 (c). The results are also compared with the theoretical predictions of APR and DBHF + Bonn B. The APR results shown by black line, which shows the decrease of quadrupole moment of neutron star with mass M. Also, we get same trend in DBHF + Bonn B (red colour in Fig. 8.3(c)) predictions. The results with $\sigma = 10^{-3}$, match well to the APR and DBHF + Bonn B predictions, while for $\sigma = 10^{-2}$, we get very scattered values as shown in Fig. 8.3(c). The ellipticity of a neutron star is an important observable, which gives the structural variation of a star from its spherical shape. We have given our calculated results obtained by all the force parameters in Fig. 8.3(d). We have also compared our results with two theoretical models APR (black line) and DBHF + Bonn B (blue dash line) along with the two experimental results of Ref. [329] for $x = 0$ (red dotted line) and -1 (green dotted dash line). Here, we have shown the results of two sets with $\sigma = 10^{-2}$ and $\sigma = 10^{-3}$, which are shown by open circle and square in Fig. 8.3(d). As this is rotational star, the maximum mass is larger compared to slowly rotating one. If

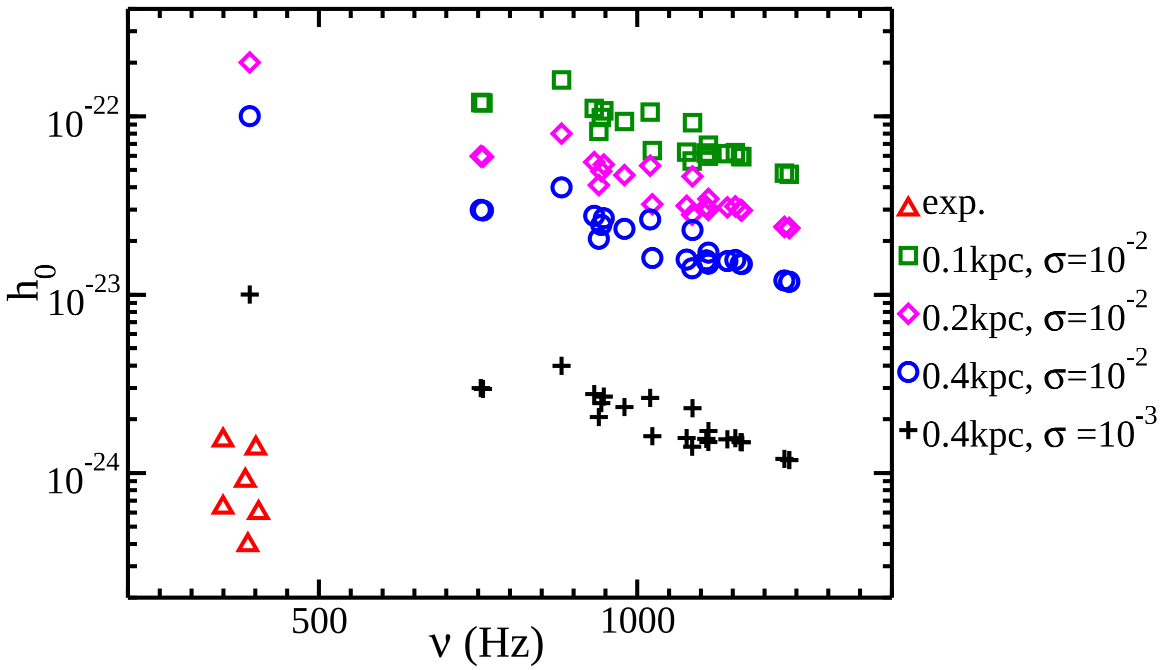

Figure 8.4: The gravitational wave strain amplitude h_0 from various parameter sets.

we see the results shown in Fig. 8.3(d), our calculated result still matches with the earlier work for large NS mass. Thus our predicted ellipticity of rotating neutron star using various parameter sets, where their origin are very much different from each other are almost similar. The variation of the ellipticity ϵ obtained from various star mass is very small. This will be helpful for us to constrain the results of quadrupole moment, moment of inertia and breaking strain of the neutron star.

For a rotating neutron star, the gravitational wave amplitude h_0 is an experimental observable. We can observed it directly by specially designed experimental setup [325, 327]. The gravitational wave is generated by the rotation of an axially asymmetric neutron star. The wave strain amplitude h_0 can be measured by knowing the maximum mass and corresponding radius of a star. Apart from the mass and radius, the quadrupole moment Φ_{22}, moment of inertia along the rotation axis I_{zz}, ellipticity of the star due to rotation ϵ and rotational frequency ν_r are essential inputs for the estimation of the gravitational wave strain h_0. These values are depicted in Figure 8.3 for $\sigma = 10^{-2}$ and $\sigma = 10^{-3}$ with $r = 0.1, 0.2$ and 0.4 kpc. These are some standard values used by earlier calculations [329]. So in this way, we have given the GW strain amplitude and frequency relation for four sets of data as shown in the Fig. 8.4 along with the experimental results (for more discussion, see

Ref. [329]). Here, the gravitational frequencies obtained more than 500 Hz from all the parameter sets. We have noticed an important point here is that the gravitational wave strain amplitude decreases with increasing r and decreases with the value of breaking strain of neutron star crust σ.

In summary, the calculated gravitational wave strain amplitude, gravitational wave frequency, Keplerian frequency, quadrupole moment and ellipticity of rotating neutron star are almost consistent with all the considered models which show the model independent predictions of the observables. We found that gravitational wave strain amplitude is a function of breaking strain of neutron star crust and distance between the star and the earth. From our calculation, we approximate the range of the gravitational wave amplitude between 10^{-24} to 10^{-22} for rotating neutron star. The moment of inertia of the star comes around $\sim 10^{45}\ gcm^2$ and the predicted range of gravitational wave frequency is in between 400 to 1280 Hz. We have calculated the rotating frequency of star and concluded that, if we increase the rotating frequency then the increment in the mass is also changes subsequently. The ellipticity of the neutron star is consistent in all the considered 20 parameter sets which will be helpful to constrain the value of quadrupole and moment of inertia of the NS and vice versa.

Chapter 9

Summary and Conclusions

In the present thesis, we summarise the main finding and conclusion of our thesis in this chapter. In first part of the thesis, we have used effective mean field models (SHF and RMF) and discussed the finite nuclei properties like binding energy, charge radius, nucleon density distribution, shapes (prolate, oblate and spherical), and evolution of single particle orbits. Apart from these finite nuclei properties, we discussed the microscopic origin of NN-potential, which is one of the most outstanding problems of all time in nuclear physics study. Here, we have derived a nucleon-nucleon potential R3Y and NR3Y starting from a microscopic level, which can be used as an alternative of M3Y or DDM3Y NN-interactions. The NN-potential (NR3Y) so obtained is an appropriate replacement substitution for the widely used M3Y potential, which has empirical origin. The main point of NR3Y (Non-linear three Yukawa) potential is that the constants are generated from the well established RMF parameters (HS, NL3). The NR3Y interaction is very useful in many body system at low energy.

We have used the effective mean field models in low mass region and study the parity doublet in low lying Ω states in **Chapter 4**. We have able checked the applicability of mean field formalism in Ne-S (Neon to Sulphur) region of the mass table comparing with the experimental data. We found that the considered models (SHF, RMF) are good enough to explain the drip-line nuclei ^{40}Mg and ^{42}Al which are predicted by various mass models beyond the drip-line. We have analyzed the shape coexistence and deformation parameters of these considered nuclei within the effective mean field approaches. We found that the low Ω orbits (Ω=$\frac{1}{2}$) becomes more bound and nearly degenerate with the orbits of opposite parity, i.e. they show parity doublet structure. Low lying parity doublet band structures and enhanced odd parity multipole transitions are possible for the superdeformed shape.

In **Chapter 5**, we have calculated the binding energy (BE), charge (r_{ch}) and matter radii (r_{rms}), quadrupole deformation parameter (β_2) for the neutron drip-line nuclei having atomic number Z=17-23, 37-40 and 60-64 using RMF (NL3*) formalism. These regions are recently predicted to be extra stable compared to their near by isotopes, hence termed as "island of inversion". Since the considered isotopes are experimentally unknown, we compared our results with the predictions of various mass formulas (FRDM and INM). We found large differences both in binding energy and deformation parameters indicating the special nature of these nuclei. This type of special features can be resolved by experimental verification which may be possible in near future, because of the evolution of advance experimental facilities. For more definite conclusions, one needs extra attention for these drip-line nuclei. In our analysis, we got some interesting features like a bump and pit at some places in charge distribution radius, which are different from the conventional distribution.

In second part of the thesis, major portion is focused on extension of the model. This is done by incorporating some extra terms into the model Lagrangian. In this way, we included cross coupling interaction, which arises due to the coupling between isovector-vector $\rho-$meson and isoscalar-vector $\omega-$meson in **Chapter 6**. The important point for this term is that it does not affect the symmetry part of the system, but changes the neutron skin, giant dipole resonance and symmetry energy. It also makes the equation of state (EOS) softer and bring the compressibility down, which is one of the successes of the modification. We have discussed its effects on finite and infinite nuclear systems in a very extensive way and showed its applicability. We added this coupling on top of the E-RMF parametrization (G2 parameter) which is a very successful parameter set available in literature. It plays a crucial role in softening the symmetry energy (E_{sym}) at large baryon density. The E_{sym} is found to be softer with the value Λ_v ~0.15 (cross coupling constant of $\rho-\omega$) and after that overestimate to the experimental results. The results match with the experimental data as well as other theoretical predictions for E_{sym} and L_{sym} at saturation density for different values of Λ_v. The effects on composition of neutron star and mass radius trajectory are also very important. With the help of this cross coupling, we can obtain the mass and radius of neutron star within current experimental observations, which are very good constraints on nuclear models. The predicted range of Λ_v helps us in developing new parameter sets.

With the same motivation, we include an extra meson degree of freedom into the model, i.e. the $\delta-$meson, which arises due to the mass difference of neutron and proton (**Chapter 7**). The effects of extra coupling on finite and infinite nuclear systems are discussed and it concluded that mass isospin is important only in the large asymmetric systems (drip-line nuclei). We have discussed the effects of $\delta-$meson coupling on BE, r_{ch} and single particle energy levels of nucleons. From the analysis, we conclude that $\delta-$meson is more effective than the cross coupling on finite and infinite systems. The variation in the coupling constants are taken care on top of G2 parameter and we keep the original G2 parameter intact. To avoid double counting of isospin, one needs more care to handle the $\delta-$meson coupling in the presence of $\rho-$meson. For this, we split the isospin part of the system into two components and again re-shuffle the coupling constants of ρ and $\delta-$mesons to get the same physical observables. Finally, with these obtained combinations (g_ρ, g_δ), we have evaluated the BE, r_{ch}, single particle energy and spin-orbit interaction potential for ^{48}Ca and ^{208}Pb. The $\delta-$meson coupling can make the EOS stiffer at large baryon density which will estimate a heavier mass of neutron star (NS). Another beauty of $\delta-$coupling is to make the softer E_{sym} at higher density which is one of the most awaited results from the experimental side. The behavior of symmetry energy near the saturation density is well understood but it is totally unknown for away from the saturation density. So, a proper fitting of coupling constants inneed for the upcoming experiments.

In **Chapter 8**, an extensive study has been done on the Nuclear Astrophysics. Here, we analyzed the behaviour of static and rotating neutron star. We used several (more than 20) relativistic and non-relativistic parameter sets for mass and radius of NS. Properties of rotating neutron star like gravitational wave strain amplitude, gravitational wave frequency, Keplerian frequency, quadrupole moment and ellipticity are calculated with various forces. Maximum mass and its corresponding radii are used to calculate these observables. We got almost consistent results with all considered forces, which shows the model independent predictions of the observables. We found that the gravitational wave strain amplitude is a function of breaking strain of neutron star crust and distance between the star and earth. From the calculations, we approximate the range of the gravitational wave amplitude between 10^{-24} to 10^{-22} for rotating neutron star. The moment of inertia of the star comes around $\sim 10^{45}$ gcm^2 and the predicted range of the gravitational wave frequency is in between 400 to 1280 Hz. We have calculated the rotating frequency of star and concluded that, if we increase the rotating frequency then the increment in the mass also changes subsequently. The ellipticity of the neutron star is consistent in all the considered parameter sets which will be helpful to constrain the value of quadrupole moment and moment of inertia of neutron star and vice versa. Our results will be helpful to the new generation of gravitational wave detectors families.

The whole work of the thesis is based on the Hartree and Hartree-Fock approximations. Within this approximation, one can only analyze ground and intrinsic excited states of the system. To study the excited band structure of a nucleus, one should extend the model beyond the mean field level. This can be achieved by including the particle-hole correlations via the small amplitude limit of the Hartree and Hartree-Fock equations. This allows one to describe the excitation energy of Giant Resonances in nuclei. Another approach is to use particle hole correlations to study collective nuclear surface vibrations and allow them to interact with single particle degrees of freedom. Such a scheme correspond to the Particle Vibration Coupling (PVC) approach. These corrections are very useful in the context of current experimental research. So, study of the nuclear properties within these corrections will be interesting and able to solve many outstanding problems of nuclear physics community.

Bibliography

[1] J. Chadwick, Proc. Roy. Soc. A **136**, 692 (1932).

[2] J. W. Xia et al., The heavy ion cooler-storage-ring project (HIRFL-CSR) at Lanzhou, Nucl. Instr. and Meth. A **488**, 11 (2002).

[3] J. W. Xia, W. L. Zhan, B. W. Wei, and CSR group, Cooler storage ring at china institute of modern physics, Proc. PAC **05**, 271 (2005).

[4] An International Accelerator Facility for Beams of Ions and Antiprotons, GSI report 2006. http://www.gsi.de/GSI-Future/cdr/.

[5] H. Simon, in Proceedings of the International Workshop XXXII on Gross Properties of Nuclei and Nuclear Excitations, Hirschegg (Austria), 2004, edited by M. Buballa, J. Knoll, W. Norenberg, B.-J. Schaefer, and J. Wambach (GSI, Darmstad, 2004) 290.

[6] M.-G. Saint-Laurent et al. Final report SPIRAL PHASE-II (2001) in: http://pro.ganil-spiral2.eu/spiral2/origin-of-spiral2/ spiral-phase-iieuropean- rtt-final-report/view

[7] T. Suda, K. Maruyama, and I. Tanihata, RIKEN Accel. Prog. Rep. **34**, 49 (2001).

[8] Facility for Rare Isotope Beams at Michigan State University, http://www.frib.msu.edu/about/msu-frib-proposal.

[9] S. Hofmann and G. Münzenberg, Rev. Mod. Phys. **72**, 733 (2000).

[10] G. Münzenberg et al., Z. Phys. A **300**, 107 (1981).

[11] S. Hofmann et al., Z. Phys. A **350**, 277 (1995).

[12] S. Hofmann et al., Z. Phys. A **350**, 281 (1995).

[13] S. Hofmann et al., Z. Phys. A **354**, 229 (1996).

[14] S. Hofmann et al., Rep. Prog. Phys. **61**, 639 (1998); Acta Phys. Pol. B **30**, 621 (1999).

[15] S. Hofmann, Russ. Chem. Rev. **78**, 1123 (2009).

[16] Yu. Ts. Oganessian, Phys. Rev. Lett. **83**, 3154 (1998).

[17] Yu. Ts. Oganessian et al., Nucl. Phys. A **685**, 17c (2001).

[18] Yu. Ts. Oganessian et al., Phys. Rev. C **69**, 021601(R) (2004).

[19] Yu. Oganessian, J. Phys. G: Nucl. Part. Phys. **34**, R165 (2007).

[20] Yu. Ts. Oganessian et al., Phys. Rev. Lett. **104**, 142502 (2010).

[21] Yu. Ts. Oganessian et al., Phys. Rev. C **83**, 954315 (2011).

[22] H. Yukawa, Proc. Phys. Math. Soc. Japan **17**, 48 (1935).

[23] C. M. G. Lattes, H. Muirhead, G. P. O. Occhialini, and C. F. Powell, Nature **159**, 694 (1947).

[24] O. Dumbrajs, R. Koch, H. Pilkuhn, G. C. Oades, H. Behrens, J. J. De Swart, and P. Kroll, Nucl. Phys. B **216**, 277 (1983).

[25] F. E. Close, *An Introduction to Quarks and Partons*, (Academic Press, London, 1979).

[26] B. D. Serot and J. D. Walecka, Adv. Nucl. Phys. **16**, 1 (1986).

[27] L. D. Miller and A. E. S. Green, Phys. Rev. C **5**, 241 (1972).

[28] J. D Walecka, Ann. Phys. (NY) **83**, 491 (1974).

[29] R. Brockmann and W. Weise, Phys. Rev. C **16**, 1282 (1977).

[30] Particle Data Group, Eur. Phys. J. C **363**, 390 (1998).

[31] Particle Data Group, 2012.

[32] Jun-ichi Fujita and H. Miyazawa, Prog. Theor. Phys. **17**, 360 (1957).

[33] L. I. Schiff, Phys. Rev. **80**, 137 (1950); Phys. Rev. **83**, 239 (1951); Phys. Rev. **84**, 1 (1950).

[34] Y. Sugahara and H. Toki, Nucl. Phys. A **579**, 557 (1994).

[35] A. R. Bodmer, Nucl. Phys. A **526**, 703 (1991).

[36] P. Arumugam, B. K. Sharma, P. K. Sahu, S. K. Patra, T. Sil, M. Centelles, and X. Viñas, Phys. Lett. B **601**, 51 (2004).

[37] S. Gmuca, Z. Phys. A **342**, 387 (1992); Nucl. Phys. A **547**, 447 (1992).

[38] S. K. Patra and C. R. Praharaj, Phys. Rev. C **44**, 2552 (1991).

[39] R. Machleidt, Advance in Nuclear Physics, Edited by J. W. Negele and E. Vogt, **19**, 189 (1989)

[40] J. A. Oller and E. Oset, AIP Conference Proceedings **432**, 824 (1998).

[41] W. H. Long, N. Van Giai, and J. Meng, Phys. Lett. B **640**, 150 (2006).

[42] W. H. Long, H. Sagawa, N. V. Giai, and J. Meng, Phys. Rev. C **76**, 034314 (2007).

[43] W. H. Long, H. Sagawa, J. Meng, and N. Van Giai, Europhys. Lett. **83**, 12001 (2008).

[44] W. H. Long, P. Ring, N. Van Giai, and J. Meng, Phys. Rev. C **81**, 024308 (2010).

[45] S. Kubis and M. Kutschera, Phys. Lett. B **399**, 191 (1997).

[46] H. Huber, F. Weber and M. K. Weigel, Nucl. Phys. A **596**, 684 (1996).

[47] H. Huber, F. Weber, and M. K. Weigel, Int. J. Mod. Phys. E **7**, 301 (1998).

[48] J. Leja and S. Gmuca, Acta Phys. Slov. **51**, 201 (2001).

[49] B. Liu, V. Greco, V. Baran, M. Colonna, and M. DiToro, Phys. Rev. C **65**, 045201 (2002).

[50] V. Greco, M. Colonna, M. DiToro, and F. Matera, Phys. Rev. C **67**, 015203 (2003).

[51] S. S. Avancini, L. Brito, D. P. Menezes, and C. Providencia, Phys. Rev. C **70**, 015203 (2004).

[52] T. Gaitanos, M. DiToro, S. Typel, V. Barana, C. Fuchs, V. Greco, and H. H. Wolter, Nucl. Phys. A **732**, 24 (2004).

[53] V. Baran, M. Colonna, V. Greco, and M. DiToro, Phys. Rep. **410**, 335 (2005).

[54] B. Liu, M. DiToro, and V. Greco, Int. J. Mod. Phys. E **9**, 1815 (2008).

[55] H. Pais, A. Santos, and C. Providencia, Phys. Rev. C **80**, 045808 (2009).

[56] A. Rabhi, C. Providencia, and J. DaProvidencia, Phys. Rev. C **80**, 025806 (2009).

[57] G. B. Alaverdyan, Res. Astron. Astrophys. **10**, 1255 (2010).

[58] H. Chiu and E. E. Salpeter, Phys. Rev. Lett. **12**, 413 (1964).

[59] J. N. Bahcall and R. A. Wolf, Phys. Rev. Lett. **14**, 343 (1965).

[60] J. M. Lattimer, C. J. Pethic, M. Prakash, and P. Haensel, Phys. Rev. Lett. **66**, 2701 (1991).

[61] C. F. Von Weizsäcker, Z. Physik **96**, 431 (1935).

[62] G. A. Lalazisis, J. König, and P. Ring, Phys. Rev. C **55**, 540 (1997).

[63] G. A. Lalazissis, S. Karatzikos, R. Fossion, D. Pena Arteaga, A. V. Afanasjev, and P. Ring, Phys. Lett. B **671**, 36 (2009).

[64] B. G. Todd-Rutel, and J. Piekarewicz, Phys. Rev. Lett. **95**, 122501 (2005).

[65] F. J. Fattoyev, C. J. Horowitz, J. Piekarewicz, and G. Shen, Phys. Rev. C **82**, 055803 (2010).

[66] W. Zuo, I. Bombaci, and U. Lombardo, Phys. Rev. C **60**, 024605 (1999).

[67] W. Zuo, A. Lejeune, U. Lombardo, and J. F. Mathiot, The European Physical Journal A **14**, 469 (2002).

[68] F. Hofmann, C. M. Keil, and H. Lenske, Phys. Rev. C **64**, 034314 (2001).

[69] B.-A. Li, Phys. Rev. C **69**, 064602 (2004).

[70] D. D. S. Coupland, et. al., arXiv:1406.4546

[71] Q. F. Li et al., Phys. Rev. C **72**, 034613 (2005).

[72] B. A. Li, Phys. Rev. Lett **88**, 192701 (2002).

[73] F. Gulminelli and P. Chomaz, Phys. Rev. C **71**, 054607 (2005).

[74] G. C. Yong, B. A. Li, L. W. Chen, W. Zuo, Phys. Rev. C **73**, 051601 (2006).

[75] Z. G. Xiao et. al., Nucl. Part. Phys **36**, 064040 (2009).

[76] Z. Xiao, B.-A. Li, L.-W. Chen, G.-C. Yong, and M. Zhang, Phys. Rev. Lett. **102**, 062502 (2009).

[77] Y. Gao, L. Zhang, W. Zuo, J. Q. Li, Phys. Rev. C **86**, 034611 (2012).

[78] H. H. Wolter, Progress in Particle and Nuclear Physics **59**, 365 (2007).

[79] W. P. Tan et. al., Phys. Rev. C **64**, 051901 (2001).

[80] V. Baran et. al., Nucl. Phys. A **703**, 603 (2002).

[81] B. A. Li and C. M. Ko, Nucl. Phys. A **618**, 498 (1997).

[82] L. W. Chen, C. M. Ko and B. A. Li, Phys, Rev. C **68**, 017601 (2003); Nucl. Phys. A **729**, 809 (2003).

[83] Y. Zhang and Z. Li, Phys. Rev. C **71**, 024604 (2005).

[84] H. S. Xu et. al., Phys. Rev. Lett. **85**, 716 (2000).

[85] H. Muller and B. Serot, Phys. Rev. C 52, 2072 (1995).

[86] B. A. Li, Phys. Rev. Lett **85**, 4221 (2000).

[87] H. Liu, G. Yong and D. Wen, arXiv:1406.6504v2.

[88] B. A. Brown, Phy. Rev. Lett. **85**, 5296 (2000).

[89] X. Roca-Maza, X. Viñas, M. Centelles, P. Ring and P. Schuck, Phys. Rev. C **84**, 054309 (2011).

[90] C. J. Horowitz and J. Piekarewicz, Phy. Rev. C **66**, 055803 (2002)

[91] C. J. Horowitz and J. Pickarewicz, Phys. Rev. Lett. **86**, 5647 (2001); Phys. Rev. C **64**, 062802 (R) (2001).

[92] Wen-Mei Guo, Gao-Chan Yong, Y. Wang, Q. Li, H. Zhang and W. Zuo, arxiv:1404.7217v1

[93] B. K. Sharma and S. Pal, Phys. Lett. B **682**, 23 (2009).

[94] F. J. Fattoyev, W. G. Newton and Bao-An Li, Eur. Phys. J. A, **50**, 45 (2014).

[95] John Antoniadis et al., Science **340** 6131 (2013).

[96] P. B. Demorest, T. Pennucci, S. M. Ransom, M. S. E. Roberts, and J. W. T. Hessels, Nature **467**, 1081 (2010).

[97] Irwin I. Shapiro, Phys. Rev. Lett. **13**, 789 (1964).

[98] J. M. Lattimer, A. W. Steiner, 1305.3242v2

[99] J. R. Oppenheimer and G. M. Volkoff, Phys. Rev **55**, 374 (1939); R. C. Tolman, Phys. Rev **55**, 364 (1939).

[100] Shailesh K. Singh, S. K. Biswal, M. Bhuyan, T. K. Jha, and S. K. Patra, arXiv:1312.5840.

[101] J. W. Negele and K. Yazaki, Phys. Rev. Lett. **47**, 71 (1981).

[102] J. C. Caillon and J. Labarsouque, Phys. Rev. C **54**, 2069 (1996).

[103] T. Sil, S. K. Patra, B. K. Sharma, M. Centelles, and X. Viñas, Phys. Rev. C **69**, 044315 (2004).

[104] M. Bhuyan and S. K. Patra, Mod. Phys. Lett. A **27**, 1250173 (2012).

[105] R. K. Gupta, S. K. Patra, and W. Greiner, Mod. Phys. Lett. A **12**, 1317 (1997).

[106] V. M. Strutinsky, Nucl. Phys. A **95**, 420 (1967).

[107] P. Möller, J. R. Nix, and K.-L. Kratz, Atomic and Nucl. Data Tables **66**, 131 (1997).

[108] P. Möller and J. R. Nix, Nucl. Phys. A **361**, 117 (1981).

[109] L. Satpathy and R. C. Nayak, Phys. Rev. Lett. **51**, 1243 (1983).

[110] N. H. Hugenholtz and W. Van Hove, Physica **24**, (1958).

[111] P. Navrátil and B. R. Barrett, Phys. Rev. C **57**, 562 (1998).

[112] P. Navrátil, J. P. Vary, and B. R. Barrett, Phys. Rev. Lett. **84**, 5728 (2000); Phys. Rev. C **62**, 054311 (2000).

[113] D. C. Zheng, B. R. Barrett, L. Jaqua, J. P. Vary, and R. J. McCarthy, Phys. Rev. C **48**, 1083 (1993).

[114] B. D. Day, Phys. Rev. C **24**, 1203 (1981); Phys. Rev. Lett. **47**, 226 (1981).

[115] F. Coester, S. Cohen, B. D. Day, and C. M. Vincent, Phys. Rev. C **1**, 769 (1970).

[116] C. J. Horowitz and B. D. Serot, Phys. Lett. B **137**, 287 (1984).

[117] M. Dutra et al., Phy. Rev. C **85**, 035201 (2012).

[118] E. Chabanat, P. Bonche, P. Hansel, J. Meyer, and R. Schaeffer, Nucl. Phys. A **627**, 710 (1997).

[119] E. Chabanat, P. Bonche, P. Haensel, J. Meyer, and R. Schaeffer, Nucl. Phys. A **635**, 231 (1998).

[120] P.-G. Reinhard and H. Flocard, Nucl. Phys. A **584**, 467 (1995).

[121] P. Ring and P. Schuck, *The Nuclear Many-Body Problem*, **Springer**, (2004).

[122] B. A. Brown, Phys. Rev. C **58**, 220 (1998).

[123] S. K. Patra, C.-L. Wu, C. R. Praharaj, and R. K. Gupta, Nucl. Phys. A **651**, 117 (1999).

[124] M. Bender, Paul-Henri Heenen, and P.-G. Reinhard, Rev. Mod. Phys. **75**, 121 (2003).

[125] J. R. Stone, J. C. Miller, R. Koncewicz, P. D. Stevenson, and M. R. Strayer, Phys. Rev. C **68**, 034324 (2003).

[126] B. D. Serot, Rep. Prog. Phys. **55**, 1855 (1992).

[127] Y. K. Gambhir, P. Ring, and A. Thimet, Ann. Phys. (N.Y.) **198**, 132 (1990).

[128] J. Boguta and A. R. Bodmer, Nucl. Phys. A **292**, 413 (1977).

[129] P. Ring, Prog. Part. Nucl. Phys. **37**, 193 (1996).

[130] M. H. Johnson and E. Teller, Phys. Rev. **98**, 783 (1955).

[131] H. P. Duerr, Phys. Rev. **103**, 469 (1956).

[132] B. F. Rozsnayi, Phys. Rev. **124**, 860 (1961).

[133] J. P. Blaizot, Phys Rep. **64**, 171 (1980).

[134] M. Rufa, P.-G. Reinhard, J. A. Maruhn, W. Greiner, and M. R. Strayer, Phys. Rev. C **38**, 390 (1988).

[135] P.-G. Reinhard, M. Rufa, J. Maruhn, W. Greiner, and J. Friedrich, Z. Phys. A **323**, 13 (1986).

[136] M. Sharma, G. A. Lalazissis, and P. Ring, Phys. Lett. B **317**, 9 (1993).

[137] D. Vautherin and D. M. Brink, Phys. Rev. C **5**, 626 (1972).

[138] J. Decharge and D. Gogny, Phys. Rev. C **21**, 1568 (1980).

[139] B. D. Serot and J. D. Walecka, Int. J. Mod. Phys. E **6**, 515 (1997).

[140] H. Müller and B. D. Serot, Nucl. Phys. A **606**, 508 (1996).

[141] S. K. Patra, M. Del Etal, M. Centelles, and X. Viñas, Phy. Rev. C **63**, 024311 (2001).

[142] R. J. Furnstahl, B. D. Serot, and H. B. Tang, Nucl. Phys. A **598**, 539 (1996).

[143] R. J. Furnstahl, B. D. Serot, and H. B. Tang, Nucl. Phys. A **615**, 441 (1997).

[144] D. Vretenar, A. V. Afanasjev, G. A. Lalazissis, and P. Ring, Phys. Rep. **409**, 101 (2005).

[145] P.-G. Reinhard, Rep. Prog. Phys. **52**, 439 (1989).

[146] J. Meng, H. Toki, S.-G. Zhou, S.-Q. Zhang, W.-H. Long, and L.-S. Geng, Prog. Part. Nucl. Phys. **57**, 470 (2006).

[147] M. Del Estal, M. Centelles, and X. Viñas, Nucl. Phys. A **650**, 443 (1999).

[148] J. P. Elliott and T. H. R. Skyrme, Proc. R. Soc. London A **232**, 561 (1955).

[149] J. W. Negele, Phys. Rev. C **1**, 1260 (1970).

[150] M. A. Preston and R. K. Bhaduri, *Structure of Nucleus, Addison-Wesley Publishing Company*, Ch. 8, page 309 (1982).

[151] S. K. Patra, Phys. Rev. C **48**, 1449 (1993).

[152] D. G. Madland and J. R. Nix, Nucl. Phys. A **476**, 1 (1981).

[153] P. Möller and J.R. Nix, Atomic and Nucl. Data Tables **39**, 213 (1988).

[154] J. Dobaczewski, H. Flocard, and J. Treiner, Nucl. Phys. A **422**, 103 (1984).

[155] J. Dobaczewski, W. Nazarewicz, T.R. Werner, J.F. Berger, C. R. Chinn, and J. Decharge, Phys. Rev. C **53**, 2809 (1996).

[156] T. R. Werner, J. A. Sheikh, W. Nazarewicz, M. R. Strayer, A. S. Umar, and M. Mish, Phys. Lett. B **335**, 259 (1994).

[157] T. R. Werner, J. A. Sheikh, M. Mish, W. Nazarewicz, J. Rikovska, K. Heeger, A. S. Umar, and M. R. Strayer, Nucl. Phys. A **597**, 327 (1996).

[158] G. A. Lalazissis, D. Vretenar, P. Ring, M. Stoitsor, and L. M. Robledo, Phys. Rev. C **60**, 014310 (1999).

[159] G. A. Lalazissis, D. Vretenar, and P. Ring, Nucl. Phys. A **650**, 133 (1999).

[160] K. A. Brueckner and K. M. Watson, Phys. Rev. **92**, 1023 (1953).

[161] R. V. Reid, Ann. Phys. (N.Y.) **50**, 411 (1968).

[162] W. N. Cottingham, M. Lacombe, B. Loiseau, J. M. Richard, and R. Vinh Mau, Phys. Rev. D **8**, 800 (1978).

[163] M. M. Nagels, T. A. Rijken, and J. J. de Swart, Phys. Rev. D **17**, 768 (1978).

[164] R. Machleidt, K. holinde, and Ch. Elster, Phys. Rep. **149**, 1 (1987).

[165] C. Ordonez, L. Roy, and U. van Kolck, Phys. Rev. Lett. **72**, 1982 (1994).

[166] G. R. Satchler, and W. G. Love, Phys. Rep. **55**, 183 (1979).

[167] B. B. Singh, M. Bhuyan, S. K. Patra, and R. K. Gupta, J. Phys. G: Nucl. Part. Phys. **39**, 025101 (2012).

[168] C. J. Horowitz and B. D. Serot, Nucl. Phys. A **368**, 503 (1981).

[169] S. C. Pieper, V. R. Pandharipande, R. B. Wiringa1, and J. Carlson, Phys. Rev. C **64**, 014001 (2001).

[170] W. Pannert, P. Ring, and J. Boguta, Phys. Rev. Lett., **59**, 2420 (1987).

[171] R. Brockmann and R. Machleidt, Phys. Rev. C **42**, 1965 (1990).

[172] F. Cooper, A. Khare, N. R. Quintero, F. G. Mertens, and A. Saxena, Phys. Rev. E **85**, 046607 (2012); F. Cooper, A. Khare, B. Mihaila, and A. Saxena, Phys. Rev. E **82**, 036604 (2010).

[173] M. Del Estal, M. Centelles, X. Viñas, and S. K. Patra, Phys. Rev. C **63**, 024314, (2001).

[174] T. R. Routray, A. Mishra, S. K. Tripathy, B. Behera, and D. N. Basu, Eur. Phys. J. A **48**, 77 (2012).

[175] J. Theis, G. Grabner, G. Buchwald, J. Maruhm, W. Greiner, H. Stoker, and J. Polonyi, Phys. Rev. D **28**, 2286 (1983).

[176] P.-G. Reinhard, M. Rufa, J. Maruhn, W. Greiner, and J. Friedrich, Z. Phys. A **323**, 13 (1986).

[177] L. J. B. Goldfarb and Y. K. Gambhir, Nucl. Phys. A **401**, 557 (1983).

[178] Krishichayan, X. Chen, Y.-W. Lui, Y. Tokimoto, J. Button, and D. H. Youngblood, Phys. Rev. C **81**, 014603 (2010).

[179] B. B. Singh, S. K. Patra, and R. K. Gupta, Phys. Rev. C **82**, 014607 (2010).

[180] W. G. Love and G. R. Satchler, Nucl. Phys. A**159**, 1 (1970).

[181] W. G. Love and L. J. Parish, Nucl. Phys. A **157**, 625 (1970); W. G. Love, Nucl. Phys. A **192**, 49 (1972).

[182] R. Brockmann, Phys. Rev. C **18**, 1510 (1978).

[183] R. Finkelstein and M. Ruderman, Phys. Rev. **81**, 655 (1951).

[184] R. Machleidt, Adv. Nucl. Phys. **19**, 189 (1989).

[185] M. R. Anastasio, L. S. Celenza, W. S. Pong, and C. M. Shakin, Phys. Rep. **100**, 327 (1983).

[186] R. Brockmann and R. Machleidt, Phys. Lett. B **149**, 283 (1984).

[187] B. ter Haar and R. Malfliet, Phys. Rep. **149**, 207 (1987).

[188] A. Amorim and J. A. Tjon, Phys. Rev. Lett. **68**, 772 (1992).

[189] S. Rafi, A. Bhagwat, W. Haider, and Y. K. Gambhir, Phys. Rev. C **86**, 034612 (2012).

[190] D. T. Khoa, W. Von Oertzen, and H. G. Bohlen, Phys. Rev. C **49**, 1652 (1994).

[191] S. S Malik and R. K. Gupta, Phys. Rev. C **39**, 1992 (1989).

[192] R. K. Gupta and W. Greiner, Int. J. Mod. Phys. E **3**, 335 (1994).

[193] G. Audi, A. H. Wapstra, and C. Thiboult, Nucl. Phys. A **729**, 337 (2003).

[194] B. B. Sahu, S. K. Agarwalla, and S. K. Patra, Phys. Rev. C **84**, 054604 (2011).

[195] B. B. Singh, B. B. Sahu, and S. K. Patra, Phys. Rev. C **83**, 064601 (2011).

[196] Basudeb Sahu, G. S. Mallick, B. B. Sahu, S. K. Agarwalla, and C. S. Shastry, Phys. Rev. C **77**, 024604 (2008).

[197] M. Balasubramaniam and N. Arunachalam, Phys. Rev. C **71**, 014603 (2005).

[198] D. N. Basu, P. Roy Chowdhury, and C. Samanta, Phys. Rev. C **72**, 051601(R) (2005).

[199] P. J. Woods and C. N. Davids, Annu. Rev. Nucl. Part. Sci. **47**, 541 (1997).

[200] K. P. Rykaczewski et al., Nucl. Phys. A **682**, 270c (2001).

[201] C. N. Davids and H. Esbensen, Phys. Rev. C **64**, 034317 (2001).

[202] A. Navin et al., Phys. Rev. Lett. **85**, 266 (2000); H. Iwasaki et al., Phys. Lett. B **491**, 8 (2000); H. Iwasaki et al., Phys. Lett. B **481**, 7 (2000).

[203] T. Motobayashi et al., Phys. Lett. B **346**, 9 (1995).

[204] K. Tanaka et al., Phys. Rev. Lett. **104**, 062701 (2010).

[205] H. Iwasaki et al., Phys. Lett. B **522**, 227 (2001).

[206] T. Baumann et al., Nature **449**, 1022 (2007).

[207] P. Möller, R. J. Nix, W. D. Myers, and W. J. Swiatecki, Atomic and Nucl. Data Tables **59**, 185 (1995).

[208] A. Ozawa, T. Kobayashi, T. Suzuki, K. Yoshida, and I. Tanihata, Phys. Rev. Lett. **84**, 5493 (2000).

[209] T. Minamisono, T. Ohtsubo, I. Minami, S. Fukuda, A. Kitagawa, M. Fukuda, K. Matsuta, Y. Nojiri, S. Takeda, H. Sagawa, and H. Kitagawa, Phys. Rev. Lett. **69**, 2058 (1992).

[210] I. Tanihata, J. Phys. G: Nucl. Part. Phys. **22**, 157 (1996).

[211] T. Nakamura, J. Phys. Conf. Ser. **312**, 082006 (2011); T. Nakamura et al., Phys. Rev. Lett. **103**, 262501 (2009).

[212] G. Ripka, Adv. Nucl. Phys. **1**, 183 (1968); W. H. Bassichis, B. Giraud, and G. Ripka, Phys. Rev. Lett. **15**, 980 (1965).

[213] A. Bohr and B. R. Mottelson, Nuclear Structure Vol. I W A Benjamin, Inc (1969).

[214] G. A. Lalazissis, S. Raman, and P. Ring, Atomic and Nucl. Data Tables **71**, 1 (1999).

[215] S. Raman, C. W. Jr. Nestor, and P. Tikkanen, Atomic and Nucl. Data Tables **78**, 1 (2001).

[216] M. Wang, G. Audi, A. H. Wapstra, F. G. Kondev, M. MacCormick, X. Xu, and B. Pfeiffer, Chin. Phys. C **36**, 1603 (2012).

[217] R. C. Nayak and L. Satpathy, Atomic and Nucl. Data Tables **98**, 616 (2012).

[218] M. Samyn, S. Goriely, M. Bender, and J. M. Pearson, Phys. Rev. C **70**, 044309 (2004).

[219] I. Angeli and K. P. Marinova, Atomic and Nucl. Data Tables **99**, 69 (2013).

[220] J. P. Maharana, Y. K. Gambhir, J. A. Sheikh, and P. Ring, Phys. Rev. C **46**, R1163 (1992).

[221] S. K. Patra and C. R. Praharaj, Phys. Rev. C **47**, 2978 (1993).

[222] F. Sarazin et al., Phys. Rev. Lett. **84**, 5062 (2000).

[223] J. L. Egido, L. M. Robledo, R. R. Rodriguez-Guzman, Phys. Rev. Lett. **93**, 282502 (2004).

[224] T. K. Jha, M. S. Mehta, S. K. Patra, B. K. Raj, and R. K. Gupta, PRAMANA -J. Phys. **61**, 517 (2003); L. Satpathy and S. K. Patra, Nucl. Phys. A **722**, 24c (2003); R. K. Gupta, M. Balasubramaniam, Sushil Kumar, S. K. Patra, G. Münzenberg, and W. Greiner, J. Phys. G **32**, 565 (2006).

[225] Ren Zhongzhou, Z. Y. Zhub, Y. H. Cai, and Xu Gongou, Phys. Lett. B **380**, 241 (1994).

[226] I. Hamamoto, Phys. Rev. C **76**, 054319 (2007); *ibid* C **85**, 064329 (2012).

[227] M. M. Sharma, M. A. Nagarajan, and P. Ring, Phys. Lett. B **312**, 377 (1993).

[228] R. Kanungo, I. Tanihata, and A. Ozawa, Phys. Lett. B **528**, 58 (2002).

[229] A. Bohr and B. R. Mottelson, Nuclear Structure, vol. II.

[230] C. R. Praharaj, *INT Workshop on "Nuclear Many-Body Approaches for the* 21^{st} *Century"*, September 24 - November 30, 2007, Institute for Nuclear Theory website, University of Washington, Seattle.

[231] C. R. Praharaj, *Structure of Atomic Nuclei*, Ch. 4, page 108, Edited by Satpathy L, Narosa Publishers (Delhi) (1999).

[232] D. Miller et al., Phys. Rev. C **79**, 054306 (2009).

[233] E. K. Warburton, J. A. Becker, and B. A. Brown, Phys. Rev. C **41**, 1147 (1990).

[234] E. K. Warburton, J. A. Becker, D. J. Millener, and B. A. Brown, *BNL report* 40890 (1987) .

[235] E. Caurier, G. Martinez - pinedo, F. Nowacki, A. poves, and A. P. Zuker, Rev. Mod. Phys. **77**, 427 (2005).

[236] S. K. Patra and C. R. Praharaj, Phys. Letters. B **273**, 13 (1991).

[237] J. Duflo and A. Zucker, Phys. Rev. C **52**, R23 (1996).

[238] O. B. Tarasov et al., Phys. Rev. Lett. **102**, 142501 (2009).

[239] S. M. Lenzi et al., Phys. Rev. C **82**, 054301 (2010).

[240] R. C. Nayak and L. Satapathy, Atomic and Nucl. Data Tables **98**, 616 (2012).

[241] S. K. Patra, P. Arumugam, and L. Satpathy, Bulletin Board Nucl-Th/0504063.

[242] P. Möller, J. R. Nix, and K.-L. Kratz, Atomic and Nucl. Data Tables **66**, 131 (1997).

[243] K. Tshoo et al., Phys. Rev. Lett. **109**, 022501 (2012).

[244] D. Vretenar, A. Wandelt, and P. Ring, Phys. Lett. B **487**, 334 (2000).

[245] D. Vretenar, T. Niksic, and P. Ring, Phys. Rev. C **68**, 024310 (2003).

[246] G. Colò, P. F. Bortignon, N. Van Gai, A. Bracco, and R. A. Broglia, Phys. Lett. B **276**, 279 (1992).

[247] J. P. Blaizot, J. F. Berger, J. Decharge, and M. Girod, Nucl. Phys. A **591**, 435 (1995).

[248] I. Hamamoto, H. Sagawa, and X. Z. Zhang, Phys. Rev. C **56**, 3121 (1997).

[249] K. A. Brueckner, C. A. Levinson, and H. M. Mahmoud, Phys. Rev. **95**, 217 (1954).

[250] H. A. Bethe, Phys. Rev. **103**, 1353 (1956).

[251] J. Goldstone, Proc. R. Soc. London, Ser. A **239**, 267 (1957).

[252] H. A. Bethe, Annu. Rev. Nucl. Sci. **21**, 93 (1971).

[253] M. R. Anastasio, L. S. Celenza, W. S. Pong, and C. M. Shakin, Phys. Rep. **100**, 327 (1983).

[254] C. J. Horowitz, and B. D. Serot, Nucl. Phys. A **464**, 613 (1987).

[255] R. Brockmann, and R. Machleidt, Phys. Rev. C **42**, 1965 (1990).

[256] J. Piekarewicz, Phys. Rev. C **66**, 034305 (2002).

[257] J. Piekarewicz, Phys. Rev. C **69**, 041301 (2004).

[258] N. K. Glendenning, F. Weber, and S. A. Moszkowski, Phys. Rev. C **45**, 844 (1992).

[259] H. Heiselberg and M. Hjorth-Jensen, Astrophys. J. Lett. **525**, L45 (1999).

[260] P. K. Panda, A. Mishra, J. M. Eisenberg, and W. Greiner, Phys. Rev. C **56**, 3134 (1997).

[261] J. Casares, P. A. Charles, and E. Kuulkers, Astrophys. J. Lett. **493**, L39 (1998).

[262] W. Kohn and L. J. Sham, Phys. Rev. **140**, A1133 (1965).

[263] T. Matsui, Nucl. Phys. A **370**, 365 (1981).

[264] C. Xu, B.-A. Li, and L.-W. Chen, Phys. Rev. C **82**, 054607 (2010).

[265] W. G. Newton, M. Gearheart, and B.-A. Li, *arXiv:1110.4043* (2011).

[266] A. W. Steiner and S. Gandolfi, Phys. Rev. Lett. **108**, 081102 (2012).

[267] F. J. Fattoyev, W. G. Newton, J. Xu, and B.-A. Li, Phys. Rev. C **86**, 025804 (2012).

[268] S. K. Singh, M. Bhuyan, P. K. Panda, and S. K. Patra, J. Phys. G: Nucl. Part. Phys. **40**, 085104 (2013).

[269] M. Tsang et al., Phys. Rev. C **86**, 015803 (2012).

[270] B. K. Agrawal, S. K. Dhiman, and R. Kumar, Phy. Rev. C **73**, 034319 (2006).

[271] P. A. M. Guichon, H. H. Matevosyan, N. Sandulescu, and A. W. Thomas, Nucl. Phys. A **772**, 1 (2006).

[272] F. Tondeur, M. Brack, M. Farine, and J. M. Pearson, Nucl. Phys. A **420**, 297 (1984).

[273] B. A. Brown (private communication).

[274] M. Rashdan, Mod. Phys. Lett. A **15**, 1287 (2000).

[275] B. A. Brown, G. Shen, G. C. Hillhouse, J. Meng, and A. Trzcińska, Phys. Rev. C **76**, 034305 (2007).

[276] M. B. Tsang, Y. Zhang, P. Danielewicz, M. Famiano, Z. Li, W. G. Lynch, and A. W. Steiner, Phys. Rev. Lett. **102**, 122701 (2009).

[277] A. Klimkiewicz et al., Phys. Rev. C **76**, 051603 (2007).

[278] A. Carbone, G. Col'o, A. Bracco, L.-G. Cao, P. F. Bortignon, F. Camera, and O. Wieland, Phys. Rev. C **81**, 041301 (2010).

[279] P. Danelewicz and J. Lee, *arXiv:1111.0326v1*.

[280] P. M öller, W. D. Meyers, H. Sagawa, and S. Yoshida, Phys. Rev. Lett. **108**, 052501 (2012).

[281] C. J. Horowitz, S. J. Pollock, P. A. Souder, and R. Michaels, Phys. Rev. C **63**, 025501 (2001).

[282] S. Abrahamyan et al., Phys. Rev. Lett. **108**, 112502 (2012).

[283] Jefferson Lab Experiment E12-11-101 (PREX-II). Proposal available at http://hallaweb.jlab.org/parity/prex.

[284] N. K. Glendenning, Compact Stars, Nuclear Physics, Particle Physics and General Relativity (*Springer-Verlag, New York*,(1997).

[285] N. K. Glendenning, Astrophys. J. **293**, 470 (1985).

[286] J. Schaffner-Bielich and A. Gal, Phys. Rev. C **62**, 034311 (1999).

[287] I. Bednarek and R. Manka, Int. J. Mod. Phys. D **10**, 607 (2001).

[288] I. Bednarek and R. Manka, Phys. Rev. C **73**, 045804 (2006).

[289] S. Weissenborn, D. Chatterjee, and J. Schaffner-Bielich, Nucl. Phys. A **881**, 62 (2012).

[290] R. J. Furnstahl and B. D. Serot, Nucl. Phys. A **671**, 447 (2000).

[291] B. K. Sharma, P. K. Panda, and S. K. Patra, Phy. Rev. C **75**, 035808 (2007).

[292] J. Boguta and S. Bohrmann, Phys. Lett. B **102**, 93 (1981).

[293] J. Ellis, J. I. Kaput, and K. A. Olive, Nucl. Phys. B **348**, 345 (1991).

[294] J. Schaffner, C. B. Dover, A. Gal, D. J. Milliner, C. Greiner, and H. stöcker, Ann. Phys. (N.Y.) **235**, 35 (1994).

[295] M. Chiapparini, M. E. Bracco, A. Delfino, M. Malheiro, D. P. Menezes, C. Providência, Nucl. Phys. A **826**, 178 (2009).

[296] A. W. Steiner, S. Reddy, and M. Prakash, Phys. Rev. D **66**, 094007 (2002).

[297] A. W. Steiner, J. M. Lattimer, and E. F. Brown, Astrophys. J. **722**, 33 (2010).

[298] F. Özel, Nature **441**, 1115 (2006).

[299] Isaac Vidaña, Nucl. Phys. A (2013), http://dx.doi.org/10.1016/j.nuclphysa.2013.01.015

[300] F. Sammarruca, Phys. Rev. C **79**, 034301 (2009).

[301] P. M. M. Maessen, T. A. Rijken, J. J. de Swart, Phys. Rev. C **40**, 2226 (1989).

[302] Th. A. Rijken, Y. Yamamoto, Phys. Rev. C **73**, 044008 (2006).

[303] J. K. Bunta and S. Gmuca, Phys. Rev. C **68**, 054318 (2003).

[304] S. Abrahamyan et al. *arXiv.1201.2568v2* (2012).

[305] S. K. Singh, S. K. Biswal, M. Bhuyan, and S. K. Patra, J. Phys. G: Nucl. Part. Phys. **41**, 055201 (2014).

[306] S. K. Singh, S. K. Biswal, M. Bhuyan, and S. K. Patra, Phys. Rev. C **89**, 044001 (2014).

[307] M. Centelles, S. K. Patra, X. Roca-Maza, B. K. Sharma, P. D. Stevenson, and X. Viñas, J. Phys. G **37**, 075107 (2010).

[308] M. Baldo and C. Maieron, Phys. Rev. C **77**, 015801 (2008).

[309] J. Margueron, H. Sagawa, and K. Hagino, Phys. Rev. C **77**, 054309 (2008).

[310] B. Friedman and V. R. Pandharipande, Nucl. Phys. A **361**, 502 (1981).

[311] S. Gandol, A. Yu. Illarionov, S. Fantoni, F. Pederiva, and K. E. Schmidt, Phys. Rev. Lett. **101**, 132501 (2008).

[312] P. Danielewicz, R. Lacey, and W. G. Lynch, Science **298**, 1592 (2002).

[313] F. Hofmann, C. M. Keil, and H. Lenske, Phys. Rev. C **64**, 034314 (2001).

[314] B. S. Sathyaprakash and B. F. Schutz, Living Rev. Relativity **12**, 2 (2009).

[315] J. Aasi et al., arXiv:1309.4027v2.

[316] J. H. Taylor and J. M. Wesselberg, Astrophys. J. **345**, 434 (1989).

[317] C. Sturm et al., Phys. Rev. Lett. **86**, 39 (2001).

[318] C. Fuchs, A. Faessler, E. Zabrodin, and Y.-M. Zheng, Phys. Rev. Lett. **86**, 1974 (2001).

[319] M. Dutra, O. Lourenco, A. Delfino, J. S. Sã Martins, C. Providẽncia, S. S. Avancini, and D. P. Menezes, Phys. Rev. C **77**, 035201 (2008).

[320] H. Komatsu, Y. Eriguchi, and I. Hachisu, Mon. Not. R. Astron. Soc. **237**, 355 (1989).

[321] N. K. Glendenning and F. Weber, Phys. Rev. D **50**, 3836 (1994).

[322] N. Stergioulas and J. L. Friedman, Astrophys. J. **444**, 306 (1995).

[323] B. J. Owen, Phys. Rev. Lett. **95**, 211101 (2005).

[324] M. Bejger and P. Haensel, Astron. Astrophys **396**, 917 (2002).

[325] B. Abbott et al., Phys. Rev. D **76**, 042001 (2007), J. Abadie et al., Phys. Rev. D **85**, 082002 (2012).

[326] P. Jaranowski, A. Krolak, and B. F. Schutz, Phys. Rev. D **58**, 063001 (1998).

[327] http://lisa.nasa.gov/

[328] B. Haskell, N. Andersson, D. I. Jones, and L. Samuelsson, Phys. Rev. Lett. **99**, 231101 (2007).

[329] P. G. Krastev, B. A. Li, and A. Worley, Phys. lett. B **668**, 1 (2008).